A single-cell transcriptomic and anatomic atlas of mouse dorsal raphe *Pet1* neurons

Authors: Benjamin W. Okaty*#, Nikita Sturrock*, Yasmin Escobedo Lozoya, YoonJeung Chang, Krissy A. Lyon, Olga V. Alekseyenko, Susan M. Dymecki#

Department of Genetics, Harvard Medical School, Boston, MA, USA.

* These authors contributed equally

Corresponding Authors

Abstract

The dorsal raphe nucleus (DR) contains the largest brain population of *Pet1*-lineage neurons, a predominantly serotonergic group distributed throughout multiple DR subdomains. These neurons collectively regulate diverse physiology and behavior and are often therapeutically targeted to treat affective disorders. Characterizing *Pet1* neuron molecular heterogeneity and relating it to anatomy is vital for understanding DR functional organization, with potential to inform therapeutic separability. Here we use high-throughput and DR subdomain-targeted single-cell transcriptomics and intersectional genetic tools to map molecular and anatomical diversity of DR-*Pet1* neurons. We describe up to fourteen neuron subtypes, many showing biased cell body distributions across the DR. We further show that *P2ry1-Pet1* DR neurons – the most molecularly distinct of the subtypes – possess unique efferent projections and electrophysiological properties. The present data complement and extend previous DR characterizations, combining intersectional genetics with multiple transcriptomic modalities to achieve fine-scale molecular and anatomic identification of *Pet1* neuron subtypes.

Introduction

Brainstem neurons that synthesize the monoamine neurotransmitter serotonin (5-hydroxytryptamine, 5-HT) (Baker et al., 1991a; Baker et al., 1991b; Baker et al., 1990; Dahlstroem and Fuxe, 1964; Ishimura et al., 1988; Steinbusch, 1981; Steinbusch et al., 1978) derive from embryonic precursors that express the transcription factor PET1 (alias FEV) upon terminal cell division (Hendricks et al., 1999). PET1 shapes the serotonergic identity of neurons by regulating expression of genes required for 5-HT biosynthesis, packaging in synaptic vesicles, reuptake, and metabolism (Hendricks et al., 2003; Krueger and Deneris, 2008; Liu et al., 2010; Wyler et al., 2015; Wyler et al., 2016), though some *Pet1*-lineage cells in the brain have ambiguous phenotypes with respect to their ability to synthesize and release 5-HT (Alonso et al., 2013; Barrett et al., 2016; Okaty et al., 2015; Pelosi et al., 2014; Sos et al., 2017). Aside from shared expression of 5-HT marker genes (to varying degrees), *Pet1*-lineage neurons display wide-ranging phenotypic heterogeneity, including diverse brainstem anatomy, hodology, and expression of neurotransmitters in addition to or other than 5-HT, suggestive of distinct *Pet1* neuron subtypes with divergent neural circuit functions (recently reviewed in (Okaty et al., 2019)). We have previously shown that the mature molecular identities of *Pet1*-lineage neurons strongly correlate with both the embryonic progenitor domain (rhombomeric domain) from which they derive and with their mature anatomy (Jensen et al., 2008; Okaty et al., 2015), largely consistent with (Alonso et al., 2013). However, even within a given *Pet1* rhombomeric sublineage and anatomical subdomain, *Pet1* neurons may display different molecular and cellular phenotypes (Niederkofler et al., 2016; Okaty et al., 2015). *Pet1* neurons project widely throughout the brain and are functionally implicated in numerous life-sustaining biological processes and human pathologies. Thus, assembling a taxonomy of *Pet1* neuron subtypes based on molecular and cellular properties and linking identified *Pet1* neuron subtypes to specific biological functions is important for basic neuroscience and human health, including the development of targeted therapeutics. Here we provide a high-resolution, single-cell transcriptomic atlas of dorsal raphe *Pet1*-lineage neurons revealing hierarchically and spatially organized molecular subtypes, each expressing unique repertoires of neurotransmitters, plasma membrane receptors, ion channels, cell adhesion molecules, and other gene categories important for specifying neuronal functions.

61 The dorsal raphe (DR) nucleus comprises the largest anatomically defined subgroup of
62 *Pet1* expressing cells in the brain, and these cells are derived from embryonic
63 progenitors in the isthmus and rhombomere 1 (Alonso et al., 2013; Jensen et al., 2008).
64 Multiple studies have demonstrated neuronal diversity within the DR, in *Pet1*-expressing
65 5-HT neurons as well as other resident cell populations (Calizo et al., 2011; Challis et al.,
66 2013; Crawford et al., 2010; Fernandez et al., 2016; Huang et al., 2019; Kirby et al.,
67 2003; Niederkofler et al., 2016; Prouty et al., 2017; Ren et al., 2018; Ren et al., 2019;
68 Spaethling et al., 2014; Vasudeva and Waterhouse, 2014; Zeisel et al., 2018). In the
69 present study, we extend these findings by transcriptionally profiling *Pet1*-lineage
70 marked DR neurons using microfluidic cell sorting and droplet-based single-cell RNA
71 sequencing (scRNA-seq). Our particular experimental approach combining intersectional
72 mouse genetics, high-throughput cell-type-specific purification (using the On-chip Sort),
73 and newly improved scRNA-seq library construction chemistry (using the 10X Genomics
74 Chromium Single Cell 3' v3 kit) allowed us to surpass prior resolution of DR *Pet1* neuron
75 molecular diversity, both in terms of the number of DR *Pet1* cells profiled and the
76 number of transcriptomically distinct *Pet1* neuron subtypes identified. To further
77 characterize the anatomical organization of these molecularly defined *Pet1* neuron
78 subtypes, we used intersectional mouse transgenic tools, crossing *Pet1::Flpe* mice with
79 various subtype-relevant Cre-driver mice and dual Flpe- and Cre-responsive fluorescent
80 reporter lines. In addition to performing histological analyses of these intersectionally
81 defined *Pet1*-lineage neuron subpopulations, we further characterized them using
82 manual cell-sorting from microdissected sub-domains of the DR followed by scRNA-seq.
83 Comparing this data with our high-throughput droplet-based scRNA-seq approach
84 allowed us to map *Pet1* neuron molecular diversity onto DR anatomy. We found that DR
85 *Pet1*-lineage neurons comprise as many as fourteen distinct molecularly defined
86 subtypes, several of which we show are anatomically biased within rostral-caudal,
87 dorsal-ventral, and medial-lateral axes. Additionally, by combining intersectional genetics
88 with projection mapping and *ex vivo* slice electrophysiology we show examples of
89 distinct *Pet1* neuron molecular subtypes that also differ in other cellular phenotypes
90 important for function, such as hodology and electrophysiology.

91 **Results**

92 **Droplet-based scRNA-seq of *Pet1* fate-mapped DR neurons reveals new**
93 **molecularly defined neuron subtypes**

94 To characterize the molecular diversity of *Pet1*-lineage DR neurons in a targeted, high-
95 throughput, high-resolution manner we partnered recombinase-based genetic fate
96 mapping, microfluidic fluorescence-based cell sorting, and droplet-based single-cell
97 barcoding followed by RNA-seq library preparation and next-generation sequencing
98 using the 10X Genomics Chromium Single Cell 3' v3 kit (**Figure 1A; Methods**).
99 Fluorescent labeling of *Pet1*-lineage DR neurons was achieved in mice of the following
100 genotypes: (1) *Pet1::Flpe* (Jensen et al., 2008); *En1::cre* (Kimmel et al., 2000);
101 *RC::FrePe* (the latter transgene a dual Flpe- and Cre-dependent fluorescent reporter
102 inserted into the *ROSA26* (*R26*) locus (Brust et al., 2014; Dymecki et al., 2010; Okaty et
103 al., 2015)), in which *Pet1*-lineage neurons derived from the *En1*$^+$ isthmus and
104 rhombomere 1 (r1) embryonic progenitor domains, are marked by eGFP expression or
105 (2) *Pet1::Flpe; RC*::*FL-hM3Dq* (Sciolino et al., 2016), in which all *Pet1* neurons are
106 eGFP-labeled (Cre was not utilized in these experiments, thus only eGFP, not hM3Dq,
107 was expressed).

108 Brains were acutely dissected from 6-10 week old mice of both genotypes (4 males and
109 6 females), and DR cells were dissociated as previously described (Okaty et al., 2015)
110 (also see **Methods**). eGFP-expressing neurons were selectively purified using the On-
111 chip Sort (On-chip Biotechnologies Co., Ltd.), a recently developed technology that
112 greatly reduces the pressure forces typically exerted on cells in conventional flow
113 sorters, thereby achieving higher levels of cell viability (Watanabe et al., 2014). Indeed,
114 examination of sorted neurons revealed that many still had intact processes emanating
115 from their somas. Cells were then run through the 10X Genomics Chromium Single Cell
116 3' v3 protocol, followed by Illumina NextSeq 500 sequencing. The Cell Ranger pipeline
117 was used for transcript mapping and single-cell de-multiplexing, and all analyses of
118 transcript counts were performed using the R package Seurat (Butler et al., 2018; Stuart
119 et al., 2019) (also see **Methods**). After stringently filtering out "suspect" single-cell
120 libraries (e.g. libraries with high levels of non-neuronal or mitochondrial genes, outlier
121 library complexity, or absence/low levels of *Pet1* transcripts), we obtained 2,350 single
122 cells for further analysis, with a mean of 7,521 genes detected per single cell library
123 (mean of 57,678 UMIs per cell), and a total of 17,231 genes detected in aggregate (after
124 filtering out genes that were expressed in fewer than ten cells).

125 As the principal goal of our scRNA-seq experiments was to characterize molecular
126 diversity of *Pet1*-lineage neurons, our analyses were aimed at identifying genes with

127 significantly variable transcript expression across single neurons, and using these gene
128 expression differences to classify *Pet1*-lineage neuron subtypes. Typical clustering
129 approaches used to classify cell types (or cell states) based on scRNA-seq data are
130 largely unsupervised, but do require supervised input regarding a number of parameters
131 that have the potential to significantly alter the resulting cluster assignments. These
132 parameters include the data reduction used prior to clustering (such as principal
133 components analysis), the number of components included in the reduction, and a
134 resolution or granularity parameter that determines the "community" size of clusters (i.e.
135 whether cluster boundaries are more or less inclusive; coarse-grained or fine-grained).
136 Rather than arbitrarily choosing a set of parameters for our *Pet1*-lineage neuron subtype
137 classification, we chose a more exploratory approach by systematically varying key
138 parameters and examining how sensitive the resulting clusters were to these
139 combinations of parameters.

140 First, single-cell transcript counts were log-normalized, and we carried out principal
141 components analysis (PCA) on the scaled and centered expression values of the top two
142 thousand genes with the highest variance (after applying a variance-stabilizing
143 transform, see **Methods**) in order to reduce the dimensionality of the data onto a smaller
144 set of composite variables that represent the most salient gene expression differences.
145 Plotting the variance explained by each principal component we observed an inflection
146 point, or "elbow", around the fiftieth component suggesting a drop-off in the information
147 content of subsequent components (**Figure 1–figure supplement 1A**), and found that
148 roughly forty percent of the total variance was explained by these first fifty components.
149 Further examination of the gene loadings of each component revealed that components
150 six and seven were heavily weighted towards sex-specific transcripts and transcripts that
151 largely correlated with batch. As our experiments were not designed to explicitly
152 compare sex as a variable, and given the difficulties of interpreting batch-correlated
153 gene expression differences (e.g. these could stem from population sampling biases of
154 the different cell sorts, different genotypes used, different balance of sexes, or any
155 number of idiosyncratic biological and technical differences) we ultimately chose to
156 remove components six and seven from downstream analyses (though we found that
157 their inclusion had only modest effects on data clustering).

158 Next, we varied: (1) the number of PCs included in the data reduction (from one to fifty,
159 excluding PCs six and seven) used as input to the Seurat FindNeighbors function, and

160 (2) the resolution parameter in the Seurat FindClusters function (from 0.1 to 2.0, in
161 intervals of 0.1, using the Louvain algorithm). The results of this analysis are
162 summarized in the heatmap in **Figure 1–figure supplement 1B**. Including only the first
163 few principal components led to highly variable numbers of clusters depending on the
164 resolution parameter (resulting in as many as 40 clusters at the highest resolution).
165 However, for all resolutions the number of clusters mostly stabilized after including the
166 first thirty PCs. In this regime of parameter space the number of clusters was, for the
167 most part, bounded between five and twenty depending on the resolution. As a first pass
168 at homing in on the "optimum" number of clusters (strictly in a heuristic sense), we
169 calculated the frequency of obtaining a given number of clusters over all combinations of
170 parameters, reasoning that cluster numbers that are less sensitive to precise tuning of
171 parameters would appear more frequently, and the "robustness" of these cluster
172 numbers might more faithfully reflect biologically meaningful subgroup structure in the
173 data. The cluster number frequency plot in **Figure 1–figure supplement 1C** shows that
174 there are four local maxima and one global maximum corresponding to five, eight,
175 eleven, fourteen, and seventeen clusters respectively. Given the high frequency of these
176 cluster numbers, we chose to examine their composition more carefully. As multiple
177 combinations of parameters lead to the same number of clusters (**Figure 1–figure**
178 **supplement 1D**), in some cases leading to differences in cluster composition (generally
179 subtle), we decided to err on the side of including more data and thus fixed the number
180 of PCs at one to fifty, excluding PCs six and seven, and varied the resolution to obtain
181 five, eight, eleven, fourteen, and seventeen clusters.

182 We characterized cluster structure through hierarchical dendrograms, uniform manifold
183 approximation and projection for dimension reduction (UMAP) (a technique recently
184 developed by McInness, Healy, and Melville as described in a manuscript available at
185 arXiv.org, and implemented in Seurat), and differential expression analysis using
186 Wilcoxon rank-sum tests to identify transcripts that are significantly enriched or depleted
187 among clusters (**Figure 1–figure supplement 2A-I**, **Figure 1 B-D**). We ultimately
188 judged seventeen clusters (resolution = 1.5) to be excessive, due to the inclusion of
189 clusters with very few enriched genes as well as clusters that appeared somewhat
190 intermixed in UMAP space (analysis not shown). We thus focused our analyses on lower
191 resolution clusters. Across all resolutions analyzed (0.1, 0.3, 0.7, and 0.9), we found a
192 common set of genes that was useful in characterizing cluster structure, namely *Tph2,*

193 *Gad2, Gad1, Slc17a8 (*alias *Vglut3*)*,* and *Met*. The *Tph2* gene encodes for tryptophan
194 hydroxylase 2, the rate-limiting enzyme involved in 5-HT biosynthesis in the central
195 nervous system (Walther and Bader, 2003; Walther et al., 2003), and all but one cluster
196 showed consistently high *Tph2* transcript expression. In the five- and eight-cluster-
197 number analyses (resolution = 0.1 and 0.3, respectively), one cluster displayed a
198 strikingly bi-modal distribution of *Tph2* transcript expression (**Figure 1–figure**
199 **supplement 2A,D**, clusters four and six, respectively), however increasing the resolution
200 further divided this group into a *Tph2*-low and a *Tph2*- "variable" group, displaying a
201 broader distribution of single-cell expression than other clusters (**Figure 1–figure**
202 **supplement 2G** and **Figure 1B**, clusters ten and fourteen, respectively, corresponding
203 to resolutions of 0.7 and 0.9). Beyond *Tph2* expression, these two subgroups displayed
204 similarly shaped distributions (lower mean expression and higher variability) for several
205 5-HT neuron marker genes (**Figure 1–figure supplement 3**). *Gad1* and *Gad2* are
206 paralogous genes that encode two distinct forms of the gamma-aminobutyric acid
207 (GABA) synthetic enzyme glutamate decarboxylase (Erlander et al., 1991), and we
208 found a sizable cluster of *Pet1* neurons (~50%) that express high levels of *Tph2* and
209 *Gad2*, and to a lesser extent *Gad1* (generally detected in fewer cells than *Gad2*), which
210 could be further subdivided into five sub-clusters at finer resolution (**Figure 1B, C,**
211 clusters two-six**)**. One of these clusters, cluster six (**Figure 1B,C**), contained *Pet1*
212 neurons additionally expressing intermediate levels of transcripts for *Vglut3,* encoding
213 the vesicular glutamate transporter 3 (Fremeau et al., 2002; Gras et al., 2002). Notably,
214 this group of neurons also had the highest expression of *Gad1* relative to other groups.
215 High expression levels of *Vglut3* transcripts were detected in eight clusters (**Figure 1B,**
216 **C,** clusters seven to fourteen), comprising ~46% of profiled *Pet1* neurons, including the
217 *Tph2*-low and *Tph2*-variable clusters (**Figure 1B, C,** clusters 13 and 14). Cluster twelve,
218 the most striking outlier group of *Pet1* neurons, is characterized by high transcript
219 expression of *Tph2*, *Vglut3,* and *Met,* the latter encoding the MET proto-oncogene (also
220 known as hepatocyte growth factor receptor) (Iyer et al., 1990). The remaining 4% of
221 *Pet1* neurons, comprising cluster one, expressed high levels of *Tph2* transcripts but only
222 sporadically expressed transcripts for *Gad2*, *Gad1*, or *Vglut3* (**Figure 1B,C**).

223 Examination of the dendrogram in **Figure 1B** and the UMAP plot in **Figure 1C** (as well
224 as examining the successively parcelled UMAP clusters in **Figure 1–figure supplement**
225 **2B, E, and H** with increasing resolution) gives a sense of "relatedness" among clusters.

226 For example, *Gad1/2-Tph2* clusters two to four are more similar to each other than to
227 *Vglut3-Tph2* clusters, while cluster six, the *Gad1/2-Vglut3-Tph2* cluster, and cluster five
228 are situated between the other *Gad1/2-Tph2* and *Vglut3-Tph2* groups. Like cluster
229 twelve, clusters thirteen and fourteen appear as outliers from the other clusters in the
230 dendrogram (**Figure 1B)**, but despite showing low and variable expression of the 5-HT
231 neuron marker gene *Tph2*, respectively, they nonetheless cluster more closely to other
232 *Pet1* neurons than do *Met-Vglut3-Tph2-Pet1* neurons (cluster twelve) in the UMAP plot
233 (**Figure 1C)**.

234 *Met*-expressing *Pet1* neurons have been previously reported in mice, both at the
235 transcript and protein levels, specifically in the caudal DR and the median raphe (MR)
236 (Kast et al., 2017; Okaty et al., 2015; Wu and Levitt, 2013) and more recently (Huang et
237 al., 2019; Ren et al., 2019). Likewise, *Vglut3-* and *Gad1/2*-expressing DR *Pet1* neurons
238 have been previously reported in mice and rats, as demonstrated by mRNA *in situ*,
239 immunocytochemistry, and RNA-seq (Amilhon et al., 2010; Commons, 2009; Fu et al.,
240 2010; Gagnon and Parent, 2014; Gras et al., 2002; Herzog et al., 2004; Hioki et al.,
241 2004; Hioki et al., 2010; Huang et al., 2019; Okaty et al., 2015; Ren et al., 2018; Ren et
242 al., 2019; Rood et al., 2014; Shikanai et al., 2012; Spaethling et al., 2014; Voisin et al.,
243 2016). Consistent with functional expression of VGLUT3, which allows for filling of
244 synaptic vesicles with the excitatory neurotransmitter glutamate, depolarization-induced
245 glutamate release by DR *Pet1*/5-HT neurons has been demonstrated by a number of
246 groups (Johnson, 1994; Kapoor et al., 2016; Liu et al., 2014; Sengupta et al., 2017;
247 Wang et al., 2019). Additionally, VGLUT3 is thought to interact with vesicular
248 monoamine transporter two (encoded by *Slc18a2,* alias *Vmat2* (Erickson et al., 1992)) to
249 enhance the loading of 5-HT into synaptic vesicles by increasing the pH gradient across
250 vesicular membranes, a process referred to as “vesicle-filling synergy” (Amilhon et al.,
251 2010; El Mestikawy et al., 2011; Munster-Wandowski et al., 2016). GABA-release by
252 *Pet1* DR neurons, on the other hand, has not been reported, thus the functional
253 consequences of *Gad1* and *Gad2* transcript expression are presently unknown.

254 **Differentially expressed genes span functional categories relevant to neuronal**
255 **identity**

256 Scaled expression of the top five marker genes for each cluster (ranked by Bonferroni
257 corrected p-value or in some cases fold enrichment) are represented in the heatmaps in

258 **Figure 1–figure supplement 2C, F, I**, and **Figure 1D,** depending on the cluster
259 resolution. To aid interpretation of the functional significance of differentially expressed
260 genes, expression patterns of a subset of significantly variable genes and cluster
261 markers (for the fourteen clusters resulting from a cluster resolution of 0.9) are
262 represented in the dot plots in **Figure 2**, organized by categories of biological function
263 (identified by Gene Ontology annotations and literature searches). These gene
264 categories were selected based on general importance for shaping neuronal functional
265 identity – e.g. genes that encode transcription factors which broadly regulate molecular
266 phenotypes, as well as genes that encode ion channels, plasma membrane receptors,
267 calcium-binding proteins, kinases, and cell adhesion and axon guidance molecules,
268 which collectively govern neuronal electrophysiology, signal transduction, and synaptic
269 connectivity.

270 *Transcription Factors*

271 History of expression of *Pet1/Fev,* encoding the FEV transcription factor, ETS family
272 member (Fyodorov et al., 1998; Hendricks et al., 1999) defines the *Pet1* neuronal
273 lineage. As can be observed from the transcription factor dot plot in **Figure 2** (as well as
274 the violin plot in **Figure 1–figure supplement 3**), *Pet1/Fev* displays broad expression
275 across clusters but is expressed at significantly lower levels in cluster thirteen *Pet1*
276 neurons. Several genes known to be directly regulated by *Pet1* (Hendricks et al., 2003;
277 Liu et al., 2010; Wyler et al., 2015; Wyler et al., 2016), such as *Tph2*, *Slc6a4* (*Sert*)
278 (encoding the serotonin transporter (Hoffman et al., 1991; Lesch et al., 1993)), and
279 *Slc18a2* (*Slc18a2*) likewise show reduced expression in cluster thirteen. The
280 transcription factor engrailed 1 (*En1*) (Joyner et al., 1985), in its expression overlap with
281 *Pet1,* is a marker of having derived from progenitors in the isthmus and r1 (Alonso et al.,
282 2013; Jensen et al., 2008; Okaty et al., 2015), and, as expected, *En1* transcripts are
283 detected broadly across all DR clusters. The paralogous gene engrailed 2 (*En2*) (Joyner
284 and Martin, 1987), shows a more variable expression profile across *Pet1* DR neurons,
285 being largely absent in cluster eight and twelve, and significantly lower in cluster seven.
286 *En1* and *En2* are required for normal development of DR *Pet1* neuron cytoarchitecture
287 and for perinatal maintenance of serotonergic identity (Fox and Deneris, 2012). *Nr3c1*,
288 encoding the nuclear receptor subfamily 3, group C, member 1, aka the glucocorticoid
289 receptor, which binds the stress hormone corticosterone (cortisol in humans), is
290 expressed broadly across clusters one through eleven, but is de-enriched in cluster

291 twelve, and to a lesser extent clusters thirteen and fourteen, suggesting differential
292 sensitivity to corticosterone across different *Pet1* neuron molecular subtypes. Numerous
293 studies have highlighted the functional importance of DR glucocorticoid signaling for 5-
294 HT neuron activity and behavioral modulation (Bellido et al., 2004; Evrard et al., 2006;
295 Judge et al., 2004; Laaris et al., 1995; Vincent et al., 2018; Vincent and Jacobson,
296 2014).

297 Other transcription factor encoding genes show more striking expression specificity.
298 Transcripts for neuronal pas domain 1 and 3 (encoded by *Npas1* and *Npas3*) and POU
299 class 3 homeobox 1 (*Pou3f1*) are significantly enriched in cluster one *Pet1* neurons.
300 From mouse genetic studies, both NPAS1 and NPAS3 are associated with regulation of
301 genes and behavioral endophenotypes implicated in psychiatric disorders, such as
302 schizophrenia, though NPAS1/3 are also expressed by other cell types in the brain, such
303 as cortical interneurons, which may contribute to observed behavioral effects of *Npas1/3*
304 loss of function (Erbel-Sieler et al., 2004; Michaelson et al., 2017; Stanco et al., 2014).

305 *Pax5*, encoding paired box 5 (Asano and Gruss, 1992), a transcription factor involved in
306 the regulation of isthmic organizer activity during development (Funahashi et al., 1999;
307 Ye et al., 2001) is significantly enriched in clusters two, four, and five, and highly
308 expressed in clusters three and six as well. *Pou6f2* (POU class 6 homeobox 2) and *Klf5*
309 (Kruppel like factor 5) show a similar pattern of expression. *Sox14* (SRY-box
310 transcription factor 14) and *Satb2* (SATB homeobox 2) show an even more restricted
311 expression profile, limited to clusters two through four. Notably, clusters two through six
312 are also enriched for expression of *Gad2*, which, like *Sox14*, is most highly expressed in
313 cluster four. *Sox14* expression has been shown to regulate GABAergic cell identity in the
314 dorsal midbrain (Makrides et al., 2018), and *Pax5* expression has been implicated in
315 GABAergic neurotransmitter specification in the dorsal horn of the spinal cord (Pillai et
316 al., 2007), suggesting that these genes may play similar roles in DR *Pet1* neurons.
317 Interestingly, *Nr2f2* (encoding nuclear receptor subfamily 2, group F, member 2, alias
318 COUP-TFII) shows an expression profile that is complementary to *En2* and *Pax5,*
319 enriched in cluster eight, nine, and twelve, all of which are enriched for *Vglut3*
320 transcripts, and are largely devoid of *Gad1/2* expression.

321 Overall, each of the fourteen transcriptome-defined clusters of DR *Pet1* neurons can
322 largely be classified by the combinatorial expression of two to three transcription factors.

323 For example, *Pou3f2* (POU class three homeobox 2), *Bcl11a* (B cell CLL/lymphoma 11A
324 zinc finger protein), and *Id2* (inhibitor of DNA binding 2) show enriched expression in
325 cluster six, and to a lesser extent cluster thirteen. Other notable transcription factor
326 markers of *Pet1* neuron subgroups include *Foxp1* (forkhead box P1), enriched in
327 clusters seven and fourteen, *Rorb* (RAR-related orphan receptor beta), enriched in
328 cluster eight, *Maf* (avian musculoaponeurotic fibrosarcoma oncogene homolog),
329 enriched in cluster nine, *Foxa1* (forkhead box A1), enriched in cluster eleven, *Zeb2* (zinc
330 finger E-box binding homeobox 2) enriched in cluster twelve, *Zfp536* (zinc finger protein
331 536), *Nfix* (nuclear factor I/X), and *Nfib* (nuclear factor I/B), enriched in cluster thirteen
332 (detected in cluster six as well), and *Ldb2* (LIM domain binding 2), enriched in clusters
333 thirteen and fourteen.

334 *Neurotransmitters and Neuropeptides*

335 *Pet1* neuron subtypes defined by transcriptomic clustering also show differential
336 expression of a number of neurotransmitter-related and neuropeptide-encoding genes
337 (**Figure 2** Neurotransmitters and Neuropeptides dot plot). Transcript profiles related to
338 classic neurotransmitter production, including *Tph2, Gad2, Gad1,* and *Slc17a8,* have
339 already been described above (see also **Figure 1B**). Transcript expression of *Trh*,
340 encoding thyrotropin-releasing hormone, is significantly enriched in cluster two *Pet1*
341 neurons and detected in clusters four and six (**Figure 1D** and **Figure2**). Another gene
342 involved in thyroid hormone signaling, *Crym*, encoding crystalline mu, also known as
343 NADP-regulated thyroid-hormone-binding protein shows a similar expression profile
344 (**Figure 1D**). *Pdyn*, encoding the preprohormone prodynorphin is enriched in clusters
345 five, six, and fourteen. Prodynorphin is the precursor protein to the opioid polypeptide
346 dynorphin, which predominately binds the kappa-opioid receptor to produce a variety of
347 effects, such as analgesia and dysphoria (Bruchas et al., 2010; Chavkin et al., 1982;
348 Land et al., 2008; Land et al., 2009). Expression of *Nos1*, encoding nitric oxide synthase
349 1, is significantly enriched in cluster five, nine, and eleven. The anatomical distribution of
350 nitric oxide expressing DR 5-HT neurons in rodents has been characterized previously
351 as being predominately midline in the DR (Fu et al., 2010; Prouty et al., 2017; Vasudeva
352 et al., 2011; Vasudeva and Waterhouse, 2014). Cluster nine also shows enriched
353 expression of *Crh*, encoding corticotropin-releasing hormone. Several other
354 neuropeptide encoding genes show sporadic, significantly variable expression among

355 different clusters, including growth hormone-releasing hormone (*Ghrh),* neuromedin B
356 (*Nmb),* neuropeptide B (*Npb),* proenkephalin (*Penk),* and somatostatin (*Sst).*

357 *Ionotropic and G-Protein Coupled Receptors*

358 Cluster one and cluster thirteen *Pet1* neurons show the most prominent specificity with
359 respect to ionotropic receptor markers (**Figure 2 Ionotropic Receptors**), though in
360 general we found relatively few *Pet1* neuron subtype-specific ionotropic gene markers
361 relative to other categories of gene function. *Gabrq* and *Gabre*, encoding GABA type A
362 receptor subunits theta and epsilon, respectively, are significantly enriched in cluster
363 one, as well as *Gria1,* encoding glutamate ionotropic receptor AMPA type subunit 1.
364 GABA type A receptor subunit gamma3 (*Gabrg3*) and glutamate ionotropic receptor
365 NMDA type subunit 2A (*Grin2a*) transcripts are largely de-enriched in clusters two
366 through four and twelve, are significantly enriched in cluster nine, and variably
367 expressed in other clusters. GABA A receptor subunit alpha 2 (*Gabra2*) is expressed in
368 all clusters but is significantly enriched in cluster twelve, and GABA A receptor subunit
369 alpha 1 (*Gabra1*) and glutamate ionotropic receptor AMPA type subunit 3 (*Gria3*)
370 transcripts both show significant enrichment in cluster thirteen.

371 Transcripts encoding G protein-coupled receptors (GPCRs) show patterns of enrichment
372 largely across blocks of clusters (e.g. *Vglut3*-expressing versus non-*Vglut3*-expressing
373 *Tph2-Pet1* neurons), or highly specific enrichment in either cluster twelve or clusters
374 thirteen and fourteen (**Figure 2 G Protein-coupled Receptors**). For example, cluster
375 twelve neurons show strong enrichment for opioid receptor mu (*Oprm1*), purine receptor
376 y1 (*P2ry1)*, relaxin receptor (*Rxfp1)*, sphingosine-1-phosphate receptor *3* (*S1pr3*), and
377 tachykinin receptor 3 (*Tacr3)* transcripts. Moreover, they lack expression of transcripts
378 for many GPCRs expressed by the majority of other *Pet1* neurons, such as presynaptic
379 5-HT autoreceptors, encoded by *Htr1b* and *Htr1d*, as well as orexin and histamine
380 receptors (e.g. *Hcrtr1*, *Hcrtr2*, *Hrh1*, *Hrh3*), whose protein products are involved in the
381 regulation of arousal. We found that histamine receptor 1 (*Hrh1*) and hypocretin (alias
382 orexin) receptor 1 (*Hcrtr1*) transcripts were the most abundant in clusters one through
383 four, and histamine receptor 3 (*Hrh3*) transcripts were the most abundant in clusters two
384 through six. Hypocretin receptor 2 (*Hcrtr2*) transcripts showed a somewhat
385 complementary expression pattern, with the highest levels in clusters seven through
386 eleven, as well as cluster three. Other GPCR transcripts with notable expression

387 patterns are neuropeptide Y receptor Y2 (*Npy2r*), enriched in clusters seven and ten,
388 cannabinoid receptor 1 (*Cnr1*) and 5-HT receptor 2C (*Htr2c*), enriched in clusters
389 thirteen and fourteen, and *Gpr101*, an "orphan" GPCR thought to play a role in the
390 growth hormone releasing-growth hormone signaling axis (GHRH-GH axis) (Trivellin et
391 al., 2016; Trivellin et al., 2018), enriched in cluster fourteen.

392 *Regulators of Neuron Projections, Synaptic Connectivity, and Heparan Sulfate*
393 *Proteoglycans*

394 Similar to transcription factor expression patterns, most DR *Pet1* neuron subgroups can
395 be classified by combinatorial enrichment of transcripts for genes encoding regulators of
396 neuron projections and synaptic connectivity (**Figure 2 Regulators of Neuron**
397 **Projections and Synaptic Connectivity**). Differential expression of these genes likely
398 contributes to differential innervation patterns of distinct DR *Pet1* neuron subgroups,
399 such as reported by various studies (Fernandez et al., 2016; Huang et al., 2019; Kast et
400 al., 2017; Muzerelle et al., 2016; Niederkofler et al., 2016; Ren et al., 2018; Ren et al.,
401 2019; Teng et al., 2017), and yet to be uncovered. Genes encoding regulators of
402 heparan sulfate proteoglycans may also play a role in projection specificity and synaptic
403 organization (Condomitti and de Wit, 2018; Di Donato et al., 2018; Lazaro-Pena et al.,
404 2018; Minge et al., 2017; Zhang et al., 2018), and likewise show patterns of enrichment
405 across different *Pet1* neuron clusters (**Figure 2 Regulators of Heparan Sulfate**
406 **Proteoglycans**). For example, transcript expression of heparan sulfate-glucosamine 3-
407 sulfotransferase 4 (*Hs3st4*) is enriched across clusters one through four, heparan
408 sulfate-glucosamine 3-sulfotransferase 5 (*Hs3st5*) expression is significantly enriched in
409 cluster ten (and expressed at high levels in clusters one, eight, nine, and eleven), and
410 sulfatase 2 (*Sulf2*) and heparan sulfate-glucosamine 3-sulfotransferase 2 (*Hs3st2*)
411 transcripts are enriched in cluster thirteen.

412 **Intersectional genetic labeling of *Pet1* neuron subgroups in combination with**
413 **histology and manual scRNA-seq reveals spatial distributions of DR *Pet1* neuron**
414 **subtypes**

415 Having identified transcriptomically distinct DR *Pet1* neuron subtypes in a largely
416 unsupervised manner, we next sought to determine whether the cell bodies of these
417 molecularly defined *Pet1* neuron subtypes show differential distributions within

418 anatomical subfields of the DR. Using intersectional genetics to fluorescently label *Pet1*
419 neuron subgroups defined by pairwise expression of *Pet1* and one of an assortment of
420 identified subtype marker genes, we iteratively mapped molecular subtypes to anatomy
421 in two ways – (1) using histology and microscopy to directly characterize cell body
422 locations in fixed brain sections (**Figure 3**), and (2) performing manual scRNA-seq on
423 labeled cells dissociated and hand sorted from microdissected anatomical subdomains
424 of the DR, and comparing these expression profiles to our above described high-
425 throughput scRNA-seq data (which we will refer to as our 10X scRNA-seq data) (**Figure**
426 **4**). We iteratively bred triple transgenic mice harboring (1) our *Pet1::Flpe* transgene, (2)
427 one of two dual Flpe- and Cre- responsive reporter constructs (*RC::FrePe* or *RC*::*FL-*
428 *hM3Dq*), and (3) one of five Cre-encoding transgenes (*Sert::cre*, *Vglut3::IRES-cre*,
429 *Npy2r::IRES-cre*, *Crh::cre*, or *P2ry1::IRES-cre*), where *cre* expression is driven by either
430 the endogenous promoter of the marker gene or by a gene-specific bacterial artificial
431 chromosome (BAC). In selecting candidate markers from our list of differentially
432 expressed genes, we sought gene drivers that could potentially divide *Pet1* neurons into
433 subgroups at varying resolutions and were available as *cre* lines. Representative
434 images for each triple transgenic genotype are given in **Figure 3** (organized by marker
435 genes, columns A-E, at different rostrocaudal levels of the DR, rows 1-6). For each
436 genotype, the intersectionally defined subpopulation of neurons is labeled in green (i.e.
437 history of Flpe and Cre expression) whereas the "subtractive" subpopulation is labeled in
438 red (i.e. history of Flpe but not Cre expression).

439 *Histology of Pet1-Intersectionally Defined Neuron Populations*

440 High *Sert* expression, like high *Tph2* expression, defines *Pet1* neuron clusters one
441 through eleven. Cluster twelve shows consistently lower mean expression of *Sert*
442 transcripts (and to a lesser extent *Tph2* transcripts) than clusters one through eleven
443 (**Figure 3A**), cluster fourteen shows a broader distribution of *Sert* transcript levels
444 (**Figure 3A**) and most 5-HT markers (**Figure 1–figure supplement 3**), and cluster
445 thirteen shows very low levels of *Sert* transcripts (**Figure 3A**) and other 5-HT markers
446 (**Figure 1–figure supplement 3**). Consistent with the majority of profiled *Pet1* neurons
447 expressing high levels of *Sert* and *Pet1* transcripts, we detected intersectional
448 *Sert::cre;Pet1::Flpe* fluorescently marked neurons throughout the full rostrocaudal and
449 dorsoventral extent of the DR (**Figure 3A1-A6**), however the subtractive population
450 (presumably cluster thirteen and perhaps some cluster twelve and fourteen *Pet1*

451 neurons) showed a more limited distribution. These subtractive (Flpe+ but Cre-) neurons
452 were most conspicuously concentrated in the rostromedial DR (**Figure 3A2**), where only
453 a few *Sert::cre;Pet1::Flpe* intersectional (Flpe+ and Cre+) neurons were intermingled.
454 More caudally, the Flpe-only, subtractive neurons remained largely midline, but became
455 more intermixed with the double-positive *Sert::cre;Pet1::Flpe* intersectionally marked
456 cells. As another way of anatomically characterizing putative cluster thirteen *Pet1*
457 neurons, we immunostained for TPH2 in *En1::cre;Pet1::Flpe;RC::FrePe* mice (the same
458 genotype as used in some of our 10X scRNA-seq experiments), and found that the
459 distribution of TPH2 immuno-negative *Pet1* neuron cell bodies showed a very similar
460 distribution to the subtractive neurons (Flpe-only) in *Sert::cre;Pet1::Flpe;RC::FrePe*
461 mice. (**Figure 3–figure supplement 1A-B**), further confirming the existence of *Pet1*-
462 expressing neurons that do not express TPH2 protein (Barrett et al., 2016; Pelosi et al.,
463 2014). We consistently observed that these *Pet1::Flpe*-captured, TPH2-immunonegative
464 neurons often have smaller cell soma and bipolar morphology (**Figure 3–figure**
465 **supplement 1B**).

466 *Vglut3-Pet1* expression defines *Pet1* neuron clusters seven through fourteen, and to a
467 lesser extent cluster six (**Figure 3B**). We observed that *Vglut3::cre;Pet1::Flpe*
468 intersectionally marked neurons show a strong ventromedial bias in rostral portions of
469 the DR (**Figure 3B1-B3**), and are the predominant *Pet1* neuron subgroup in the more
470 caudal midline DR (**Figure 3B3-B6**). By contrast, the subtractive *Pet1* neuron subgroup
471 (presumably comprising *Pet1* neurons from clusters one through five and partly six)
472 show a strong dorsal and lateral bias and are largely absent from the most caudal
473 portions of the DR. We further characterized VGLUT3 protein expression in *Pet1*
474 neurons by VGLUT3 immunohistology in *Vglut3::IRES-cre;Pet1::Flpe; RC::FL-hM3Dq*
475 mice. We found consistent overlap between intersectional recombination marked
476 neurons and VGLUT3 protein expression, especially in medial, ventromedial, and caudal
477 portions of the DR (**Figure 3–figure supplement 1C-J**). In the dorsal and lateral
478 portions of the DR, however, where there are far fewer intersectionally labeled neurons,
479 we observed a small number of *Vglut3::cre;Pet1::Flpe* intersectionally marked neurons
480 that were negative for VGLUT3 antibody staining, suggesting transient expression of
481 *Vglut3* (and *Vglut3::IRES-cre)* by these cells at an earlier time in their developmental
482 history (or low *Vglut3* expression sufficient to drive Cre expression, but not VGLUT3
483 immunodetection).

484 Transcripts for *Npy2r*, encoding the neuropeptide Y receptor 2, are strongly enriched in
485 clusters six, seven, and ten, with less consistent expression in clusters eleven, thirteen,
486 and eight, and only sporadic expression elsewhere (**Figure 3C**). In mid-rostral portions
487 of the DR, we found that *Npy2r::cre;Pet1::Flpe* intersectionally marked cell bodies show
488 a largely midline bias, with a greater density of cells ventrally than dorsally, and the
489 occasional labeled cell body appearing more laterally (**Figure 3C2-C3**). In more caudal
490 extents of the DR, *Npy2r::cre;Pet1::Flpe* intersectionally marked cell bodies appear to be
491 concentrated more medially (**Figure 3C4-C6**).

492 Transcripts for *Crh*, encoding corticotropin-releasing hormone, are most highly enriched
493 in neurons comprising cluster nine and to a lesser extent cluster five, with sporadic
494 expression in other clusters (**Figure 3D**). *Crh::cre;Pet1::Flpe* intersectionally labeled
495 neurons do not show an obvious overall anatomical bias, distributing widely throughout
496 the DR (**Figure 3D1-D6**). At the most rostral levels of the DR, they appear to be more
497 consistently medially and ventrally localized (**Figure 3D1-D2**), but additionally appear in
498 the dorsal and lateral DR at mid-rostral levels, and are preferentially localized off the
499 midline more ventrally in these same sections (in regions sometimes referred to as the
500 ventrolateral wings) (**Figure 2D3-D4**). At the most caudal levels they distribute dorsally
501 and ventrally, with an apparent gap between these two domains (**Figure 3D5-D6**).

502 The most molecularly distinct *Pet1* neuron subtype we identified, cluster twelve *Met-*
503 *Vglut3-Tph2-Pet1* neurons, shows highly specific enrichment for a number of transcripts,
504 including *P2ry1*, encoding purinergic receptor P2Y1, which is only sporadically
505 expressed in other clusters (**Figure 3E**). *P2ry1::cre;Pet1::Flpe* intersectionally marked
506 neurons likewise show a strikingly unique anatomical distribution from the other
507 subgroups examined, being largely restricted to the caudal DR where they are densely
508 clustered dorsally, just beneath the aqueduct (**Figure 3E5-E6**). This is consistent with
509 previous characterizations of *Met*-expressing *Pet1/*5-HT neurons (Okaty et al., 2015; Wu
510 and Levitt, 2013), as well as other more recent characterizations (Huang et al., 2019;
511 Kast et al., 2017; Ren et al., 2019). Notably the distribution of *P2ry1::cre;Pet1::Flpe*
512 intersectional neurons within the cDR is distinct from *Npy2r:: cre;Pet1Flpe* intersectional
513 neurons, and only partially overlaps with where *Crh::cre;Pet1::Flpe* intersectional
514 neurons are found, arguing for *Pet1/*5-HT neuron subtype diversity within the caudal DR,
515 consistent with (Kast et al., 2017).

516 It should be noted that the precise anatomical boundaries of the caudal DR (cDR), also
517 referred to as B6 (Dahlstroem and Fuxe, 1964; Jacobs and Azmitia, 1992)), are variably
518 described in the literature. Alonso and colleagues divide B6 into dorsal and ventral sub-
519 compartments, referred to as r1DRd and r1DRv, respectively, where "r1" designates the
520 putative developmental domain of origin of *Pet1* neurons residing in this DR sub-region
521 (i.e. originating from r1, as opposed to isthmus)(Alonso et al., 2013). r1DRv likely
522 corresponds to what others have described as the caudal portion of the "interfascicular"
523 DR (DRI), a medioventral band of DR cells flanked on either side by the medial
524 longitudinal fasciculi. 5-HT neurons of the caudal DRI merge with the more dorsal B6 DR
525 sub-nucleus roughly at the level of the DR where dorsolateral 5-HT neurons become
526 sparse (coronal sections 5 and 6 in **Figure 3**) (Hale and Lowry, 2011; Jacobs and
527 Azmitia, 1992). Depending on the plane and angle of sectioning these caudal DRI cells
528 also appear to merge with MR 5-HT neurons more ventrally, and it has been proposed
529 that caudal DRI cells may be more similar to MR 5-HT neurons developmentally,
530 morphologically, and hodologically than to DR 5-HT neurons (Commons, 2015, 2016;
531 Hale and Lowry, 2011; Jacobs and Azmitia, 1992). In the present study, our designation
532 of cDR is inclusive of r1DRd/r1DRv/caudal DRI/B6, as indicated in **Figure 4A**. Moreover,
533 we do not discount the possibility that this region as drawn partially overlaps with what
534 Alonso and colleagues would call the most dorsal portion of the caudal median raphe
535 (MnRc), as the boundary between the MnRc and r1DRv is poorly defined. Thus, the
536 territory between the cluster of *Met-Vglut3-Tph2-Pet1* neurons beneath the aqueduct in
537 the cDR and the MR is difficult to classify strictly based on cytoarchitecture,
538 underscoring the importance of alternative classification schemes, such as offered by
539 transcriptomics.

540 *Manual scRNA-seq of Pet1-Intersectionally Defined Neuron Populations*

541 Having mapped the spatial distributions of intersectionally labeled *Pet1* neuron
542 subgroups, next we wanted to explore the correspondence of molecular subtype identity
543 with DR subregions more comprehensively. To do this, we microdissected subdomains
544 of the DR in a subset of the intersectional mouse lines just described, dissociated and
545 sorted fluorescently labeled neurons, harvested mRNA from single cells, and prepared
546 scRNA-seq libraries (n = 70 single-cell libraries in total) using the SMART-Seq v4 kit,
547 followed by Illumina sequencing (**Figure 4A**). Specifically, we separately microdissected
548 and manually sorted *Sert::cre;Pet1::Flpe* intersectionally labeled neurons from the

549 dorsolateral DR (dl or dlDR, n = 10 cells), dorsomedial DR (dm or dmDR, n = 9 cells)
550 ventromedial DR (vm or vmDR, n = 8 cells), and caudal DR (cDR, n = 6 cells), as
551 schematized in **Figure 4A**. Additionally, we separately microdissected and manually
552 sorted *Npy2r::cre;Pet1::Flpe* intersectional neurons from the rostral (rDR, n = 9 cells)
553 versus caudal (n = 10 cells) DR, *P2ry1:: cre;Pet1::Flpe* intersectional neurons from the
554 cDR (n = 10 cells) , and *Crh::cre;Pet1::Flpe* intersectional neurons from the rostromedial
555 DR (n = 8 cells). We then used the fourteen *Pet1* neuron subtype identities derived from
556 our 10X scRNA-seq data as a reference to "query" the corresponding identities of our
557 manually sorted and transcriptomically profiled single cells (using the Seurat functions
558 FindTransferAnchors and TransferData as described in (Stuart et al., 2019)). A summary
559 of this analysis is shown in the dot plot in **Figure 4B**. We found that the majority of
560 *Sert::cre;Pet1::Flpe* dlDR neurons mapped to cluster two, with a smaller percentage of
561 single cells mapping to clusters one, three, and six. *Sert::cre;Pet1::Flpe* dmDR neurons
562 were split between clusters two and three, and to a lesser extent four, five, and nine.
563 *Sert::cre;Pet1::Flpe* vmDR neurons mostly corresponded to cluster ten, and were
564 additionally mapped to clusters one, four, seven, and thirteen (note, this may suggest
565 that some *Pet1* neurons expressing little or no *Sert* nor *Tph2* in the adult may yet
566 express the *Sert::cre* transgene). Finally, *Sert::cre;Pet1::Flpe* cDR neurons mapped
567 exclusively to clusters eight and seven (note, cluster twelve neurons do not appear to be
568 well marked by *Sert::cre;Pet1::Flpe;RC::FrePe* eGFP expression – see **Figure 3A5**
569 compared with **Figure 3E5** – perhaps reflecting the lower levels of *Sert* transcripts
570 detected in these neurons).

571 The majority of *Npy2r::cre;Pet1::Flpe* neurons in the rDR were found to correspond to
572 cluster six, with additional mapping to clusters five, seven, ten, and thirteen (consistent
573 with the expression profile of *Npy2r* transcripts in the 10X scRNA-seq data) whereas the
574 majority of *Npy2r:: cre;Pet1::Flpe* neurons from the cDR were found to correspond to
575 cluster seven, with a smaller percentage corresponding to clusters ten and fourteen.
576 *P2ry1::cre;Pet1::Flpe* cDR manually sorted and profiled neurons were mapped
577 exclusively to cluster twelve as expected. *Crh::cre;Pet1::Flpe* profiled neurons were split
578 across clusters in a manner consistent with sporadic *Crh* expression in our 10X scRNA-
579 seq data, however, we found more cluster three than cluster nine *Crh::cre;Pet1::Flpe*
580 neurons, perhaps reflecting that our sampling of this population was biased towards
581 rostromedial DR (or a potential discrepancy between endogenous *Crh* expression and

582 *Crh::cre* expression). Finally, we also included *Drd2::cre;Pet1::Flpe* intersectional
583 scRNA-seq data (n = 17 cells) associated with a previous study from our lab
584 (Niederkofler et al., 2016). *Drd2::cre;Pet1::Flpe* intersectional neurons show a largely
585 dorsolateral and dorsomedial bias within the DR. The majority of these neurons map to
586 clusters three and four, with a much smaller percentage mapping to clusters eight and
587 eleven.

588 Thus combining intersectional genetics, histological analyses, and precisely targeted
589 manual scRNA-seq we were able to infer the anatomical distributions of our fourteen
590 clusters (**Figure 4C**). Clusters one through six and eleven appear to be dorsally, laterally
591 and rostrally biased (to varying degrees), clusters seven, eight, and twelve appear to be
592 caudally biased (as well as cluster fourteen, to a lesser extent), and the remaining
593 clusters appear to be more ventromedial biased in the more rostral DR. Moreover, *Pet1-*
594 *Tph2*^{low} neurons (comprising cluster thirteen) show a prominent enrichment in the
595 medial-rostral DR. Among caudal DR *Pet1* neuron clusters, cluster twelve shows a clear
596 dorsal bias, whereas clusters seven and eight are likely more ventrally biased, based on
597 **Figure 3A5-6, C5-6,** though a nontrivial degree of intermixing of different genetically
598 defined *Pet1* neuron subpopulations in the dorsal cDR is apparent from these images.
599 Expression patterns of cluster marker genes showing strong anatomical biases in our
600 manual scRNA-seq data are depicted in the dot plot in **Figure 4–figure supplement 1** in
601 comparison with our 10X scRNA-seq data.

602 These inferred anatomical distributions of molecularly distinct *Pet1* neuron populations
603 shed further light on the potential developmental significance of transcription factor
604 expression patterns described above. As noted, *Pax5*, a gene associated with isthmic
605 organizer activity during embryonic development (Funahashi et al., 1999; Ye et al.,
606 2001), shows a complementary expression pattern to *Nr2f2*, which encodes a
607 transcription factor that appears to be excluded from the isthmus, but is expressed in r1
608 and other rhombomeres during development, at least in zebrafish (Love and Prince,
609 2012). We further validated the anatomical expression profile of these genes, as well as
610 *Satb2* (expressed by cluster two through four), at the level of protein expression by
611 performing immunohistology in tissue sections prepared from *Vglut3::IRES-*
612 *cre;Pet1::Flpe;RC::FL-hM3Dq* mice (**Figure 4–figure supplement 2 A-E**). Consistent
613 with our anatomically-targeted, manual scRNA-seq data, PAX5 and SATB2 display a
614 rostrodorsal bias in predominately non-*Vglut3*-expressing DR *Pet1* neurons (**Figure 4–**

615 **figure supplement 2B-C,E**), whereas NR2F2 has a ventromedial and caudal
616 expression bias in predominately *Vglut3*-expressing DR *Pet1* neurons (**Figure 4–figure**
617 **supplement 2D,E**). Alonso and colleagues have proposed that cDR *Pet1* neurons are
618 derived from r1 progenitors, whereas more rostral *Pet1* neurons are derived from
619 isthmus (Alonso et al., 2013), however further fate-mapping experiments would be
620 helpful to clarify isthmic versus r1-derived *Pet1* neuron populations (Okaty et al., 2019).
621 Moreover, while rostral DR *Pet1* neurons may derive from isthmus and cDR *Pet1*
622 neurons may derive from r1, our scRNA-seq data nonetheless show substantial *Pet1*
623 neuron molecular heterogeneity within both DR domains, suggesting factors beyond
624 isthmus and r1-lineage driving molecular diversity.

625 **cDR *P2ry1::cre;Pet1::Flpe* neurons display unique hodological and**
626 **electrophysiological properties**

627 Having established correlations between DR *Pet1* neuron molecular expression profiles
628 and anatomical distribution of cell bodies, we next wanted to explore corresponding
629 differences in other cellular phenotypes. We chose to focus on cluster twelve *Met-*
630 *Vglut3-Tph2 Pet1* neurons, captured intersectionally by *P2ry1::IRES-cre;Pet1::Flpe,* as
631 they are the most distinct from other *Pet1* neurons molecularly. To determine if these
632 neurons are likewise unique from other DR *Pet1* neurons with respect to other features
633 we explored the hodological and electrophysiology properties of *P2ry1::cre;Pet1::Flpe*
634 neurons using the intersectional expression of TdTomato (*RC::Ai65*). The anatomical
635 location of cell somata labeled in *P2ry1::IRES-cre;Pet1::Flpe;RC::Ai65* animals was
636 similar to that found in the previously characterized *P2ry1::IRES-*
637 *cre;Pet1::Flpe;RC::FrePe* mice, with a dense population of neurons directly under the
638 aqueduct in the cDR. In addition, there were slightly higher numbers of intersectionally
639 labeled cells in the rostral part of the dorsal raphe as well as scattered cells in the
640 median raphe, consistent with the sporadic expression of *P2ry1* revealed by the present
641 RNA-seq data and the scRNA-seq data of *Pet1* neurons from the MR (Okaty et al.,
642 2015; Ren et al., 2019). Strikingly, most fibers from *P2ry1::cre;Pet1::Flpe;RC::Ai65*
643 neurons were supra-ependymal and were found throughout the third, lateral, and fourth
644 ventricles, a property previously attributed to 5-HT neurons within the cDR (Kast et al.,
645 2017; Mikkelsen et al., 1997; Tong et al., 2014). Sparser fibers were found in regions
646 such as the lateral hypothalamus, medial and lateral septum, hippocampus, olfactory
647 bulb, lateral parabrachial nucleus, and the amygdala. To gain a better perspective of the

648 extent of *P2ry1::cre; Pet1::Flpe;RC::Ai65* fibers in the lateral ventricle we stained for
649 *P2ry1::cre;Pet1::Flpe;RC::Ai65* fibers on a flat mount of the lateral wall as previously
650 described (Mirzadeh 2010). *P2ry1::cre; Pet1::Flpe;RC::Ai65* fibers were found on all
651 aspects of the wall except for the adhesion area, including regions that contain
652 proliferating cells and migrating neuroblasts from the subventricular zone (Mirzadeh et
653 al., 2010)(**Figure 5**). Further, *P2ry1::cre;Pet1::Flpe;RC::Ai65* fibers were closely
654 apposed to proliferating cells (Ki67+) and migrating neuroblasts (doublecortin, DCX+)
655 within the subventricular zone (SVZ) and within the rostral migratory stream (RMS)
656 (**Figure 5**). The proximity of *P2ry1::cre;Pet1::Flpe;RC::Ai65* fibers to adult neural stem
657 cells suggests that they may constitute a serotonergic population of neurons that
658 regulate SVZ proliferation, a process known to be regulated by 5-HT levels and that has
659 previously been associated with the cDR (Aghajanian and Gallager, 1975; Banasr et al.,
660 2004; Brezun and Daszuta, 1999; Hitoshi et al., 2007; Kast et al., 2017; Lorez and
661 Richards, 1982; Mirzadeh et al., 2010; Negoias et al., 2010; Siopi et al., 2016; Soumier
662 et al., 2010; Tong et al., 2014).

663 We next characterized electrophysiological properties of *P2ry1::IRES-cre;*
664 *Pet1::Flpe;RC::Ai65* neurons in comparison with other more broadly defined *Pet1*
665 neuron subpopulations using whole-cell patch clamp in acute slice preparations. As
666 comparison groups we chose: (1) "subtractive" *P2ry1::IRES-cre; Pet1::Flpe;RC*::*FL-*
667 *hM3Dq* neurons in the cDR (i.e. cDR neurons with a history of *Pet1::Flpe* expression but
668 not *P2ry1::IRES-cre* expression; we chose to use *RC*::*FL-hM3Dq* as opposed to
669 *RC::Ai65* or *RC::FrePe* because the subtractive population is identifiable in acute brain
670 slices by eGFP fluorescence without the need for secondary staining), and (2)
671 *Gad2::IRES-cre;Pet1::Flpe;RC::Ai65* neurons from the more rostral and mostly dorsal
672 DR (**Figure 6**). Recording from *P2ry1::IRES-cre;Pet1::Flpe;RC*::*FL-hM3Dq* subtractive
673 cDR neurons allowed us to assess the degree to which electrophysiology may differ
674 within a given DR subdomain depending on molecularly-defined neuron subtype,
675 whereas *Gad2::IRES-cre;Pet1::Flpe;RC::Ai65* neuron recordings provided a comparison
676 group that is both anatomically and molecularly distinct. As demonstrated in the F-I
677 curves in **Figure 6A,** we found that *P2ry1::IRES-cre;Pet1::Flpe;RC::Ai65* neurons have
678 dramatically lower excitability than the two comparison populations, requiring
679 substantially more injected current to reach action potential threshold, and showing a
680 roughly three-fold lower maximum firing rate. Even within the regime of current injection

681 that *P2ry1::IRES-cre;Pet1::Flpe;RC::Ai65* neurons are excitable, we found that they
682 displayed very different spiking characteristics from other *Pet1* neuron groups (**Figure**
683 **6B-F**), specifically showing a longer latency to first action potential (AP, **Figure 6D,F**).
684 Altogether, we observed four distinct firing types exemplified by the voltage traces
685 displayed in **Figure 6B-E**: short-latency to first AP (regular spiking/non-adapting)
686 (**Figure 6B**), mid-latency to first AP (**Figure 6C**), long-latency to first AP (**Figure 6D**),
687 and short-latency to first AP with spike frequency adaptation (**Figure 6E**). The heatmap
688 in **Figure 6F** shows the percentage of single-neuron recordings from each genotype that
689 correspond to a given firing type. **Figure 6-figure supplement 1** displays differences in
690 measured electrophysiological properties when cells are grouped by firing type, as
691 opposed to genotype. All *P2ry1::IRES-cre;Pet1::Flpe;RC::Ai65* neurons recorded (twelve
692 neurons from three animals) showed long latency to first AP, whereas only one out of
693 nine subtractive neurons in the *P2ry1::IRES-cre;Pet1::Flpe;RC*::*FL-hM3Dq* cDR (from
694 three animals) showed this phenotype and none of the *Gad2::IRES-*
695 *cre;Pet1::Flpe;RC::Ai65* neurons (twelve neurons from two animals). These latter two
696 groups of neurons showed greater heterogeneity with respect to firing characteristics, as
697 might be expected given that labeled cells from both genotypes comprise multiple
698 molecular subtypes identified by our scRNA-seq experiments. While the full extent of
699 electrophysiological heterogeneity of these populations is likely under-sampled by the
700 present dataset, the uniqueness of *P2ry1::IRES-cre;Pet1::Flpe;RC::Ai65* neurons
701 nonetheless stands out.

702 **Comparison to other DR scRNA-seq datasets**

703 Recent scRNA-seq studies of mouse DR cell types have been published (Huang et al.,
704 2019; Ren et al., 2019), reporting using either the InDrops platform to profile dissociated
705 DR neurons (Huang et al., 2019) or fluorescence-activated cell sorting to purify
706 dissociated Cre-dependent tdTomato-expressing *Sert::cre* neurons from mouse DR and
707 MR, followed by SMART-Seq v2 library preparation and sequencing (Ren et al., 2019).
708 Huang and colleagues identified six distinct *Pet1*-expressing DR neuron subtypes – five
709 serotonergic and one glutamatergic – while Ren and colleagues identified seven *Pet1*-
710 expressing serotonergic DR neuron subtypes (note they did not identify a glutamatergic
711 *Tph2*^{low} group, presumably because these neurons do not typically express *Sert::cre*). To
712 directly compare our subtype classifications, we used the fourteen *Pet1* neuron subtype
713 identities derived from our 10X scRNA-seq data as a reference to query the

714 corresponding identities of the Huang and Ren datasets (using the Seurat functions
715 FindTransferAnchors and TransferData, as described above for comparison with our
716 manual scRNA-seq data). The results of this analysis are shown in the dot plot in **Figure**
717 **7**. Some *Pet1* neuron subgroup classifications were highly consistent across studies. For
718 example, one hundred percent of single neurons making up the Huang 5-HT V and Ren
719 cDR subgroups map to our cluster twelve *Pet1* neuron subgroup (*Met-Vglut3-Tph2-Pet1*
720 neurons, corresponding to neurons intersectionally captured by *P2ry1::cre;Pet1::Flpe*
721 expression in the cDR shown in **Figure 3E**). Likewise, there is high correspondence
722 between Huang 5-HT I, Ren DR 1, and our cluster-two *Pet1*-neuron subgroup
723 (dorsolateral DR *Gad2-Trh-Tph2-Pet1* neurons). Huang 5-HT II and Ren 2 subgroups
724 are largely split between our cluster two and cluster three subgroups, with a smaller
725 portion of each mapping to our cluster four subgroup (which also corresponds to a small
726 subset of Huang 5-HT I and Ren DR 1 neurons). Huang 5-HT III and Ren DR 3
727 correspond to our cluster five and six subgroups, with a larger percentage of Huang 5-
728 HT III neurons mapping to cluster five and a larger percentage of Ren DR 3 neurons
729 mapping to cluster six.

730 In other cases, there is better correspondence between our identified *Pet1* neuron
731 subgroups and one or the other study, likely due in part to technological differences
732 between studies. For example, Huang Glu V corresponds well with our cluster thirteen
733 *Pet1* neuron subgroup (*Vglut3-Tph2*^{low}*-Pet1* neurons) but very few neurons profiled in
734 the Ren study map to cluster thirteen. As mentioned above, the absence of a prominent
735 glutamatergic *Tph2*^{low} group of neurons in the Ren study likely stems from the fact that
736 the low level of *Sert* transcription in these neurons does not reliably drive *Sert::cre*
737 transgene expression and thus reporter expression for their cell sorting. However, the
738 fact that a small number of *Sert::cre* expressing neurons from the Ren study do map to
739 our cluster thirteen subgroup indicates that there may be exceptions (moreover, these
740 cells may more specifically map to cluster thirteen neurons at the higher end of the
741 distribution of *Sert* and *Tph2* transcript levels **Figure 1–figure supplement 3**).

742 On the other hand, Ren DR 6 corresponds well with our cluster one subgroup (*Npas1/3-*
743 *Tph2-Pet1* neurons) and Ren DR 4 corresponds well with our cluster nine subgroup
744 (*Maf-Nos1-Tph2-Pet1* neurons), but there is no such one-to-one correspondence
745 between these groups and the neuron groups identified in the Huang study. Rather,
746 cluster one and cluster nine neurons get “pulled” from other groups identified by Huang.

747 This likely reflects the different sensitivities of the various approaches. Specifically, our
748 study and the Ren study achieved more than three-fold higher gene detection per single
749 cell library on average than the Huang study, thus allowing for finer-scale molecular
750 subgroup classification. However our higher single-cell sampling resolution – we profiled
751 2,350 DR *Pet1* neurons, whereas Huang and Ren each profiled roughly seven hundred
752 DR *Pet1* neurons – ultimately allowed us to resolve more subgroups. Huang 5-HT IV
753 and Ren DR 5 show the greatest degree of dispersion into different clusters identified in
754 our study. Ren DR 5 is split predominately between clusters seven, ten, and fourteen,
755 while Huang 5-HT IV is split into clusters ten and fourteen, as well as across several
756 other clusters. Importantly, our higher number of identified clusters does not appear to
757 stem from analytic differences between studies *per se*, given that we identified more
758 clusters using a lower resolution parameter in our clustering analysis than the other two
759 studies. Huang, et al. reported using a Seurat FindCluster resolution of 2.0, Ren, et al.
760 used a resolution of 1.0, whereas the highest resolution we used was 0.9.

761 Lastly, we also found that Ren MR 1 (identified as being a median raphe 5-HT neuron
762 subtype in that study) shows striking similarity to our cluster eight subgroup, which we
763 have mapped to the cDR based on histology and our manual scRNA-seq data. As
764 described above, the boundary between the cDR and the MR, specifically the portion of
765 the MR attributed to r1-derived neurons (Alonso et al., 2013; Okaty et al., 2015), is
766 poorly defined, thus Ren MR 1 and our cluster eight neurons may indeed partially
767 overlap anatomically. Notably, some Huang 5-HT IV neurons (microdissected from what
768 was considered the DR in that study) also map to our cluster eight subgroup.

769 **Discussion**

770 The dorsal raphe nucleus is likely one of the most extensively connected hubs in the
771 mammalian brain. Efferent DR fibers, predominantly serotonergic (but also glutamatergic
772 and GABAergic), collectively innervate much of the forebrain and midbrain, as well as
773 some hindbrain nuclei (Azmitia and Segal, 1978; Bang and Commons, 2012; Bang et al.,
774 2012; Beaudet and Descarries, 1976; Fernandez et al., 2016; Gagnon and Parent, 2014;
775 Hale and Lowry, 2011; Kast et al., 2017; Kosofsky and Molliver, 1987; Lidov et al., 1980;
776 Lidov and Molliver, 1982; Maddaloni et al., 2017; McDevitt et al., 2014; Molliver, 1987;
777 Muzerelle et al., 2016; O'Hearn and Molliver, 1984; Prouty et al., 2017; Ren et al., 2018;
778 Steinbusch, 1981; Steinbusch et al., 1980; Vasudeva et al., 2011; Vertes, 1991; Vertes

779 and Kocsis, 1994), and DR afferents have been identified from as many as eighty
780 distinct anatomical brain regions, including other brainstem raphe nuclei (Celada et al.,
781 2001; Commons, 2015; Goncalves et al., 2009; Levine and Jacobs, 1992; Mosko et al.,
782 1977; Ogawa et al., 2014; Peyron et al., 1998; Peyron et al., 2018; Pollak Dorocic et al.,
783 2014; Weissbourd et al., 2014). As such, the DR is hodologically poised to broadcast
784 and receive signals related to a wide range of sensory, motor, affective, and cognitive
785 processes. Indeed, DR neuropathology is associated with several human disorders (or
786 disease models thereof) with broad symptomatology, such as major depressive disorder,
787 autism, and Alzheimer's disease (Chen et al., 2000; Dengler-Crish et al., 2017; Ellegood
788 et al., 2015; Guo and Commons, 2017; Ji et al., 2020; Luo et al., 2017; Michelsen et al.,
789 2008; Miyazaki et al., 2005; Simic et al., 2017; Vakalopoulos, 2017; Wang et al., 2018;
790 Zweig et al., 1988). Outside of DR-specialist research, the DR has often been viewed by
791 the wider neuroscience community as a "black box" source of a single neurochemical,
792 namely 5-HT. Accordingly, development of therapeutics for associated disorders has
793 largely focused on modulating overall serotonergic tone. However, DR-focused research
794 over several decades has revealed layers of functional complexity and compositional
795 heterogeneity warranting a more nuanced view (reviewed in (Abrams et al., 2004;
796 Andrade and Haj-Dahmane, 2013; Gaspar and Lillesaar, 2012; Hale and Lowry, 2011;
797 Michelsen et al., 2007; Okaty et al., 2019; Vasudeva et al., 2011)). While these studies
798 have reached into the black box of the DR and described a variety of features at different
799 levels of observation, integration across levels to arrive at principles of DR organization
800 has proved challenging. Elucidating how molecular, neurochemical, anatomical,
801 hodological, electrophysiological, and functional descriptions of the DR overlap is
802 essential to understanding the structure-function relationship of the DR and other raphe
803 nuclei (Brust et al., 2014; Fernandez et al., 2016; Huang et al., 2019; Kast et al., 2017;
804 Niederkofler et al., 2016; Okaty et al., 2015; Prouty et al., 2017; Ren et al., 2018; Ren et
805 al., 2019), and will likely facilitate improved therapies for human disorders. Here we have
806 focused on one broadly defined subgroup of DR cells – neurons that express the gene
807 *Pet1/Fev* – and applied scRNA-seq, iterative intersectional genetics, histology, and slice
808 electrophysiology to provide a transcriptomic and anatomic atlas of mouse DR *Pet1*
809 neurons with examples of links between molecular, neurochemical, anatomical,
810 hodological, and electrophysiological levels of description. We identify as many as
811 fourteen distinct molecularly defined subtypes of *Pet1* neurons that show biased cell
812 body distributions in DR sub-regions. We further characterize projections and

813 electrophysiology of the most molecularly unique DR *Pet1* neuron subtype – *Met-Vglut3-*
814 *Tph2-Pet1* cDR neurons (cluster twelve), genetically accessed by intersectional
815 *P2ry1::cre;Pet1::Flpe* expression. The present study complements other recent
816 characterizations of DR cell types (Huang et al., 2019; Ren et al., 2019), increasing the
817 sampling resolution of *Pet1* neurons in particular through our experimental approach to
818 achieve fine-scale identification of *Pet1* neuron subtypes.

819 ***Molecular and anatomic organization of Pet1 neuron subtypes***

820 Our data and analysis highlight the hierarchical organization of DR *Pet1* neurons
821 molecularly and anatomically, allowing for identification of features that organize *Pet1*
822 neurons at different levels of granularity (**Figure 8**). Neurochemistry has long served as
823 a principal phenotypic axis for classifying neurons, and concordantly we found that
824 distributions of transcripts associated with distinct neurotransmitters correspond with
825 broad subgroup divisions. The majority of *Pet1* neurons (clusters one through twelve)
826 express high levels of *Tph2* mRNA, encoding tryptophan hydroxylase two, the rate-
827 limiting biosynthetic enzyme for 5-HT, as well as several other genes indicative of a
828 serotonergic phenotype, such as *Slc6a4* (*Sert*), *Slc18a2* (*Vmat2*), and *Maob*. However,
829 we also identified two subgroups of *Pet1* neurons with 5-HT marker gene profiles that
830 differ from the majority (clusters thirteen and fourteen). One subgroup (cluster thirteen)
831 expresses very low transcript levels of 5-HT neuron marker genes, is mostly negative for
832 TPH2 immunolabeling, and shows a biased cell body distribution in the rostromedial DR,
833 as well as distributing sporadically throughout. The other subgroup (cluster fourteen)
834 exhibits a much broader distribution of transcript levels for 5-HT marker genes than other
835 groups. The functional significance of this variable expression can only be hypothesized
836 at present; we speculate that it may reflect a capacity for neurotransmitter plasticity – i.e.
837 experience-dependent induction or up-regulation of 5-HT phenotype, as hinted at by a
838 recent study (Prakash et al., 2019). If this is the case, cluster fourteen neurons may be
839 partially in transition, for example, from a predominately glutamatergic phenotype to a 5-
840 HT phenotype or to a glutamate-5-HT co-transmitter phenotype. Both cluster thirteen
841 and fourteen *Pet1* neuron subgroups express *Slc17a8* (*Vglut3*) transcripts, suggestive of
842 a capacity for synaptic glutamate packaging and release, and show shared enrichment
843 for several transcripts, including *Ldb2*, encoding the transcription factor LIM domain
844 binding 2, and *Cnr1*, encoding cannabinoid receptor 1. Cluster fourteen is also uniquely

845 distinguished by enrichment for *Gpr101* transcripts, encoding an orphan G protein-
846 coupled receptor.

847 Among *Pet1* neurons expressing high levels of *Tph2* and other 5-HT gene markers,
848 expression of genes related to GABA synthesis (*Gad1* and *Gad2*) or glutamatergic
849 synaptic vesicle packaging (*Vglut3*) correlate with major molecular and anatomical
850 subdivisions (evident in the dendrogram in **Figure 1B**, the UMAP plot in **Figure 1C**, and
851 the histological image series in **Figure 3 B1-6 and Figure 3 – figure supplement 1D-**
852 **J**). We found that the cell bodies of non-*Vglut3*, largely *Gad2*-expressing *Pet1* neurons
853 are preferentially distributed in the dorsal and lateral sub-regions of the rostral DR, and
854 become exclusively lateral and ultimately absent at more caudal extents of the DR.
855 Conversely, *Vglut3-Tph2-Pet1* neuron bodies show a ventromedial bias rostrally and
856 predominate the entire cDR. *Gad2-Tph2-Pet1* neurons and *Vglut3-Tph2-Pet1* neurons
857 show differential enrichment of hundreds of transcripts, including *Pax5* and *Nr2f2*. Both
858 genes encode transcription factors, the expression of which we examined through
859 immunohistology and found a similar distribution of cell body staining as revealed by
860 intersectional genetic labeling of *Vglut3::cre;Pet1::Flpe* neurons – *Pax5* expression
861 overlaps predominately with the non-*Vglut3*-expressing population, whereas *Nr2f2*
862 overlaps with the *Vglut3*-expressing population (**Figure 4 – figure supplement 2**). We
863 also found one *Pet1* neuron subgroup (cluster six) that expresses *Gad1*, *Gad2*, and
864 "intermediate" levels of *Vglut3* transcripts (relative to other *Vglut3*+ clusters). These
865 neurons correspond with the rostral population of neurons labeled by intersectional
866 *Npy2r::cre;Pet1::Flpe* expression (**Figure 3C**), which we characterized by manual
867 scRNA-seq (**Figure 4**).

868 Altogether we identified five *Pet1* neuron subgroups that express *Gad1* or *Gad2*
869 transcripts (clusters two through six), and found *Gad2* to be expressed more consistently
870 and at higher levels than *Gad1* (with the exception of cluster six). *Gad1* and *Gad2*
871 encode two distinct isoforms of glutamate decarboxylase, referred to as GAD67 and
872 GAD65, respectively. In many neuron types, these proteins are often co-expressed, but
873 localize to different subcellular compartments and differ in their interaction with the co-
874 factor pyridoxol phosphate (Chen et al., 2003; Erlander et al., 1991; Soghomonian and
875 Martin, 1998). GAD65 (encoded by *Gad2*) is typically found in axon terminals where it is
876 thought to play a role in GABA synthesis specifically for synaptic vesicular release,
877 whereas GAD67 is typically localized to the soma and may be more involved with non-

878 vesicular GABA release. While we did not reliably detect transcripts for the vesicular
879 GABA transporter (*Slc32a1*), we did detect expression of transcripts encoding VMAT2
880 which has been shown to package GABA into synaptic vesicles in dopaminergic
881 neurons, allowing for monoaminergic-GABAergic co-transmission (Tritsch et al., 2012).
882 Thus it is plausible that *Gad2-Tph2-Pet1* neurons may likewise co-release GABA,
883 though it has yet to be reported in the literature.

884 Beyond classic neurotransmitters, we also found enrichment of various peptide hormone
885 transmitters in different *Gad2-Tph2-Pet1* neuron subgroups. Cluster two shows
886 enrichment for thyrotropin-releasing hormone transcripts (*Trh*), and clusters five and six
887 show enrichment for prodynorphin (*Pdyn*) (as does cluster fourteen). As can be seen in
888 the dendrogram in **Figure 1B** and UMAP plot in **Figure 1C**, there appears to be a major
889 division between *Gad2-Tph2-Pet1* clusters two through four and clusters five and six,
890 with clusters five and six also sharing many molecular similarities with *Vglut3-Tph2-Pet1*
891 subgroups. This may in part reflect differential expression of transcription factors that
892 regulate divergent gene "modules". While all *Gad2-Tph2-Pet1* neurons express *Pax5*,
893 clusters two through four also express *Sox14* and *Satb2*. Cluster six, on the other hand,
894 shows enrichment for several transcription factor genes that are also enriched (or trend
895 towards enrichment) in clusters thirteen and fourteen, such as *Pou3f2*, *Bcl11a*, and *Id2*.
896 These molecularly distinct *Gad2-Tph2-Pet1* subgroups also show differences in
897 anatomy. Based on manual scRNA-seq of sub-anatomically targeted *Pet1* neurons, we
898 found that cluster two *Gad2-Trh-Tph2-Pet1* neuron cell bodies are found predominately
899 in the dorsolateral DR, as well as the dorsomedial DR, whereas clusters three, four, and
900 five appear to be more dorsomedially biased, consistent with recent reports (Huang et
901 al., 2019; Ren et al., 2019). Cluster six neurons, as captured by *Npy2r::cre;Pet1::Flpe*
902 expression, show a more diffuse distribution in the rostral DR, illustrating that not all *Pet1*
903 neuron subtypes, as defined transcriptomically, correspond with clear-cut anatomical
904 patterns. Indeed, while there are major differences between predominately dorsal versus
905 ventral or rostral versus caudal DR *Pet1* neuron subtypes, different subtypes
906 nonetheless intermix within these domains, emphasizing the importance of molecular-
907 genetic targeting of *Pet1* neuron subtypes to gain specificity for functional
908 characterization (a point also made by (Huang et al., 2019) and (Okaty et al., 2019)).

909 *Vglut3-Tph2-Pet1* neuron subgroups, as noted above, are found more ventrally than
910 *Gad2-Tph2-Pet1* neurons in the rostral DR, and are the dominant neurotransmitter

911 phenotype in the caudal DR (as inferred by transcript expression and VGLUT3 and
912 TPH2 immunostaining). We found two *Vglut3-Tph2-Pet1* neuron subtypes with cell
913 bodies biased towards the rostral DR (clusters nine and ten) and three subtypes
914 (clusters seven, eight, and twelve) biased towards the more caudal DR (as delineated in
915 **Figure 4**, and see the discussion of varying nomenclature around the cDR in the
916 **Results** section *Histology of Pet1-Intersectionally Defined Neuron Populations* above).
917 Cluster twelve *Pet1* neurons, also marked by expression of the gene *Met*, we found to
918 be the most different from all other *Pet1* neurons, both in terms of the number of
919 differentially expressed genes and the magnitudes of enrichment/depletion compared to
920 other *Pet1* neuron subtypes (as also observed by (Huang et al., 2019; Ren et al., 2019)).
921 We show by histology of genetically marked neurons (intersectional
922 *P2ry1::cre;Pet1::Flpe* expression) that the cell bodies of these *Met-Vglut3-Tph2-Pet1*
923 neurons are clustered beneath the aqueduct in the caudal DR (**Figure 3E**) and send
924 extensive axonal projections throughout the ventricles (**Figure 5**). Based on retrograde
925 tracing experiments (Kast et al., 2017; Tong et al., 2014), it is likely that these neurons
926 constitute the major source of 5-HT innervation to the ventricles. Furthermore, our
927 demonstration that *P2ry1::cre;Pet1::Flpe* fibers are closely apposed with proliferating
928 and migrating cells in the SVZ and rostral migratory stream (**Figure 5**), supports a
929 proposed role for these neurons in regulating adult neural stem cell proliferation in the
930 SVZ (Tong et al., 2014). Cluster twelve neuron transcript enrichment for several GPCRs
931 implicated in modulation of adult neurogenesis, such as *P2ry1* (Lin et al., 2007)*, Gipr*
932 (found to be enriched in our *P2ry1::cre;Pet1::Flpe* manual scRNA-seq data) (Nyberg et
933 al., 2005)*, S1pr3* (Alfonso et al., 2015; Ye et al., 2016)*,* and *Oprm1* (Harburg et al., 2007)
934 lends further support to this hypothesis. Now, with intersectional access to this
935 population of cDR 5-HT neurons provided by *P2ry1::IRES-cre* with *Pet1::Flpe,* the
936 function of *Met-Vglut3-Tph2-Pet1* cDR neurons in regulating SVZ proliferation can be
937 tested directly in a cell type-specific manner using dual Cre- and Flpe- responsive
938 chemo- or optogenetic approaches (Brust et al., 2014; Hennessy et al., 2017; Kim et al.,
939 2009; Madisen et al., 2015; Niederkofler et al., 2016; Okaty et al., 2015; Ray et al., 2011;
940 Sciolino et al., 2016; Teissier et al., 2015).

941 **DR *Pet1* neuron subtypes have distinct electrophysiological properties**

942 To further characterize correspondence of molecular identities with other cell
943 phenotypes we performed whole-cell electrophysiological recordings in acute slices

944 prepared from mice in which different *Pet1* neuron subsets were genetically labeled. We
945 found that 5-HT neurons with different molecular identities also exhibit distinct
946 electrophysiological properties likely to impact their circuit function. While we did not
947 comprehensively sample all molecularly defined subtypes, our survey of cDR *Pet1*
948 neurons and rostrodorsal *Gad2::cre;Pet1::Flpe* neurons provides evidence for at least
949 four distinct electrophysiological types based on four key properties: (1) rheobase (also
950 known as current threshold), which reflects a neuron's sensitivity to input, (2) delay to
951 first spike, which reflects the degree to which a neuron is able to activate phasically in
952 response to input, (3) spike-frequency adaptation, which reflects the degree to which a
953 neuron is able to continuously signal ongoing input, and (4) maximum firing rate, which
954 determines the dynamic range of neuron responsiveness to graded inputs. As with
955 molecular differences, cluster twelve *Met-Vglut3-Tph2-Pet1* cDR neurons
956 (*P2ry1::cre;Pet1::Flpe* intersectional expression) showed profound differences from
957 other subtypes, including other cDR *Pet1* neurons. *P2ry1::cre;Pet1::Flpe* neurons
958 consistently displayed a long latency to first action potential, required substantially more
959 input to reach action potential threshold, and had a lower maximum firing rate (**Figure 6**
960 **and Figure 6 – figure supplement 1**). These differences, together with differential
961 transcript expression of several GPCRs, suggest that *Met-Vglut3-Tph2-Pet1* cDR
962 neurons respond in a different way and to very different stimuli than other DR *Pet1*
963 neuron types. For example, low excitability and long-latency to spike suggest that these
964 neurons may only be recruited by very strong stimuli at relatively slower timescales than
965 other *Pet1* neurons (to the extent that properties recorded in slice reflect *in vivo*
966 properties). Notably, 5-HT neurons with this electrophysiological profile have not yet
967 been reported in the literature. However, the two firing types that we have defined as
968 "Short-Latency to First AP; Non-Adapting" and "Mid-Latency to First AP" (**Figure 6B,C**)
969 correspond well to those described by (Fernandez et al., 2016) in groups of *Pet1-eGFP*
970 serotonergic neurons projecting to the mPFC and the BLA, respectively. Differential
971 expression of ion channels and receptors identified here suggest molecular substrates of
972 these different electrophysiological properties.

973 **Technical aspects of our study allow for high-resolution transcriptome**
974 **characterization of *Pet1* neurons**

975 Due to the high-dimensional "richness" of transcriptomic data, together with the capacity
976 to propose explanations of cellular phenotypes in terms of molecular mechanisms –

977 RNA-seq dissection of neural circuits has gained traction as a way to define and
978 enumerate cell types in the brain (and other tissues). Single-cell RNA-sequencing, in
979 particular, has become an indispensable approach, with different methods achieving
980 different resolution of underlying cellular diversity (Bakken et al., 2018; Campbell et al.,
981 2017; Hodge et al., 2019; Huang et al., 2019; Lovatt et al., 2014; Macosko et al., 2015;
982 Okaty et al., 2015; Poulin et al., 2016; Ren et al., 2019; Rosenberg et al., 2018;
983 Saunders et al., 2018; Spaethling et al., 2014; Tasic, 2018; Tasic et al., 2016; Tasic et
984 al., 2018; Usoskin et al., 2015; Zeisel et al., 2018; Zeisel et al., 2015). Droplet-based
985 scRNA-seq approaches (without cell-type-specific purification) allow for unbiased
986 classification of major cell types residing in a particular microdissected tissue region of
987 interest, however lower abundance cell types, such as DR *Pet1* neurons profiled in the
988 present study, are often insufficiently sampled to achieve high resolution of subtype
989 molecular diversity. Moreover, different reaction chemistries employed in different
990 droplet-based scRNA-seq approaches can lead to different gene detection sensitivity.
991 Low cellular abundance compounded with low gene detection can greatly limit the power
992 of a study to reveal fine-scale variation in molecular phenotypes that may be important
993 for identifying neuronal subtypes and subtype "states" (e.g. adaptive or pathological
994 transcriptional variation). Where cell type-specific markers are available, cell sorting prior
995 to scRNA-seq library preparation can greatly enhance the resolution of cellular diversity
996 for less abundant cell classes. While manual sorting approaches combined with RNA-
997 seq library preparation optimized for low amounts of input RNA achieve high single-cell
998 gene detection and allow for sampling genetically and anatomically-defined neuron
999 populations (Niederkofler et al., 2016; Okaty et al., 2015), they are often limited in the
1000 number of cells profiled, and therefore may lack sufficient throughput to fully characterize
1001 subtype diversity. On the other hand, automated sorting approaches achieve greater
1002 throughput but are less well suited to collecting low abundance cell types, such as
1003 defined by fine-scale anatomy or highly restricted marker gene expression. Our
1004 particular experimental approach to characterizing DR *Pet1*-lineage neuron diversity in
1005 the present study was informed by all of the above concerns. By combining
1006 intersectional genetic labeling of DR *Pet1* neurons with both high-throughput
1007 (microfluidic On-chip Sort) and targeted low-throughput (manual) sorting approaches,
1008 followed by high-sensitivity RNA-seq library preparation protocols (10X Genomics
1009 Chromium Single Cell 3' v3 and SMART-Seq v4 kits, respectively) we leveraged the

1010 strengths of multiple approaches to achieve high-resolution transcriptomic profiling of DR
1011 *Pet1* neurons.

1012 ***Resource value of DR Pet1 neuron scRNA-seq data***

1013 While we have highlighted many salient experimental findings in the present report, the
1014 data no doubt have more to reveal, and we thus offer this dataset as a resource to be
1015 mined by the larger community in the hopes that it may facilitate and stimulate future
1016 studies. For example, newly identified *Pet1* neuron subtype marker genes may guide
1017 development of new recombinase driver lines allowing for subtype-specific genetic
1018 access, or shape approaches for developing more targeted therapeutics. Moreover, we
1019 hope this work, together with other recent studies (Huang et al., 2019; Ren et al., 2019),
1020 may lead to the development of a standardized DR *Pet1* neuron subtype nomenclature
1021 that allows for consolidation of results across different labs and different data modalities.

1022 **Methods**

1023 **Intersectional genetic fate mapping**

1024 Triple transgenic mice were generated by crossing *Pet1::Flpe; FrePe* (Brust et al., 2014;
1025 Jensen et al., 2008; Okaty et al., 2015) or *Pet1::Flpe; Ai65* (Madisen et al., 2015) mice
1026 with *Sert::cre* (Gong et al., 2007), *Npy2r::IRES-cre* (Chang et al., 2015), *En1::cre*
1027 (Kimmel et al., 2000), *Crh::cre*
1028 (https://www.mmrrc.org/catalog/sds.php?mmrrc_id=30850), and *P2ry1::IRES-cre*
1029 (Chang et al., 2015) mice, or by crossing *Pet1::Flpe; hM3Dq* (Sciolino et al., 2016) mice
1030 with *Vglut3::IRES-cre* mice (https://www.jax.org/strain/028534). All animals were group
1031 housed on a 12hr light/dark cycle with access to food and water ad libitum and were
1032 handled and euthanized in accordance with Harvard's Institutional Animal Care and Use
1033 Committee Protocols.

1034 **Perfusion and immunohistochemistry**

1035 Anesthetized mice were transcardially perfused with cold phosphate-buffered saline
1036 (PBS) followed by 4% paraformaldehyde (PFA) overnight. Tissue was dissected and
1037 fixed in 4% PFA overnight followed by cryoprotection in 30% sucrose/PBS until
1038 equilibrated (~48 hours) before being frozen in tissue freezing medium (Triangle

1039 Biomedical Services). Tissue was cryosectioned in 40um coronal sections and
1040 processed as floating sections.

1041 For fluorescent staining, sections were washed with PBS and PBS with 0.1% Triton-X-
1042 100 (PBS-T), blocked in 5% normal donkey serum (NDS) and 1% bovine serum albumin
1043 (BSA) for 2 hours at room temperature (RT), and incubated with primary antibody at 4°C
1044 for 48 hours: anti-GFP (1:3000, chicken polyclonal, Aves Labs, GFP-1020), anti-DsRed
1045 (1:1000, rabbit polyclonal, Takara, 632496), anti-TPH2 (1:1000, rabbit polyclonal, Novus
1046 Biologicals, NB100-74555), anti-Pax5 (1:1000, goat polyclonal, Santa Cruz, sc-1974),
1047 anti-SATB2 (1:1000, guinea pig polyclonal, Synaptic Systems, 327-004), anti-COUP-TFII
1048 (1:1000, mouse monoclonal, Perseus Proteomics, PP-H7 147-00), anti-ZEB2 (1:200,
1049 rabbit polyclonal, MyBioSource, MBS9601451), anti-VGLUT3 (1:500, guinea pig
1050 polyclonal, Synaptic Systems, 135-204), anti-RFP (1:500, rat monoclonal, Chromotek,
1051 5f8-100), anti-Doublecortin (1:1000, goat polyclonal, Santa Cruz, SC-8066), and anti-Ki-
1052 67(1:1000, rat monoclonal, Invitrogen, 14-5698-80). For fluorescent detection, sections
1053 were washed in PBS-T and incubated with species matched secondary antibodies-
1054 Alexa Fluor 488 (donkey anti-chicken, Jackson, 703-545-155), Alexa Fluor 546 (donkey
1055 anti-rabbit, Invitrogen, A10040), Alexa Fluor 647 (donkey anti-goat, Invitrogen, A21447
1056 or donkey anti-mouse, Jackson, 715-605-151), and Cy5 (donkey anti-guinea pig,
1057 Jackson, 706-175-148)- at 1:500 dilution for two hours. Sections were washed in PBS
1058 and 1:3000 DAPI before rinsing and mounting onto slides.

1059 **Confocal and fluorescent microscopy and quantification**

1060 Overview images**:** Overview images of intersectional subtypes were acquired using a 5x
1061 objective on a Zeiss Axioplan2 fluorescence microscope equipped with an Axiocam
1062 digital camera and Axiovision software using 1x1 binning. Images were then cropped to
1063 a 1000x1000 pixel square containing the dorsal raphe. Images showing the distribution
1064 of PAX5, SATB2, and NR2F2 are 2x2 tiled maximum intensity images acquired using a
1065 Plan Apo λ 20x/0.75 DIC I objective on a spinning disk confocal. Images showing TPH2
1066 and VGLUT3 staining are a single optical slice taken on a spinning disk confocal using a
1067 Plan Apo λ 20x/0.75 DIC I objective or Plan Fluor 40x/1.3 Oil DIC H/N2 objective
1068 respectively. Images were cropped to create a zoomed image of the region of interest.

1069 Quantification: Quantification of PAX5, NR2F2, and SATB2 was completed in
1070 *Vglut3::IRES-cre; Pet1::Flpe; hM3Dq* animals, where cells expressing both
1071 *Vglut3::IRES-cre* and *Pet1::Flpe* express an hM3Dq-mCherry fusion and all other *Pet1+*
1072 cells express eGFP. Images were acquired as 2x2 tiles as a z-stack (0.9um step) using
1073 a Plan Apo λ 20x/0.75 DIC I objective on a spinning disk confocal and cropped into
1074 equally sized non-overlapping subregions (1000x1000 pixel) spanning the rostral to
1075 caudal extent of the dorsal raphe. Cells were counted positive if antibody staining for the
1076 protein of interest overlapped with DAPI staining and was within a DsRed + cell
1077 (*Vglut3::cre;Pet1::Flpe* lineage) or a GFP+ cell (subtractive *Pet1* lineage). All counts
1078 were completed in images taken from 2 to 4 animals depending on the brain region.
1079 Images used for the quantification of VGLUT3 antibody staining were acquired using a
1080 Plan Fluor 40x/1.3 Oil DIC H/N2 objective on a spinning disk confocal on non-
1081 overlapping anatomical subdivisions of the dorsal raphe. Cells were counted positive
1082 based on the overlap of VGLUT3 antibody staining with mCherry (*VGlut3::cre;Pet1::Flpe*
1083 lineage) or a eGFP (subtractive *Pet1* lineage) staining. In the case of TPH2
1084 quantification, *En1::cre; Pet1::Flpe; FrePe* animals were used (eGFP+ *En1::cre;*
1085 *Pet1::Flpe* intersectional lineage cells). Images were acquired as 2x2 tiles as a z-stack
1086 (0.9um step) using a Plan Apo λ 20x/0.75 DIC I objective on a spinning disk confocal
1087 and cropped into equally sized non-overlapping subregions (1000x1000 pixel) spanning
1088 the rostral to caudal extent of the dorsal raphe. Cells were counted positive based on
1089 colocalization of TPH2 antibody staining with eGFP. All quantification was performed by
1090 an experienced observer blinded to the anatomical region of the image in a minimum of
1091 two animals per region.

1092 Flat mount of lateral wall of lateral ventricle: *P2ry1::IRES-cre; Pet1::Flpe; Ai65* mice
1093 (n=4) were transcardially perfused with cold PBS. Lateral wall dissection was completed
1094 as described in Mirzadeh, et.al, 2010. Briefly, brains were dissected into PBS and split
1095 into two hemispheres. The hippocampus was removed, exposing the lateral wall, and
1096 the brain was fixed overnight in 4% PFA in PBS. The remainder of the microdissection of
1097 the lateral wall was then completed and immediately proceeded to
1098 immunohistochemistry as described above.

1099 **Single-cell sorting and RNA sequencing**

1100 On-chip Sort, 10X library preparation, and RNA sequencing: Data was derived from two
1101 different experiments composed of brain tissue harvested from *En1::cre; Pet1::Flpe;*
1102 *FrePe* mice (n=4) or *Pet1::Flpe; RC::FL-hM3Dq* mice (n=6). Tissue was sectioned on a
1103 vibratome and protease-digested in ACSF containing activity blockers as described in
1104 (Hempel et al., 2007). The dorsal raphe was micro-dissected under an upright dissection
1105 microscope with fluorescence optics and all tissue was combined in a 1.5mL Eppendorf
1106 tube containing 500ul of filtered ACSF/1%FBS. Tissue was then gently triturated using
1107 glass micropipettes of decreasing diameter until achieving a mostly homogeneous
1108 single-cell suspension without visible tissue chunks. One drop of NucBlue (Thermo
1109 Fisher Scientific) was added to the cell suspension and allowed to sit for 20 minutes (to
1110 aid in sorting and cell quantification). EGFP-marked, NucBlue-positive cells were sorted
1111 using the On-chip Sort (On-chip Biotechnologies Co., Ltd.). Final cell concentration was
1112 determined by counting the number of cells in 10ul of the sorted output using a
1113 hemacytometer. Cells were then run through the 10X Genomics Chromium Single Cell 3'
1114 v3 protocol, and libraries were sequenced on an Illumina NextSeq 500 sequencer to a
1115 mean depth of ~115,000 reads per cell.

1116 Manual Sorting and RNA sequencing: Brain tissue was harvested from triple transgenic
1117 animals – *Sert::cre;Pet1::Flpe;FrePe*, *Npy2r::IRES-cre Pet1::Flpe;FrePe,*
1118 *Crh::cre;Pet1::Flpe;FrePe,* and *P2ry1::IRES-cre* (p60-p120, a minimum of two mice per
1119 condition) and fluorescently labeled cells were sorted as described in (Okaty et al.,
1120 2015). Briefly, the brainstem was sectioned into 400um coronal sections using a
1121 vibratome. Sections were bubbled in artificial cerebrospinal fluid (ACSF) containing
1122 activity blockers for at least 5 minutes before being transferred to ACSF containing
1123 1mg/ml pronase for 1 hour. Slices were then returned to protease-free ACSF for 15
1124 minutes, before regions of interest were micro-dissected. Anatomical subdivisions of the
1125 dorsal raphe were made based on the shape of the dorsal raphe and landmarks
1126 including fiber tracts and the aqueduct (as indicated in **Figure 4A**). Dissected chunks of
1127 tissue were transferred first to a clean 35-mm dish containing ACSF and then to a 1.5mL
1128 Eppendorf tube containing 1mL of filtered ACSF/1% FBS. Tissue was then gently
1129 triturated until without visible chunks. Dissociated cells were diluted and poured into a
1130 Petri dish. Fluorescently marked cells were aspirated using mouth aspiration and moved
1131 into 3 consecutive wash dishes. Each cell was then aspirated a final time and deposited
1132 into an individual 0.5mL tube containing 9.5ul of nuclease-free water and 1ul of 10x

1133 Reaction Buffer (Smart-Seq V4 Ultra Low Input RNA kit, Takara Bio) and allowed to
1134 incubate at room temperature for 5 minutes before being stored at -80deg until cDNA
1135 synthesis. Single cells were converted to cDNA and amplified using Smart-Seq V4 Ultra
1136 Low Input RNA Kit (Takara Bio). The cDNA output was then processed with Nextera XT
1137 DNA Library Preparation Kit. Quantification and quality control were assessed with
1138 TapeStation. Libraries were then sequenced on either an Illumina HiSeq 2500 (50 base-
1139 pair, single-end) or NextSeq 500 (75-bp, paired-end) to a mean depth of ~4,000,000
1140 reads per cell.

1141 **scRNA-seq Analysis**

1142 10x scRNA-seq data: Transcriptome mapping (using the mm10 genome assembly) and
1143 demultiplexing were performed using the 10X Genomics Cell Ranger software (version
1144 3.0.2). Several data-filtering steps were performed on the matrix of transcript counts
1145 (using R version 3.5.3) prior to further analysis. First, we filtered out all genes detected in
1146 fewer than ten single-cell libraries, and filtered out all libraries with less than 4,500
1147 detected genes. This threshold was selected based on the histogram of gene detection
1148 for all single-cell libraries as initially called by the Cell Ranger cell detection algorithm,
1149 which appeared to reflect two different distributions corresponding to low-complexity
1150 versus high-complexity libraries. The low-complexity distribution was right-skewed and
1151 had a mode of less than 1,000 detected genes, whereas the high-complexity distribution
1152 was left-skewed and had a mode of ~7,500 detected genes. 4,500 genes was roughly
1153 the boundary between the two distributions; i.e. the minima between the two modes, and
1154 also corresponded to a sharp inflection point in the Barcodes versus UMI counts plot in
1155 the web_summary.html file generated by Cell Ranger. While many of these low-
1156 complexity libraries may have been misidentified as cells by Cell Ranger (e.g. droplets
1157 containing transcripts from lysed cells, rather than intact cells) examination of genes
1158 enriched in lower-complexity libraries suggested that some of them reflected unhealthy
1159 cells (e.g. libraries with high mitochondrial gene expression) or contaminating non-
1160 neuronal cells (e.g. libraries enriched for glial marker genes). Notably, the number of
1161 cells with high-complexity libraries corresponded well with our estimated number of
1162 eGFP positive cells used as input to the 10X chip. We further excluded libraries with: (1)
1163 evidence of glial contamination, based on high-outlier expression of glial marker genes,
1164 including *Plp1*, *Olig1*, and *Aqp4*, (2) absence or low-outlier levels of *Pet1/Fev* transcripts,
1165 (3) greater than fifteen percent of detected genes corresponding with mitochondrial

1166 genes, (4) less than two percent of detected genes corresponding with ribosomal genes
1167 (these appeared to be single-nuclei libraries, rather than single-cell), (5) high-outlier UMI
1168 counts, and (6) high-outlier gene detection. 2,350 single-cell libraries and 17,231 genes
1169 passed the above filtering criteria.

1170 Next, we created a Seurat object using these filtered data (Seurat version 3.0.2). Data
1171 were log-normalized using the NormalizeData function (using the default scale factor of
1172 1e4), and we identified the top two thousand genes (or in some cases non-coding RNAs)
1173 with the most highly variable transcript expression across single cells using the
1174 FindVariableFeatures function (selection.method = “vst”, nfeatures=2000). We then
1175 scaled and centered the log-normalized data using the ScaleData function and carried
1176 out principal components analysis (PCA) on the scaled expression values of the two
1177 thousand most highly variable genes. This allowed us to reduce the dimensionality of the
1178 data onto a smaller set of composite variables representing the most salient gene
1179 expression differences across single neurons. The procedure for identifying meaningful
1180 *Pet1* neuron subtype clusters is thoroughly described in the Results section of the main
1181 text. Briefly, we systematically varied the number of principal components included and
1182 the resolution parameter in the functions FindNeighbors, FindClusters, and RunUMAP,
1183 Dendrograms were created using BuildClusterTree and PlotClusterTree, and cluster-
1184 enriched genes were identified using the FindAllMarkers function, with min.pct = 0.25
1185 and logfc.threshold = 0.25, using Wilcoxon Rank Sum tests. This function adjusts p-
1186 values for multiple comparisons using the Bonferroni correction. All genes found to be
1187 significantly enriched or “de-enriched” (i.e. expressed at a significantly lower level) in
1188 each cluster, as well as the top two thousand highest variance genes, can be found in
1189 the Supplemental Excel Spreadsheet.

1190 <u>Manual scRNA-seq data:</u> Transcript mapping to the mm10 genome assembly and
1191 feature counts were performed using STAR (version 2.5.4) (Dobin and Gingeras, 2016).
1192 Given the high purity of manual cell sorting and the high sensitivity of SMART-Seq v4
1193 cDNA amplification, no data filtering was required; i.e. single-cell libraries showed no
1194 evidence for off-target contamination and showed consistently high gene detection
1195 (~9,000 genes per single-cell). Counts data were analyzed using Seurat as described
1196 for 10X scRNA-seq data.

1197 scRNA-seq data availability: RNA-seq data (manual and 10X) are available through the
1198 Gene Expression Omnibus (GEO), accession number GSE144980.

1199 Transfer of 10X cell type labels: In order to explore the correspondence between the
1200 fourteen 10X scRNA-seq data-defined *Pet1* neuron subtypes and other scRNA-seq data,
1201 including our manual scRNA-seq data, and the Huang, et al. 2019 and Ren, et al. 2019
1202 datasets, we employed the strategy outlined in (Stuart et al., 2019). Specifically, we used
1203 the Seurat functions FindTransferAnchors and TransferData, using the 10X data as the
1204 "reference" and the other datasets as the "query" group.

1205 **Electrophysiology methods**

1206 *In vitro* brainstem slice preparations containing dorsal raphe serotonin neurons were
1207 obtained from 4-5 week old mice. After isofluorane anesthesia, mice were perfused
1208 transcardially with a solution of artificial CSF ($NaHCO_3$-aCSF) containing the following
1209 (in mM): 124 NaCl, 25 NaHCO3, 3 KCl, 2 CaCl2, 2 $MgCl_2$, 1.2, NaH2PO4 and 25 d-
1210 Glucose, equilibrated with 95% O2 and 5% CO2 adjusted to 310 ± 5 mOsm/L. The
1211 brainstem was dissected and mounted on the stage of a VT1200S vibratome while
1212 immersed in an ice slush solution aCSF containing the following (in mM): NMDG 93, HCl
1213 93, KCL 2.5, NaH_2P0_4 1.2, $NaHCO_3$ 30, HEPES 20, d-Glucose 25, Na-Ascorbate 5,
1214 Thiourea 2, Na-Pyruvate 3, $MgSO_4$ 10, $CaCl_2$ 0.5 equilibrated with 95% O2 and 5% CO2
1215 adjusted to 310 ± 5 mOsm/L. Coronal slices 200 µm thick containing the dorsal nucleus
1216 raphe were recovered for 1h at 35-6 C in HEPES-aCSF containing: NaCl 92, KCl 2.5,
1217 NaH_2P0_4 1.2, $NaHCO_3$ 30, HEPES 20, Glucose 25, Na-Ascorbate 5, Thiourea 2,
1218 NaPyruvate 3, $MgSO_4$ 10, $CaCl_2$ 0.5 equilibrated with 95% O2 and 5% CO2 adjusted to
1219 310 ± 5 mOsm/L and placed at room temperature for storage. Individual slices were
1220 transferred to the recording chamber and superfused with NaHCO3-aCSF at
1221 34ºC. Electrodes (5–7 MΩ) were pulled from borosilicate glass. Pipettes were filled with
1222 (in mM): 140 K-gluconate, HEPES 10, KCl 5, Na-ATP 2, $MgCl_2$ 2, EGTA 0.02, biocytin
1223 0.1% Na_2GTP 0.5, Na_2-phosphocreatine 4, pH 7.4 adjusted with KOH and adjusted to
1224 285 ± 5 mOsm/L with sucrose. Somatic whole-cell recordings were obtained with a
1225 Multiclamp 700B amplifier, signals were acquired and sampled at 100 kHz
1226 using Digidata 1440A digitizing board. Pipette capacitance was compensated ≈70% in
1227 current clamp (CC). Series resistance (*R*s) was typically 9–15 MΩ. Cells with *R*s > 15
1228 MΩ were discarded. A measured liquid junction potential of ≈10 mV was corrected

online. Cells were held at V_h= -80 mV unless otherwise indicated. To create action potential frequency-current curves, a protocol that applies a series of 750 ms current pulses ranging from -100 pA to 220 pA was created using Molecular Devices Clampex 10.7 software running on Windows 7.

Acknowledgments

The authors thank the Biopolymers Facility at HMS for assistance with next-generation sequencing; the Microscopy Resources on the North Quad (MicRoN) core at Harvard Medical School for microscope use; Steve Liberles for providing *Npy2r::IRES-cre* and *P2ry1::IRES-cre* driver lines; ChangHee Lee and Jin Akagi for advice with the On-chip Sort; Kathryn Commons and the Dymecki lab for discussions and thoughtful comments on this manuscript; J.J Mai for reagents and animal husbandry. Grants supporting this work include NARSAD Young Investigator Grant (BWO), NIDA Grant RO1DA034022 (BWO, OVA, SMD), T32 HL 007901 (NS), Howard Hughes Medical Institute Gilliam Fellowship (KAL), NIH F99-NS108515 (KAL), Harvard Brain Science Initiative Bipolar Disorder Seed Grant, supported by Kent and Liz Dauten (OVA), and the GVR Khodadad Fund for the Study of Genetic, Neurobiological, and Physiochemical Processes of EPS (OVA, SMD).

References

Abrams, J.K., Johnson, P.L., Hollis, J.H., and Lowry, C.A. (2004). Anatomic and functional topography of the dorsal raphe nucleus. Ann N Y Acad Sci 1018, 46-57.

Aghajanian, G.K., and Gallager, D.W. (1975). Raphe origin of serotonergic nerves terminating in the cerebral ventricles. Brain Res 88, 221-231.

Alfonso, J., Penkert, H., Duman, C., Zuccotti, A., and Monyer, H. (2015). Downregulation of Sphingosine 1-Phosphate Receptor 1 Promotes the Switch from Tangential to Radial Migration in the OB. J Neurosci 35, 13659-13672.

Alonso, A., Merchan, P., Sandoval, J.E., Sanchez-Arrones, L., Garcia-Cazorla, A., Artuch, R., Ferran, J.L., Martinez-de-la-Torre, M., and Puelles, L. (2013). Development of the serotonergic cells in murine raphe nuclei and their relations with rhombomeric domains. Brain Struct Funct 218, 1229-1277.

Amilhon, B., Lepicard, E., Renoir, T., Mongeau, R., Popa, D., Poirel, O., Miot, S., Gras, C., Gardier, A.M., Gallego, J.*, et al.* (2010). VGLUT3 (vesicular glutamate transporter type 3) contribution to the regulation of serotonergic transmission and anxiety. J Neurosci 30, 2198-2210.

1262 Andrade, R., and Haj-Dahmane, S. (2013). Serotonin neuron diversity in the dorsal
1263 raphe. ACS Chem Neurosci 4, 22-25.

1264 Asano, M., and Gruss, P. (1992). Pax-5 is expressed at the midbrain-hindbrain boundary
1265 during mouse development. Mech Dev 39, 29-39.

1266 Azmitia, E.C., and Segal, M. (1978). An autoradiographic analysis of the differential
1267 ascending projections of the dorsal and median raphe nuclei in the rat. J Comp Neurol
1268 179, 641-667.

1269 Baker, K.G., Halliday, G.M., Halasz, P., Hornung, J.P., Geffen, L.B., Cotton, R.G., and
1270 Tork, I. (1991a). Cytoarchitecture of serotonin-synthesizing neurons in the pontine
1271 tegmentum of the human brain. Synapse 7, 301-320.

1272 Baker, K.G., Halliday, G.M., Hornung, J.P., Geffen, L.B., Cotton, R.G., and Tork, I.
1273 (1991b). Distribution, morphology and number of monoamine-synthesizing and
1274 substance P-containing neurons in the human dorsal raphe nucleus. Neuroscience 42,
1275 757-775.

1276 Baker, K.G., Halliday, G.M., and Tork, I. (1990). Cytoarchitecture of the human dorsal
1277 raphe nucleus. J Comp Neurol 301, 147-161.

1278 Bakken, T.E., Hodge, R.D., Miller, J.A., Yao, Z., Nguyen, T.N., Aevermann, B., Barkan,
1279 E., Bertagnolli, D., Casper, T., Dee, N.*, et al.* (2018). Single-nucleus and single-cell
1280 transcriptomes compared in matched cortical cell types. PLoS One 13, e0209648.

1281 Banasr, M., Hery, M., Printemps, R., and Daszuta, A. (2004). Serotonin-induced
1282 increases in adult cell proliferation and neurogenesis are mediated through different and
1283 common 5-HT receptor subtypes in the dentate gyrus and the subventricular zone.
1284 Neuropsychopharmacology 29, 450-460.

1285 Bang, S.J., and Commons, K.G. (2012). Forebrain GABAergic projections from the
1286 dorsal raphe nucleus identified by using GAD67-GFP knock-in mice. J Comp Neurol
1287 520, 4157-4167.

1288 Bang, S.J., Jensen, P., Dymecki, S.M., and Commons, K.G. (2012). Projections and
1289 interconnections of genetically defined serotonin neurons in mice. Eur J Neurosci 35, 85-
1290 96.

1291 Barrett, K.T., Dosumu-Johnson, R.T., Daubenspeck, J.A., Brust, R.D., Kreouzis, V., Kim,
1292 J.C., Li, A., Dymecki, S.M., and Nattie, E.E. (2016). Partial Raphe Dysfunction in
1293 Neurotransmission Is Sufficient to Increase Mortality after Anoxic Exposures in Mice at a
1294 Critical Period in Postnatal Development. J Neurosci 36, 3943-3953.

1295 Beaudet, A., and Descarries, L. (1976). Quantitative data on serotonin nerve terminals in
1296 adult rat neocortex. Brain Res 111, 301-309.

1297 Bellido, I., Hansson, A.C., Gomez-Luque, A.J., Andbjer, B., Agnati, L.F., and Fuxe, K.
1298 (2004). Corticosterone strongly increases the affinity of dorsal raphe 5-HT1A receptors.
1299 Neuroreport 15, 1457-1459.

1300 Brezun, J.M., and Daszuta, A. (1999). Depletion in serotonin decreases neurogenesis in
1301 the dentate gyrus and the subventricular zone of adult rats. Neuroscience 89, 999-1002.

1302 Bruchas, M.R., Land, B.B., and Chavkin, C. (2010). The dynorphin/kappa opioid system
1303 as a modulator of stress-induced and pro-addictive behaviors. Brain Res 1314, 44-55.

1304 Brust, R.D., Corcoran, A.E., Richerson, G.B., Nattie, E., and Dymecki, S.M. (2014).
1305 Functional and developmental identification of a molecular subtype of brain serotonergic
1306 neuron specialized to regulate breathing dynamics. Cell Rep 9, 2152-2165.

1307 Butler, A., Hoffman, P., Smibert, P., Papalexi, E., and Satija, R. (2018). Integrating
1308 single-cell transcriptomic data across different conditions, technologies, and species. Nat
1309 Biotechnol 36, 411-420.

1310 Calizo, L.H., Akanwa, A., Ma, X., Pan, Y.Z., Lemos, J.C., Craige, C., Heemstra, L.A.,
1311 and Beck, S.G. (2011). Raphe serotonin neurons are not homogenous:
1312 electrophysiological, morphological and neurochemical evidence. Neuropharmacology
1313 61, 524-543.

1314 Campbell, J.N., Macosko, E.Z., Fenselau, H., Pers, T.H., Lyubetskaya, A., Tenen, D.,
1315 Goldman, M., Verstegen, A.M., Resch, J.M., McCarroll, S.A*., et al.* (2017). A molecular
1316 census of arcuate hypothalamus and median eminence cell types. Nat Neurosci 20, 484-
1317 496.

1318 Celada, P., Puig, M.V., Casanovas, J.M., Guillazo, G., and Artigas, F. (2001). Control of
1319 dorsal raphe serotonergic neurons by the medial prefrontal cortex: Involvement of
1320 serotonin-1A, GABA(A), and glutamate receptors. J Neurosci 21, 9917-9929.

1321 Challis, C., Boulden, J., Veerakumar, A., Espallergues, J., Vassoler, F.M., Pierce, R.C.,
1322 Beck, S.G., and Berton, O. (2013). Raphe GABAergic neurons mediate the acquisition of
1323 avoidance after social defeat. J Neurosci 33, 13978-13988, 13988a.

1324 Chang, R.B., Strochlic, D.E., Williams, E.K., Umans, B.D., and Liberles, S.D. (2015).
1325 Vagal Sensory Neuron Subtypes that Differentially Control Breathing. Cell 161, 622-633.

1326 Chavkin, C., James, I.F., and Goldstein, A. (1982). Dynorphin is a specific endogenous
1327 ligand of the kappa opioid receptor. Science 215, 413-415.

1328 Chen, C.H., Battaglioli, G., Martin, D.L., Hobart, S.A., and Colon, W. (2003). Distinctive
1329 interactions in the holoenzyme formation for two isoforms of glutamate decarboxylase.
1330 Biochim Biophys Acta 1645, 63-71.

1331 Chen, C.P., Eastwood, S.L., Hope, T., McDonald, B., Francis, P.T., and Esiri, M.M.
1332 (2000). Immunocytochemical study of the dorsal and median raphe nuclei in patients

1333 with Alzheimer's disease prospectively assessed for behavioural changes. Neuropathol
1334 Appl Neurobiol 26, 347-355.

1335 Commons, K.G. (2009). Locally collateralizing glutamate neurons in the dorsal raphe
1336 nucleus responsive to substance P contain vesicular glutamate transporter 3 (VGLUT3).
1337 J Chem Neuroanat 38, 273-281.

1338 Commons, K.G. (2015). Two major network domains in the dorsal raphe nucleus. J
1339 Comp Neurol 523, 1488-1504.

1340 Commons, K.G. (2016). Ascending serotonin neuron diversity under two umbrellas.
1341 Brain Struct Funct 221, 3347-3360.

1342 Condomitti, G., and de Wit, J. (2018). Heparan Sulfate Proteoglycans as Emerging
1343 Players in Synaptic Specificity. Front Mol Neurosci 11, 14.

1344 Crawford, L.K., Craige, C.P., and Beck, S.G. (2010). Increased intrinsic excitability of
1345 lateral wing serotonin neurons of the dorsal raphe: a mechanism for selective activation
1346 in stress circuits. J Neurophysiol 103, 2652-2663.

1347 Dahlstroem, A., and Fuxe, K. (1964). Evidence for the Existence of Monoamine-
1348 Containing Neurons in the Central Nervous System. I. Demonstration of Monoamines in
1349 the Cell Bodies of Brain Stem Neurons. Acta Physiol Scand Suppl, SUPPL 232:231-255.

1350 Dengler-Crish, C.M., Smith, M.A., and Wilson, G.N. (2017). Early Evidence of Low Bone
1351 Density and Decreased Serotonergic Synthesis in the Dorsal Raphe of a Tauopathy
1352 Model of Alzheimer's Disease. J Alzheimers Dis 55, 1605-1619.

1353 Di Donato, V., De Santis, F., Albadri, S., Auer, T.O., Duroure, K., Charpentier, M.,
1354 Concordet, J.P., Gebhardt, C., and Del Bene, F. (2018). An Attractive Reelin Gradient
1355 Establishes Synaptic Lamination in the Vertebrate Visual System. Neuron 97, 1049-1062
1356 e1046.

1357 Dobin, A., and Gingeras, T.R. (2016). Optimizing RNA-Seq Mapping with STAR.
1358 Methods Mol Biol 1415, 245-262.

1359 Dymecki, S.M., Ray, R.S., and Kim, J.C. (2010). Mapping cell fate and function using
1360 recombinase-based intersectional strategies. Methods Enzymol 477, 183-213.

1361 El Mestikawy, S., Wallen-Mackenzie, A., Fortin, G.M., Descarries, L., and Trudeau, L.E.
1362 (2011). From glutamate co-release to vesicular synergy: vesicular glutamate
1363 transporters. Nat Rev Neurosci 12, 204-216.

1364 Ellegood, J., Nakai, N., Nakatani, J., Henkelman, M., Takumi, T., and Lerch, J. (2015).
1365 Neuroanatomical Phenotypes Are Consistent With Autism-Like Behavioral Phenotypes
1366 in the 15q11-13 Duplication Mouse Model. Autism Res 8, 545-555.

1367 Erbel-Sieler, C., Dudley, C., Zhou, Y., Wu, X., Estill, S.J., Han, T., Diaz-Arrastia, R.,
1368 Brunskill, E.W., Potter, S.S., and McKnight, S.L. (2004). Behavioral and regulatory

1369 abnormalities in mice deficient in the NPAS1 and NPAS3 transcription factors. Proc Natl
1370 Acad Sci U S A 101, 13648-13653.

1371 Erickson, J.D., Eiden, L.E., and Hoffman, B.J. (1992). Expression cloning of a reserpine-
1372 sensitive vesicular monoamine transporter. Proc Natl Acad Sci U S A 89, 10993-10997.

1373 Erlander, M.G., Tillakaratne, N.J., Feldblum, S., Patel, N., and Tobin, A.J. (1991). Two
1374 genes encode distinct glutamate decarboxylases. Neuron 7, 91-100.

1375 Evrard, A., Barden, N., Hamon, M., and Adrien, J. (2006). Glucocorticoid receptor-
1376 dependent desensitization of 5-HT1A autoreceptors by sleep deprivation: studies in GR-i
1377 transgenic mice. Sleep 29, 31-36.

1378 Fernandez, S.P., Cauli, B., Cabezas, C., Muzerelle, A., Poncer, J.C., and Gaspar, P.
1379 (2016). Multiscale single-cell analysis reveals unique phenotypes of raphe 5-HT neurons
1380 projecting to the forebrain. Brain Struct Funct 221, 4007-4025.

1381 Fox, S.R., and Deneris, E.S. (2012). Engrailed is required in maturing serotonin neurons
1382 to regulate the cytoarchitecture and survival of the dorsal raphe nucleus. J Neurosci 32,
1383 7832-7842.

1384 Fremeau, R.T., Jr., Burman, J., Qureshi, T., Tran, C.H., Proctor, J., Johnson, J., Zhang,
1385 H., Sulzer, D., Copenhagen, D.R., Storm-Mathisen, J.*, et al.* (2002). The identification of
1386 vesicular glutamate transporter 3 suggests novel modes of signaling by glutamate. Proc
1387 Natl Acad Sci U S A 99, 14488-14493.

1388 Fu, W., Le Maitre, E., Fabre, V., Bernard, J.F., David Xu, Z.Q., and Hokfelt, T. (2010).
1389 Chemical neuroanatomy of the dorsal raphe nucleus and adjacent structures of the
1390 mouse brain. J Comp Neurol 518, 3464-3494.

1391 Funahashi, J., Okafuji, T., Ohuchi, H., Noji, S., Tanaka, H., and Nakamura, H. (1999).
1392 Role of Pax-5 in the regulation of a mid-hindbrain organizer's activity. Dev Growth Differ
1393 41, 59-72.

1394 Fyodorov, D., Nelson, T., and Deneris, E. (1998). Pet-1, a novel ETS domain factor that
1395 can activate neuronal nAchR gene transcription. J Neurobiol 34, 151-163.

1396 Gagnon, D., and Parent, M. (2014). Distribution of VGLUT3 in highly collateralized axons
1397 from the rat dorsal raphe nucleus as revealed by single-neuron reconstructions. PLoS
1398 One 9, e87709.

1399 Gaspar, P., and Lillesaar, C. (2012). Probing the diversity of serotonin neurons. Philos
1400 Trans R Soc Lond B Biol Sci 367, 2382-2394.

1401 Goncalves, L., Nogueira, M.I., Shammah-Lagnado, S.J., and Metzger, M. (2009).
1402 Prefrontal afferents to the dorsal raphe nucleus in the rat. Brain Res Bull 78, 240-247.

1403 Gong, S., Doughty, M., Harbaugh, C.R., Cummins, A., Hatten, M.E., Heintz, N., and
1404 Gerfen, C.R. (2007). Targeting Cre recombinase to specific neuron populations with
1405 bacterial artificial chromosome constructs. J Neurosci 27, 9817-9823.

1406 Gras, C., Herzog, E., Bellenchi, G.C., Bernard, V., Ravassard, P., Pohl, M., Gasnier, B.,
1407 Giros, B., and El Mestikawy, S. (2002). A third vesicular glutamate transporter expressed
1408 by cholinergic and serotoninergic neurons. J Neurosci 22, 5442-5451.

1409 Guo, Y.P., and Commons, K.G. (2017). Serotonin neuron abnormalities in the BTBR
1410 mouse model of autism. Autism Res 10, 66-77.

1411 Hale, M.W., and Lowry, C.A. (2011). Functional topography of midbrain and pontine
1412 serotonergic systems: implications for synaptic regulation of serotonergic circuits.
1413 Psychopharmacology (Berl) 213, 243-264.

1414 Harburg, G.C., Hall, F.S., Harrist, A.V., Sora, I., Uhl, G.R., and Eisch, A.J. (2007).
1415 Knockout of the mu opioid receptor enhances the survival of adult-generated
1416 hippocampal granule cell neurons. Neuroscience 144, 77-87.

1417 Hempel, C.M., Sugino, K., and Nelson, S.B. (2007). A manual method for the purification
1418 of fluorescently labeled neurons from the mammalian brain. Nat Protoc 2, 2924-2929.

1419 Hendricks, T., Francis, N., Fyodorov, D., and Deneris, E.S. (1999). The ETS domain
1420 factor Pet-1 is an early and precise marker of central serotonin neurons and interacts
1421 with a conserved element in serotonergic genes. J Neurosci 19, 10348-10356.

1422 Hendricks, T.J., Fyodorov, D.V., Wegman, L.J., Lelutiu, N.B., Pehek, E.A., Yamamoto,
1423 B., Silver, J., Weeber, E.J., Sweatt, J.D., and Deneris, E.S. (2003). Pet-1 ETS gene
1424 plays a critical role in 5-HT neuron development and is required for normal anxiety-like
1425 and aggressive behavior. Neuron 37, 233-247.

1426 Hennessy, M.L., Corcoran, A.E., Brust, R.D., Chang, Y., Nattie, E.E., and Dymecki, S.M.
1427 (2017). Activity of Tachykinin1-Expressing Pet1 Raphe Neurons Modulates the
1428 Respiratory Chemoreflex. J Neurosci 37, 1807-1819.

1429 Herzog, E., Gilchrist, J., Gras, C., Muzerelle, A., Ravassard, P., Giros, B., Gaspar, P.,
1430 and El Mestikawy, S. (2004). Localization of VGLUT3, the vesicular glutamate
1431 transporter type 3, in the rat brain. Neuroscience 123, 983-1002.

1432 Hioki, H., Fujiyama, F., Nakamura, K., Wu, S.X., Matsuda, W., and Kaneko, T. (2004).
1433 Chemically specific circuit composed of vesicular glutamate transporter 3- and
1434 preprotachykinin B-producing interneurons in the rat neocortex. Cereb Cortex 14, 1266-
1435 1275.

1436 Hioki, H., Nakamura, H., Ma, Y.F., Konno, M., Hayakawa, T., Nakamura, K.C., Fujiyama,
1437 F., and Kaneko, T. (2010). Vesicular glutamate transporter 3-expressing
1438 nonserotonergic projection neurons constitute a subregion in the rat midbrain raphe
1439 nuclei. J Comp Neurol 518, 668-686.

1440 Hitoshi, S., Maruta, N., Higashi, M., Kumar, A., Kato, N., and Ikenaka, K. (2007).
1441 Antidepressant drugs reverse the loss of adult neural stem cells following chronic stress.
1442 J Neurosci Res 85, 3574-3585.

1443 Hodge, R.D., Bakken, T.E., Miller, J.A., Smith, K.A., Barkan, E.R., Graybuck, L.T.,
1444 Close, J.L., Long, B., Johansen, N., Penn, O.*, et al.* (2019). Conserved cell types with
1445 divergent features in human versus mouse cortex. Nature 573, 61-68.

1446 Hoffman, B.J., Mezey, E., and Brownstein, M.J. (1991). Cloning of a serotonin
1447 transporter affected by antidepressants. Science 254, 579-580.

1448 Huang, K.W., Ochandarena, N.E., Philson, A.C., Hyun, M., Birnbaum, J.E., Cicconet, M.,
1449 and Sabatini, B.L. (2019). Molecular and anatomical organization of the dorsal raphe
1450 nucleus. Elife 8.

1451 Ishimura, K., Takeuchi, Y., Fujiwara, K., Tominaga, M., Yoshioka, H., and Sawada, T.
1452 (1988). Quantitative analysis of the distribution of serotonin-immunoreactive cell bodies
1453 in the mouse brain. Neurosci Lett 91, 265-270.

1454 Iyer, A., Kmiecik, T.E., Park, M., Daar, I., Blair, D., Dunn, K.J., Sutrave, P., Ihle, J.N.,
1455 Bodescot, M., and Vande Woude, G.F. (1990). Structure, tissue-specific expression, and
1456 transforming activity of the mouse met protooncogene. Cell Growth Differ 1, 87-95.

1457 Jacobs, B.L., and Azmitia, E.C. (1992). Structure and function of the brain serotonin
1458 system. Physiol Rev 72, 165-229.

1459 Jensen, P., Farago, A.F., Awatramani, R.B., Scott, M.M., Deneris, E.S., and Dymecki,
1460 S.M. (2008). Redefining the serotonergic system by genetic lineage. Nat Neurosci 11,
1461 417-419.

1462 Ji, X., Wang, H., Zhu, M., He, Y., Zhang, H., Chen, X., Gao, W., Fu, Y., and Alzheimer's
1463 Disease Neuroimaging, I. (2020). Brainstem atrophy in the early stage of Alzheimer's
1464 disease: a voxel-based morphometry study. Brain Imaging Behav.

1465 Johnson, M.D. (1994). Synaptic glutamate release by postnatal rat serotonergic neurons
1466 in microculture. Neuron 12, 433-442.

1467 Joyner, A.L., Kornberg, T., Coleman, K.G., Cox, D.R., and Martin, G.R. (1985).
1468 Expression during embryogenesis of a mouse gene with sequence homology to the
1469 Drosophila engrailed gene. Cell 43, 29-37.

1470 Joyner, A.L., and Martin, G.R. (1987). En-1 and En-2, two mouse genes with sequence
1471 homology to the Drosophila engrailed gene: expression during embryogenesis. Genes
1472 Dev 1, 29-38.

1473 Judge, S.J., Ingram, C.D., and Gartside, S.E. (2004). Moderate differences in circulating
1474 corticosterone alter receptor-mediated regulation of 5-hydroxytryptamine neuronal
1475 activity. J Psychopharmacol 18, 475-483.

1476 Kapoor, V., Provost, A.C., Agarwal, P., and Murthy, V.N. (2016). Activation of raphe
1477 nuclei triggers rapid and distinct effects on parallel olfactory bulb output channels. Nat
1478 Neurosci 19, 271-282.

1479 Kast, R.J., Wu, H.H., Williams, P., Gaspar, P., and Levitt, P. (2017). Specific
1480 Connectivity and Unique Molecular Identity of MET Receptor Tyrosine Kinase
1481 Expressing Serotonergic Neurons in the Caudal Dorsal Raphe Nuclei. ACS Chem
1482 Neurosci 8, 1053-1064.

1483 Kim, J.C., Cook, M.N., Carey, M.R., Shen, C., Regehr, W.G., and Dymecki, S.M. (2009).
1484 Linking genetically defined neurons to behavior through a broadly applicable silencing
1485 allele. Neuron 63, 305-315.

1486 Kimmel, R.A., Turnbull, D.H., Blanquet, V., Wurst, W., Loomis, C.A., and Joyner, A.L.
1487 (2000). Two lineage boundaries coordinate vertebrate apical ectodermal ridge formation.
1488 Genes Dev 14, 1377-1389.

1489 Kirby, L.G., Pernar, L., Valentino, R.J., and Beck, S.G. (2003). Distinguishing
1490 characteristics of serotonin and non-serotonin-containing cells in the dorsal raphe
1491 nucleus: electrophysiological and immunohistochemical studies. Neuroscience 116, 669-
1492 683.

1493 Kosofsky, B.E., and Molliver, M.E. (1987). The serotoninergic innervation of cerebral
1494 cortex: different classes of axon terminals arise from dorsal and median raphe nuclei.
1495 Synapse 1, 153-168.

1496 Krueger, K.C., and Deneris, E.S. (2008). Serotonergic transcription of human FEV
1497 reveals direct GATA factor interactions and fate of Pet-1-deficient serotonin neuron
1498 precursors. J Neurosci 28, 12748-12758.

1499 Laaris, N., Haj-Dahmane, S., Hamon, M., and Lanfumey, L. (1995). Glucocorticoid
1500 receptor-mediated inhibition by corticosterone of 5-HT1A autoreceptor functioning in the
1501 rat dorsal raphe nucleus. Neuropharmacology 34, 1201-1210.

1502 Land, B.B., Bruchas, M.R., Lemos, J.C., Xu, M., Melief, E.J., and Chavkin, C. (2008).
1503 The dysphoric component of stress is encoded by activation of the dynorphin kappa-
1504 opioid system. J Neurosci 28, 407-414.

1505 Land, B.B., Bruchas, M.R., Schattauer, S., Giardino, W.J., Aita, M., Messinger, D.,
1506 Hnasko, T.S., Palmiter, R.D., and Chavkin, C. (2009). Activation of the kappa opioid
1507 receptor in the dorsal raphe nucleus mediates the aversive effects of stress and
1508 reinstates drug seeking. Proc Natl Acad Sci U S A 106, 19168-19173.

1509 Lazaro-Pena, M.I., Diaz-Balzac, C.A., Bulow, H.E., and Emmons, S.W. (2018).
1510 Synaptogenesis Is Modulated by Heparan Sulfate in Caenorhabditis elegans. Genetics
1511 209, 195-208.

1512 Lesch, K.P., Wolozin, B.L., Estler, H.C., Murphy, D.L., and Riederer, P. (1993). Isolation
1513 of a cDNA encoding the human brain serotonin transporter. J Neural Transm Gen Sect
1514 91, 67-72.

1515 Levine, E.S., and Jacobs, B.L. (1992). Neurochemical afferents controlling the activity of
1516 serotonergic neurons in the dorsal raphe nucleus: microiontophoretic studies in the
1517 awake cat. J Neurosci 12, 4037-4044.

1518 Lidov, H.G., Grzanna, R., and Molliver, M.E. (1980). The serotonin innervation of the
1519 cerebral cortex in the rat--an immunohistochemical analysis. Neuroscience 5, 207-227.

1520 Lidov, H.G., and Molliver, M.E. (1982). Immunohistochemical study of the development
1521 of serotonergic neurons in the rat CNS. Brain Res Bull 9, 559-604.

1522 Lin, J.H., Takano, T., Arcuino, G., Wang, X., Hu, F., Darzynkiewicz, Z., Nunes, M.,
1523 Goldman, S.A., and Nedergaard, M. (2007). Purinergic signaling regulates neural
1524 progenitor cell expansion and neurogenesis. Dev Biol 302, 356-366.

1525 Liu, C., Maejima, T., Wyler, S.C., Casadesus, G., Herlitze, S., and Deneris, E.S. (2010).
1526 Pet-1 is required across different stages of life to regulate serotonergic function. Nat
1527 Neurosci 13, 1190-1198.

1528 Liu, Z., Zhou, J., Li, Y., Hu, F., Lu, Y., Ma, M., Feng, Q., Zhang, J.E., Wang, D., Zeng, J.,
1529 *et al.* (2014). Dorsal raphe neurons signal reward through 5-HT and glutamate. Neuron
1530 81, 1360-1374.

1531 Lorez, H.P., and Richards, J.G. (1982). Supra-ependymal serotoninergic nerves in
1532 mammalian brain: morphological, pharmacological and functional studies. Brain Res Bull
1533 9, 727-741.

1534 Lovatt, D., Ruble, B.K., Lee, J., Dueck, H., Kim, T.K., Fisher, S., Francis, C., Spaethling,
1535 J.M., Wolf, J.A., Grady, M.S., *et al.* (2014). Transcriptome in vivo analysis (TIVA) of
1536 spatially defined single cells in live tissue. Nat Methods 11, 190-196.

1537 Love, C.E., and Prince, V.E. (2012). Expression and retinoic acid regulation of the
1538 zebrafish nr2f orphan nuclear receptor genes. Dev Dyn 241, 1603-1615.

1539 Luo, J., Feng, Q., Wei, L., and Luo, M. (2017). Optogenetic activation of dorsal raphe
1540 neurons rescues the autistic-like social deficits in Shank3 knockout mice. Cell Res 27,
1541 950-953.

1542 Macosko, E.Z., Basu, A., Satija, R., Nemesh, J., Shekhar, K., Goldman, M., Tirosh, I.,
1543 Bialas, A.R., Kamitaki, N., Martersteck, E.M., *et al.* (2015). Highly Parallel Genome-wide
1544 Expression Profiling of Individual Cells Using Nanoliter Droplets. Cell 161, 1202-1214.

1545 Maddaloni, G., Bertero, A., Pratelli, M., Barsotti, N., Boonstra, A., Giorgi, A., Migliarini,
1546 S., and Pasqualetti, M. (2017). Development of Serotonergic Fibers in the Post-Natal
1547 Mouse Brain. Front Cell Neurosci 11, 202.

1548 Madisen, L., Garner, A.R., Shimaoka, D., Chuong, A.S., Klapoetke, N.C., Li, L., van der
1549 Bourg, A., Niino, Y., Egolf, L., Monetti, C., *et al.* (2015). Transgenic mice for
1550 intersectional targeting of neural sensors and effectors with high specificity and
1551 performance. Neuron 85, 942-958.

1552 Makrides, N., Panayiotou, E., Fanis, P., Karaiskos, C., Lapathitis, G., and Malas, S.
1553 (2018). Sequential Role of SOXB2 Factors in GABAergic Neuron Specification of the
1554 Dorsal Midbrain. Front Mol Neurosci 11, 152.

1555 McDevitt, R.A., Tiran-Cappello, A., Shen, H., Balderas, I., Britt, J.P., Marino, R.A.,
1556 Chung, S.L., Richie, C.T., Harvey, B.K., and Bonci, A. (2014). Serotonergic versus
1557 nonserotonergic dorsal raphe projection neurons: differential participation in reward
1558 circuitry. Cell Rep 8, 1857-1869.

1559 Michaelson, J.J., Shin, M.K., Koh, J.Y., Brueggeman, L., Zhang, A., Katzman, A.,
1560 McDaniel, L., Fang, M., Pufall, M., and Pieper, A.A. (2017). Neuronal PAS Domain
1561 Proteins 1 and 3 Are Master Regulators of Neuropsychiatric Risk Genes. Biol Psychiatry
1562 82, 213-223.

1563 Michelsen, K.A., Prickaerts, J., and Steinbusch, H.W. (2008). The dorsal raphe nucleus
1564 and serotonin: implications for neuroplasticity linked to major depression and Alzheimer's
1565 disease. Prog Brain Res 172, 233-264.

1566 Michelsen, K.A., Schmitz, C., and Steinbusch, H.W. (2007). The dorsal raphe nucleus--
1567 from silver stainings to a role in depression. Brain Res Rev 55, 329-342.

1568 Mikkelsen, J.D., Hay-Schmidt, A., and Larsen, P.J. (1997). Central innervation of the rat
1569 ependyma and subcommissural organ with special reference to ascending
1570 serotoninergic projections from the raphe nuclei. J Comp Neurol 384, 556-568.

1571 Minge, D., Senkov, O., Kaushik, R., Herde, M.K., Tikhobrazova, O., Wulff, A.B., Mironov,
1572 A., van Kuppevelt, T.H., Oosterhof, A., Kochlamazashvili, G.*, et al.* (2017). Heparan
1573 Sulfates Support Pyramidal Cell Excitability, Synaptic Plasticity, and Context
1574 Discrimination. Cereb Cortex 27, 903-918.

1575 Mirzadeh, Z., Doetsch, F., Sawamoto, K., Wichterle, H., and Alvarez-Buylla, A. (2010).
1576 The subventricular zone en-face: wholemount staining and ependymal flow. J Vis Exp.

1577 Miyazaki, K., Narita, N., and Narita, M. (2005). Maternal administration of thalidomide or
1578 valproic acid causes abnormal serotonergic neurons in the offspring: implication for
1579 pathogenesis of autism. Int J Dev Neurosci 23, 287-297.

1580 Molliver, M.E. (1987). Serotonergic neuronal systems: what their anatomic organization
1581 tells us about function. J Clin Psychopharmacol 7, 3S-23S.

1582 Mosko, S.S., Haubrich, D., and Jacobs, B.L. (1977). Serotonergic afferents to the dorsal
1583 raphe nucleus: evdience from HRP and synaptosomal uptake studies. Brain Res 119,
1584 269-290.

1585 Munster-Wandowski, A., Zander, J.F., Richter, K., and Ahnert-Hilger, G. (2016). Co-
1586 existence of Functionally Different Vesicular Neurotransmitter Transporters. Front
1587 Synaptic Neurosci 8, 4.

1588 Muzerelle, A., Scotto-Lomassese, S., Bernard, J.F., Soiza-Reilly, M., and Gaspar, P.
1589 (2016). Conditional anterograde tracing reveals distinct targeting of individual serotonin
1590 cell groups (B5-B9) to the forebrain and brainstem. Brain Struct Funct 221, 535-561.

1591 Negoias, S., Croy, I., Gerber, J., Puschmann, S., Petrowski, K., Joraschky, P., and
1592 Hummel, T. (2010). Reduced olfactory bulb volume and olfactory sensitivity in patients
1593 with acute major depression. Neuroscience 169, 415-421.

1594 Niederkofler, V., Asher, T.E., Okaty, B.W., Rood, B.D., Narayan, A., Hwa, L.S., Beck,
1595 S.G., Miczek, K.A., and Dymecki, S.M. (2016). Identification of Serotonergic Neuronal
1596 Modules that Affect Aggressive Behavior. Cell Rep 17, 1934-1949.

1597 Nyberg, J., Anderson, M.F., Meister, B., Alborn, A.M., Strom, A.K., Brederlau, A.,
1598 Illerskog, A.C., Nilsson, O., Kieffer, T.J., Hietala, M.A*., et al.* (2005). Glucose-dependent
1599 insulinotropic polypeptide is expressed in adult hippocampus and induces progenitor cell
1600 proliferation. J Neurosci 25, 1816-1825.

1601 O'Hearn, E., and Molliver, M.E. (1984). Organization of raphe-cortical projections in rat:
1602 a quantitative retrograde study. Brain Res Bull 13, 709-726.

1603 Ogawa, S.K., Cohen, J.Y., Hwang, D., Uchida, N., and Watabe-Uchida, M. (2014).
1604 Organization of monosynaptic inputs to the serotonin and dopamine neuromodulatory
1605 systems. Cell Rep 8, 1105-1118.

1606 Okaty, B.W., Commons, K.G., and Dymecki, S.M. (2019). Embracing diversity in the 5-
1607 HT neuronal system. Nat Rev Neurosci.

1608 Okaty, B.W., Freret, M.E., Rood, B.D., Brust, R.D., Hennessy, M.L., deBairos, D., Kim,
1609 J.C., Cook, M.N., and Dymecki, S.M. (2015). Multi-Scale Molecular Deconstruction of
1610 the Serotonin Neuron System. Neuron 88, 774-791.

1611 Pelosi, B., Migliarini, S., Pacini, G., Pratelli, M., and Pasqualetti, M. (2014). Generation
1612 of Pet1210-Cre transgenic mouse line reveals non-serotonergic expression domains of
1613 Pet1 both in CNS and periphery. PLoS One 9, e104318.

1614 Peyron, C., Petit, J.M., Rampon, C., Jouvet, M., and Luppi, P.H. (1998). Forebrain
1615 afferents to the rat dorsal raphe nucleus demonstrated by retrograde and anterograde
1616 tracing methods. Neuroscience 82, 443-468.

1617 Peyron, C., Rampon, C., Petit, J.M., and Luppi, P.H. (2018). Sub-regions of the dorsal
1618 raphe nucleus receive different inputs from the brainstem. Sleep Med 49, 53-63.

1619 Pillai, A., Mansouri, A., Behringer, R., Westphal, H., and Goulding, M. (2007). Lhx1 and
1620 Lhx5 maintain the inhibitory-neurotransmitter status of interneurons in the dorsal spinal
1621 cord. Development 134, 357-366.

1622 Pollak Dorocic, I., Furth, D., Xuan, Y., Johansson, Y., Pozzi, L., Silberberg, G., Carlen,
1623 M., and Meletis, K. (2014). A whole-brain atlas of inputs to serotonergic neurons of the
1624 dorsal and median raphe nuclei. Neuron 83, 663-678.

1625 Poulin, J.F., Tasic, B., Hjerling-Leffler, J., Trimarchi, J.M., and Awatramani, R. (2016).
1626 Disentangling neural cell diversity using single-cell transcriptomics. Nat Neurosci 19,
1627 1131-1141.

1628 Prakash, N., Stark, C.J., Keisler, M.N., Luo, L., Der-Avakian, A., and Dulcis, D. (2019).
1629 Serotonergic plasticity in the dorsal raphe nucleus characterizes susceptibility and
1630 resilience to anhedonia. J Neurosci.

1631 Prouty, E.W., Chandler, D.J., and Waterhouse, B.D. (2017). Neurochemical differences
1632 betweentarget-specific populations of rat dorsal raphe projection neurons. Brain Res.

1633 Ray, R.S., Corcoran, A.E., Brust, R.D., Kim, J.C., Richerson, G.B., Nattie, E., and
1634 Dymecki, S.M. (2011). Impaired respiratory and body temperature control upon acute
1635 serotonergic neuron inhibition. Science 333, 637-642.

1636 Ren, J., Friedmann, D., Xiong, J., Liu, C.D., Ferguson, B.R., Weerakkody, T., DeLoach,
1637 K.E., Ran, C., Pun, A., Sun, Y.*, et al.* (2018). Anatomically Defined and Functionally
1638 Distinct Dorsal Raphe Serotonin Sub-systems. Cell 175, 472-487 e420.

1639 Ren, J., Isakova, A., Friedmann, D., Zeng, J., Grutzner, S.M., Pun, A., Zhao, G.Q.,
1640 Kolluru, S.S., Wang, R., Lin, R.*, et al.* (2019). Single-cell transcriptomes and whole-brain
1641 projections of serotonin neurons in the mouse dorsal and median raphe nuclei. Elife 8.

1642 Rood, B.D., Calizo, L.H., Piel, D., Spangler, Z.P., Campbell, K., and Beck, S.G. (2014).
1643 Dorsal raphe serotonin neurons in mice: immature hyperexcitability transitions to adult
1644 state during first three postnatal weeks suggesting sensitive period for environmental
1645 perturbation. J Neurosci 34, 4809-4821.

1646 Rosenberg, A.B., Roco, C.M., Muscat, R.A., Kuchina, A., Sample, P., Yao, Z., Graybuck,
1647 L.T., Peeler, D.J., Mukherjee, S., Chen, W.*, et al.* (2018). Single-cell profiling of the
1648 developing mouse brain and spinal cord with split-pool barcoding. Science 360, 176-182.

1649 Saunders, A., Macosko, E.Z., Wysoker, A., Goldman, M., Krienen, F.M., de Rivera, H.,
1650 Bien, E., Baum, M., Bortolin, L., Wang, S.*, et al.* (2018). Molecular Diversity and
1651 Specializations among the Cells of the Adult Mouse Brain. Cell 174, 1015-1030 e1016.

1652 Sciolino, N.R., Plummer, N.W., Chen, Y.W., Alexander, G.M., Robertson, S.D., Dudek,
1653 S.M., McElligott, Z.A., and Jensen, P. (2016). Recombinase-Dependent Mouse Lines for
1654 Chemogenetic Activation of Genetically Defined Cell Types. Cell Rep 15, 2563-2573.

1655 Sengupta, A., Bocchio, M., Bannerman, D.M., Sharp, T., and Capogna, M. (2017).
1656 Control of Amygdala Circuits by 5-HT Neurons via 5-HT and Glutamate Cotransmission.
1657 J Neurosci 37, 1785-1796.

1658 Shikanai, H., Yoshida, T., Konno, K., Yamasaki, M., Izumi, T., Ohmura, Y., Watanabe,
1659 M., and Yoshioka, M. (2012). Distinct neurochemical and functional properties of
1660 GAD67-containing 5-HT neurons in the rat dorsal raphe nucleus. J Neurosci 32, 14415-
1661 14426.

1662 Simic, G., Babic Leko, M., Wray, S., Harrington, C.R., Delalle, I., Jovanov-Milosevic, N.,
1663 Bazadona, D., Buee, L., de Silva, R., Di Giovanni, G.*, et al.* (2017). Monoaminergic
1664 neuropathology in Alzheimer's disease. Prog Neurobiol 151, 101-138.

1665 Siopi, E., Denizet, M., Gabellec, M.M., de Chaumont, F., Olivo-Marin, J.C., Guilloux,
1666 J.P., Lledo, P.M., and Lazarini, F. (2016). Anxiety- and Depression-Like States Lead to
1667 Pronounced Olfactory Deficits and Impaired Adult Neurogenesis in Mice. J Neurosci 36,
1668 518-531.

1669 Soghomonian, J.J., and Martin, D.L. (1998). Two isoforms of glutamate decarboxylase:
1670 why? Trends Pharmacol Sci 19, 500-505.

1671 Sos, K.E., Mayer, M.I., Cserep, C., Takacs, F.S., Szonyi, A., Freund, T.F., and Nyiri, G.
1672 (2017). Cellular architecture and transmitter phenotypes of neurons of the mouse
1673 median raphe region. Brain Struct Funct 222, 287-299.

1674 Soumier, A., Banasr, M., Kerkerian-Le Goff, L., and Daszuta, A. (2010). Region- and
1675 phase-dependent effects of 5-HT(1A) and 5-HT(2C) receptor activation on adult
1676 neurogenesis. Eur Neuropsychopharmacol 20, 336-345.

1677 Spaethling, J.M., Piel, D., Dueck, H., Buckley, P.T., Morris, J.F., Fisher, S.A., Lee, J.,
1678 Sul, J.Y., Kim, J., Bartfai, T.*, et al.* (2014). Serotonergic neuron regulation informed by in
1679 vivo single-cell transcriptomics. FASEB J 28, 771-780.

1680 Stanco, A., Pla, R., Vogt, D., Chen, Y., Mandal, S., Walker, J., Hunt, R.F., Lindtner, S.,
1681 Erdman, C.A., Pieper, A.A.*, et al.* (2014). NPAS1 represses the generation of specific
1682 subtypes of cortical interneurons. Neuron 84, 940-953.

1683 Steinbusch, H.W. (1981). Distribution of serotonin-immunoreactivity in the central
1684 nervous system of the rat-cell bodies and terminals. Neuroscience 6, 557-618.

1685 Steinbusch, H.W., van der Kooy, D., Verhofstad, A.A., and Pellegrino, A. (1980).
1686 Serotonergic and non-serotonergic projections from the nucleus raphe dorsalis to the
1687 caudate-putamen complex in the rat, studied by a combined immunofluorescence and
1688 fluorescent retrograde axonal labeling technique. Neurosci Lett 19, 137-142.

1689 Steinbusch, H.W., Verhofstad, A.A., and Joosten, H.W. (1978). Localization of serotonin
1690 in the central nervous system by immunohistochemistry: description of a specific and
1691 sensitive technique and some applications. Neuroscience 3, 811-819.

1692 Stuart, T., Butler, A., Hoffman, P., Hafemeister, C., Papalexi, E., Mauck, W.M., 3rd, Hao,
1693 Y., Stoeckius, M., Smibert, P., and Satija, R. (2019). Comprehensive Integration of
1694 Single-Cell Data. Cell 177, 1888-1902 e1821.

1695 Tasic, B. (2018). Single cell transcriptomics in neuroscience: cell classification and
1696 beyond. Curr Opin Neurobiol 50, 242-249.

1697 Tasic, B., Menon, V., Nguyen, T.N., Kim, T.K., Jarsky, T., Yao, Z., Levi, B., Gray, L.T.,
1698 Sorensen, S.A., Dolbeare, T.*, et al.* (2016). Adult mouse cortical cell taxonomy revealed
1699 by single cell transcriptomics. Nat Neurosci 19, 335-346.

1700 Tasic, B., Yao, Z., Graybuck, L.T., Smith, K.A., Nguyen, T.N., Bertagnolli, D., Goldy, J.,
1701 Garren, E., Economo, M.N., Viswanathan, S.*, et al.* (2018). Shared and distinct
1702 transcriptomic cell types across neocortical areas. Nature 563, 72-78.

1703 Teissier, A., Chemiakine, A., Inbar, B., Bagchi, S., Ray, R.S., Palmiter, R.D., Dymecki,
1704 S.M., Moore, H., and Ansorge, M.S. (2015). Activity of Raphe Serotonergic Neurons
1705 Controls Emotional Behaviors. Cell Rep 13, 1965-1976.

1706 Teng, T., Gaillard, A., Muzerelle, A., and Gaspar, P. (2017). EphrinA5 Signaling Is
1707 Required for the Distinctive Targeting of Raphe Serotonin Neurons in the Forebrain.
1708 eNeuro 4.

1709 Tong, C.K., Chen, J., Cebrian-Silla, A., Mirzadeh, Z., Obernier, K., Guinto, C.D., Tecott,
1710 L.H., Garcia-Verdugo, J.M., Kriegstein, A., and Alvarez-Buylla, A. (2014). Axonal control
1711 of the adult neural stem cell niche. Cell Stem Cell 14, 500-511.

1712 Tritsch, N.X., Ding, J.B., and Sabatini, B.L. (2012). Dopaminergic neurons inhibit striatal
1713 output through non-canonical release of GABA. Nature 490, 262-266.

1714 Trivellin, G., Bjelobaba, I., Daly, A.F., Larco, D.O., Palmeira, L., Faucz, F.R., Thiry, A.,
1715 Leal, L.F., Rostomyan, L., Quezado, M.*, et al.* (2016). Characterization of GPR101
1716 transcript structure and expression patterns. J Mol Endocrinol 57, 97-111.

1717 Trivellin, G., Hernandez-Ramirez, L.C., Swan, J., and Stratakis, C.A. (2018). An orphan
1718 G-protein-coupled receptor causes human gigantism and/or acromegaly: Molecular
1719 biology and clinical correlations. Best Pract Res Clin Endocrinol Metab 32, 125-140.

1720 Usoskin, D., Furlan, A., Islam, S., Abdo, H., Lonnerberg, P., Lou, D., Hjerling-Leffler, J.,
1721 Haeggstrom, J., Kharchenko, O., Kharchenko, P.V.*, et al.* (2015). Unbiased classification
1722 of sensory neuron types by large-scale single-cell RNA sequencing. Nat Neurosci 18,
1723 145-153.

1724 Vakalopoulos, C. (2017). Alzheimer's Disease: The Alternative Serotonergic Hypothesis
1725 of Cognitive Decline. J Alzheimers Dis 60, 859-866.

1726 Vasudeva, R.K., Lin, R.C., Simpson, K.L., and Waterhouse, B.D. (2011). Functional
1727 organization of the dorsal raphe efferent system with special consideration of nitrergic
1728 cell groups. J Chem Neuroanat 41, 281-293.

1729 Vasudeva, R.K., and Waterhouse, B.D. (2014). Cellular profile of the dorsal raphe lateral
1730 wing sub-region: relationship to the lateral dorsal tegmental nucleus. J Chem Neuroanat
1731 57-58, 15-23.

1732 Vertes, R.P. (1991). A PHA-L analysis of ascending projections of the dorsal raphe
1733 nucleus in the rat. J Comp Neurol 313, 643-668.

1734 Vertes, R.P., and Kocsis, B. (1994). Projections of the dorsal raphe nucleus to the
1735 brainstem: PHA-L analysis in the rat. J Comp Neurol 340, 11-26.

1736 Vincent, M.Y., Donner, N.C., Smith, D.G., Lowry, C.A., and Jacobson, L. (2018). Dorsal
1737 raphe nucleus glucocorticoid receptors inhibit tph2 gene expression in male C57BL/6J
1738 mice. Neurosci Lett 665, 48-53.

1739 Vincent, M.Y., and Jacobson, L. (2014). Glucocorticoid receptor deletion from the dorsal
1740 raphe nucleus of mice reduces dysphoria-like behavior and impairs hypothalamic-
1741 pituitary-adrenocortical axis feedback inhibition. Eur J Neurosci 39, 1671-1681.

1742 Voisin, A.N., Mnie-Filali, O., Giguere, N., Fortin, G.M., Vigneault, E., El Mestikawy, S.,
1743 Descarries, L., and Trudeau, L.E. (2016). Axonal Segregation and Role of the Vesicular
1744 Glutamate Transporter VGLUT3 in Serotonin Neurons. Front Neuroanat 10, 39.

1745 Walther, D.J., and Bader, M. (2003). A unique central tryptophan hydroxylase isoform.
1746 Biochem Pharmacol 66, 1673-1680.

1747 Walther, D.J., Peter, J.U., Bashammakh, S., Hortnagl, H., Voits, M., Fink, H., and Bader,
1748 M. (2003). Synthesis of serotonin by a second tryptophan hydroxylase isoform. Science
1749 299, 76.

1750 Wang, H.L., Zhang, S., Qi, J., Wang, H., Cachope, R., Mejias-Aponte, C.A., Gomez,
1751 J.A., Mateo-Semidey, G.E., Beaudoin, G.M.J., Paladini, C.A.*, et al.* (2019). Dorsal
1752 Raphe Dual Serotonin-Glutamate Neurons Drive Reward by Establishing Excitatory
1753 Synapses on VTA Mesoaccumbens Dopamine Neurons. Cell Rep 26, 1128-1142 e1127.

1754 Wang, R., Hausknecht, K., Shen, R.Y., and Haj-Dahmane, S. (2018). Potentiation of
1755 Glutamatergic Synaptic Transmission Onto Dorsal Raphe Serotonergic Neurons in the
1756 Valproic Acid Model of Autism. Front Pharmacol 9, 1185.

1757 Watanabe, M., Serizawa, M., Sawada, T., Takeda, K., Takahashi, T., Yamamoto, N.,
1758 Koizumi, F., and Koh, Y. (2014). A novel flow cytometry-based cell capture platform for
1759 the detection, capture and molecular characterization of rare tumor cells in blood. J
1760 Transl Med 12, 143.

1761 Weissbourd, B., Ren, J., DeLoach, K.E., Guenthner, C.J., Miyamichi, K., and Luo, L.
1762 (2014). Presynaptic partners of dorsal raphe serotonergic and GABAergic neurons.
1763 Neuron 83, 645-662.

1764 Wu, H.H., and Levitt, P. (2013). Prenatal expression of MET receptor tyrosine kinase in
1765 the fetal mouse dorsal raphe nuclei and the visceral motor/sensory brainstem. Dev
1766 Neurosci 35, 1-16.

1767 Wyler, S.C., Donovan, L.J., Yeager, M., and Deneris, E. (2015). Pet-1 Controls
1768 Tetrahydrobiopterin Pathway and Slc22a3 Transporter Genes in Serotonin Neurons.
1769 ACS Chem Neurosci 6, 1198-1205.

1770 Wyler, S.C., Spencer, W.C., Green, N.H., Rood, B.D., Crawford, L., Craige, C., Gresch,
1771 P., McMahon, D.G., Beck, S.G., and Deneris, E. (2016). Pet-1 Switches Transcriptional
1772 Targets Postnatally to Regulate Maturation of Serotonin Neuron Excitability. J Neurosci
1773 36, 1758-1774.

1774 Ye, W., Bouchard, M., Stone, D., Liu, X., Vella, F., Lee, J., Nakamura, H., Ang, S.L.,
1775 Busslinger, M., and Rosenthal, A. (2001). Distinct regulators control the expression of
1776 the mid-hindbrain organizer signal FGF8. Nat Neurosci 4, 1175-1181.

1777 Ye, Y., Zhao, Z., Xu, H., Zhang, X., Su, X., Yang, Y., Yu, X., and He, X. (2016).
1778 Activation of Sphingosine 1-Phosphate Receptor 1 Enhances Hippocampus
1779 Neurogenesis in a Rat Model of Traumatic Brain Injury: An Involvement of MEK/Erk
1780 Signaling Pathway. Neural Plast 2016, 8072156.

1781 Zeisel, A., Hochgerner, H., Lonnerberg, P., Johnsson, A., Memic, F., van der Zwan, J.,
1782 Haring, M., Braun, E., Borm, L.E., La Manno, G.*, et al.* (2018). Molecular Architecture of
1783 the Mouse Nervous System. Cell 174, 999-1014 e1022.

1784 Zeisel, A., Munoz-Manchado, A.B., Codeluppi, S., Lonnerberg, P., La Manno, G.,
1785 Jureus, A., Marques, S., Munguba, H., He, L., Betsholtz, C.*, et al.* (2015). Brain
1786 structure. Cell types in the mouse cortex and hippocampus revealed by single-cell RNA-
1787 seq. Science 347, 1138-1142.

1788 Zhang, P., Lu, H., Peixoto, R.T., Pines, M.K., Ge, Y., Oku, S., Siddiqui, T.J., Xie, Y., Wu,
1789 W., Archer-Hartmann, S.*, et al.* (2018). Heparan Sulfate Organizes Neuronal Synapses
1790 through Neurexin Partnerships. Cell 174, 1450-1464 e1423.

1791 Zweig, R.M., Ross, C.A., Hedreen, J.C., Steele, C., Cardillo, J.E., Whitehouse, P.J.,
1792 Folstein, M.F., and Price, D.L. (1988). The neuropathology of aminergic nuclei in
1793 Alzheimer's disease. Ann Neurol 24, 233-242.

1794

1795 **Figure Legends**

1796 Figure 1: High throughput scRNA-seq and clustering analyses reveal as many as
1797 fourteen distinct molecularly-defined subtypes (clusters) of *Pet1* neurons in the mouse
1798 DR. (A) Schematic depicting the experimental and analytical workflow, specifically: (1)
1799 brain dissection and DR microdissection, (2) cellular dissociation and microfluidic
1800 fluorescence-based cell sorting using the On-chip Sort, and (3) library preparation,
1801 sequencing, and analysis using 10X genomics, Illumina sequencing, and the R package
1802 Seurat, respectively. (B) Hierarchical clustering of *Pet1* neuron subtypes identified by
1803 Louvain clustering (using the top two thousand genes with the highest variance, PCs =
1804 1:5, 8:50, and resolution=0.9), with violin plots depicting the log-normalized expression
1805 of a common set of genes (*Tph2, Gad2, Gad1, Vglut3,* and *Met*) found useful for

1806 characterizing cluster structure across multiple resolutions (see Figure 1- figure
1807 supplement 2). (C) UMAP visualization of single-neuron transcriptome
1808 community/similarity structure, with colors and numbers indicating discrete clusters
1809 (same clustering parameters as (B)). (D) Heatmap depicting the scaled expression of the
1810 top five marker genes for each cluster (ranked by p-value, or in some cases fold
1811 enrichment).

1812 Figure 1 - figure supplement 1: Systematic variation of key clustering parameters allows
1813 for exploration of the community structure of DR *Pet1* single neuron transcriptomes at
1814 variable resolutions. (A) Scatterplot of the variance (standard deviation, Y-axis)
1815 explained by the first 250 principal components (X-axis). (B) Level plot/heat map
1816 depicting the number of clusters (DR *Pet1* neuron subtypes) resulting from variation of
1817 the number of included principle components (Y-axis) and the resolution parameter to
1818 the Seurat function FindClusters (X-axis). (C) Line graph of the frequency (Y-axis) that a
1819 given number of clusters (X-axis) arises from the analysis performed in B. (D) Plots
1820 showing the parameters (white) that lead to cluster numbers found to have the highest
1821 frequency (5, 11, 14, and 17 clusters, top left to bottom right respectively).

1822 Figure 1 - figure supplement 2: Analysis of clusters at successively increasing resolution
1823 values. (A, D, G) Hierarchical clustering of *Pet1* neuron subtypes identified by Louvain
1824 clustering at varying resolutions (specifically, the resolution value passed to the Seurat
1825 function FindClusters A= 0.1, D= 0.3, G= 0.7), and violin plots depicting the normalized
1826 expression of *Tph2, Gad2, Gad1, Vglut3,* and *Met.* (B, E, H) UMAP visualization of
1827 community structure at a given resolution (B= 0.1, E= 0.3, H= 0.7). (C, F, I) Heatmap
1828 depicting the scaled expression of the top five marker genes for each cluster (ranked by
1829 p-value).

1830 Figure 1 - figure supplement 3: Expression of serotonin-related genes across DR *Pet1*
1831 neuron subtypes. Violin plots depicting the log-normalized expression of twelve
1832 serotonin neuron marker genes across the fourteen *Pet1* neuron clusters.

1833 Figure 2: Expression patterns of a subset of highly variable genes classified by biological
1834 function. Dot plots show the expression of a gene (Y-axis) in each cluster (X-axis),
1835 separated by biological function. The size of the dot represents the percentage of cells
1836 expressing the gene and saturation of color represents average normalized expression

1837 level. For convenience, the UMAP plot from Figure 1C is re-displayed at the bottom right
1838 to help link gene expression patterns to overall cluster structure. Minimum inclusion
1839 criteria for genes was that they were among the top 2000 highest variance genes and/or
1840 they were found to be significantly enriched or “de-enriched” in at least one subtype
1841 cluster (see **Methods**).

1842 Figure 3: Intersectionally targeted *Pet1* neuron subtypes have different anatomical
1843 distributions in subregions of the DR. (A-E) Low magnification view of 40 µm coronal
1844 sections showing the DR from rostral to caudal (1-6) in triple transgenic animals. Cell
1845 bodies are labeled by the intersectional expression of a Cre driver of interest, *Pet1::Flpe*,
1846 and the intersectional allele *FrePe* (green eGFP marked cells expressing both Cre and
1847 Flpe and red mCherry expressing *Pet1::Flpe* subtractive population) unless otherwise
1848 noted. (A) *Sert::cre; Pet1::Flpe; FrePe*, (B) *Vglut3::cre; Pet1::Flpe; hM3Dq* (green
1849 mCherry-hM3Dq marked cells expressing Cre and Flpe and red eGFP expressing
1850 *Pet1::Flpe* subtractive population), (C) *Npy2r::IRES-cre; Pet1::Flpe; FrePe*, (D)
1851 *P2ry1::IRES-cre; Pet1::Flpe; FrePe*. Top row shows violin plots depicting transcript
1852 expression (10X scRNA-seq data) of the respective gene corresponding with each Cre
1853 driver. Scale bar (A1) equals 100 µm.

1854 Figure 3 - figure supplement 1: TPH2 and VGLUT3 antibody staining of *Pet1* neurons is
1855 anatomically biased within different DR subdomains. (A) Bar graph showing the
1856 percentage of *Pet1* cells that are TPH2-negative in a specific anatomical subdivision of
1857 the DR in an *En1::cre; Pet1::Flpe; RC::FrePe* (Green labeled neurons with intersectional
1858 expression of *En1::cre* and *Pet1::Flpe)*. Anatomical subdivisions (Dorsomedial (dmDR),
1859 Medial (mDR), Ventromedial (vmDR)) are depicted in the coronal photomicrographs
1860 from D-I, from rostral (left) to caudal (right). n=2, bar graph depicting the mean with
1861 SEM. (B) TPH2 immunostaining in an *En1::cre; Pet1::Flpe; RC::FrePe* coronal section.
1862 Open arrow indicates an example of a TPH2+ *En1::cre; Pet1::Flpe* cell and the closed
1863 arrow indicates a TPH2- *En1::cre; Pet1::Flpe* cell. (C) VGLUT3 immunostaining in a
1864 *Vglut3::IRES-cre; Pet1::Flpe; RC::FL-hM3Dq* coronal section (green indicating neurons
1865 labeled by the intersection of *Vglut3::IRES-cre* and *Pet1::Flpe*, red indicating the
1866 subtractive *Pet1* population). Open arrow shows an example of a VGLUT3
1867 immunopositive *Vglut3::cre; Pet1::Flpe* cell, closed arrow shows a VGLUT3
1868 immunonegative subtractive *Pet1* cell. Scale bar in B and C equals 25 µm. (D-I)
1869 Quantification of the percentage of VGLUT3 immunoreactive *Vglut3::cre; Pet1::Flpe*

1870 lineage (dark green) and VGLUT3 immunoreactive subtractive *Pet1* lineage cells (dark
1871 red) within anatomical subdivisions of the dorsal raphe from rostral (D) to caudal (I), in
1872 comparison to VGLUT3 immunonegative *Vglut3*::cre;*Pet1::Flpe* and subtractive *Pet1*
1873 neurons (light green and light red respectively). Low magnification images indicate
1874 representative quantified images. Anatomical subdivisions (dorsomedial (dm), medial
1875 (m), ventromedial (vm) and dorsolateral (dl)) are delineated with white brackets. Scale
1876 bar in D equals 100 μm, n=2, bar graph depicts mean with SEM. (J) Summary coronal
1877 brainstem schematic showing the distribution of VGLUT3 immuno-positive and immuno-
1878 negative *Vglut3::cre; Pet1::Flpe* (dark and light green) and subtractive *Pet1* neurons
1879 (dark and light red) in the DR from rostral (left) to caudal (right).

1880 Figure 4: scRNA-seq of *Pet1* neurons sorted from anatomical subdomains map onto
1881 specific 10x scRNA-seq clusters. (A) Schematic of the pipeline used for manual sorting
1882 and sequencing, including referenced anatomical subdomains mapped onto
1883 representative images of the DR. *Pet1* neurons are in green. (B) Dot plot mapping
1884 manually sorted cells from a given genotype and anatomical subdomain (Y-axis) to the
1885 fourteen 10x clusters (X-axis). The size of the dot indicates the percentage of single cells
1886 from a genotype/anatomical region attributed to a reference cluster. Note, the asterisks
1887 after *Drd2::cre;Pet1::Flpe* is to denote that these data come from a previously published
1888 study (Niederkofler, et al. 2016), and these particular single-cell libraries were prepared
1889 using the Nugen Ovation RNA-seq System v2 kit, rather than SMART-Seq v4. The
1890 expression of a selection of highly variable and cluster marker genes is depicted in
1891 Figure 4- figure supplement 1.

1892 Figure 4 – figure supplement 1: Expression patterns of a selection of highly variable and
1893 cluster marker genes that show anatomical bias. Dot plot depicting the expression of
1894 genes (Y-axis) across manually sorted cells from a specific subdomain and genotype
1895 (left) and 10x scRNA-seq clusters (right). The size of the dot represents the percentage
1896 of cells expressing the gene and saturation of color represents the average normalized
1897 expression level. As with Figure 4, the asterisks after *Drd2::cre;Pet1::Flpe* denotes that
1898 these data come from a previously published study (Niederkofler, et al. 2016), and these
1899 particular single-cell libraries were prepared using the Nugen Ovation RNA-seq System
1900 v2 kit, rather than SMART-Seq v4.

1901 Figure 4 - figure supplement 2: PAX5 and SATB2 are expressed predominately in rostral
1902 dorsomedial and dorsolateral *Pet1* neurons while NR2F2 is expressed predominately in
1903 caudal *Pet1* neurons. (A) Representative regions of the DR used for quantification of
1904 immunostaining from rostral (left) to caudal (right). Brackets indicate anatomical
1905 subdivisions- dorsomedial (dmDR, dark blue), medial (mDR, tan), ventromedial (vmDR,
1906 gray), and dorsolateral (dlDR, light blue). (B-D) (top) Distribution of normalized transcript
1907 expression of *Pax5* (B), *Satb2* (C) or *Nr2f2* (D) within *Pet1* neuron subtypes and
1908 (bottom) the percentage of counted *Pet1* neurons immunoreactive for PAX5 (B), SATB2
1909 (C) or NR2F2 (D) that are arising from *Vglut3::cre; Pet1::Flpe* neurons (dark grey) in
1910 comparison to the subtractive *Pet1* population (light grey). (B'-D') Bar graph depicting
1911 the percentage of *Pet1* neurons immunopositive for PAX5 (B'), SATB2 (C') or NR2F2
1912 (D') in anatomical subdivisions of the DR from rostral to caudal. n=2- 4 depending on
1913 rostral to caudal section, bar graph depicting mean with SEM. (B''-D'') Representative
1914 coronal confocal image depicting a region of the DR with *Pet1* neurons immunopositive
1915 for PAX5 (B''), SATB2 (C'') or NR2F2 (D''). *Vglut3::cre;Pet1::Flpe* cells are shown in
1916 green, subtractive *Pet1* cells in red, and antibody of interest in blue. (E) Coronal
1917 brainstem schematics depicting the anatomical distribution of *Pet1* neurons (top)
1918 expressing PAX5 and NR2F2, or (bottom) that are expressing *Gad2-Tph2, Vglut3-Tph2,*
1919 or *Vglut3* only from rostral (right) to caudal (left).

1920 Figure 5: *P2ry1::cre; Pet1::Flpe* neurons project throughout the ventricles and are in
1921 close apposition to proliferating cells in the SVZ and RMS. (A) Flat mount of the lateral
1922 wall of the lateral ventricle of a *P2ry1::cre;Pet1::Flpe;Ai65* animal, where
1923 *P2ry1::cre;Pet1::Flpe* fibers are in grey. Scale bar = 100 µm. (B-E) High magnification
1924 confocal images from regions of the lateral wall represented in red boxes in A. Scale bar
1925 (B) = 100 µm. (F) 3D brain schematic showing the *P2ry1::cre;Pet1:Flpe* cell bodies (dark
1926 orange) in the caudal part of the DR (light orange) and fibers (dark orange) projecting
1927 through the ventricles (grey) and along the migrating neuroblasts of the rostral migratory
1928 stream (RMS, blue). (G-H) Coronal confocal images depicting *P2ry1::cre;Pet1::Flpe*
1929 fibers (orange) from *P2ry1::cre;Pet1::Flpe;Ai65* animals in the SVZ (G) and RMS (H).
1930 Proliferating cells labeled with Ki67 (grey) and migrating neuroblasts labeled with
1931 doublecortin (DCX, blue). Scale bar (G, H) = 50 µm

1932 Figure 6: *P2ry1::cre;Pet1::Flpe* neurons have a distinct firing phenotype. (A) Example
1933 voltage traces from a neuron type that started firing action potentials with short latency

1934 (mean= 17.32 ms ± 6.61 at 200 pA), in response to 750 ms current pulses. (B) Example
1935 traces from a neuron type that started firing action potentials with medium latency
1936 (mean= 64.18 ms ± 9.8 at 200 pA). (C) Example traces from a neuron that started firing
1937 action potentials with long latency (mean= 476.55 ms ± 223.64 at 200 pA). (D) Example
1938 traces from a neuron that fired action potentials with short latency (mean= 12.6 ms ± 5.9
1939 at 200 pA) and that displayed frequency adaptation. (E) Frequency-Current curves show
1940 *P2ry1::cre; Pet1::Flpe* neurons (tdTomato$^+$ *P2ry1::IRES-cre;Pet1::Flpe;Ai65,* n=9; 3
1941 animals; red circles) are less excitable than nearby caudodorsal raphe non-
1942 *P2ry1::cre;Pet1::Flpe* populations (eGFP$^+$ *P2ry1::IRES-cre;Pet1::Flpe;RC::FL-hM3Dq,*
1943 n=8; 3 animals; black squares) or neurons from the dorsomedial and dorsolateral Raphe
1944 *Gad2::cre;Pet1::Flpe* population (tdTomato$^+$ *Gad2::IRES-cre;Pet1::Flpe;Ai65*, n=12; 2
1945 animals; blue diamonds) $p<0.0001$ Kruskal-Wallis test. (F) Heat map shows the
1946 distribution of firing types of recorded cells according to genotype, note that while firing
1947 type B is the most frequent overall, all recorded *P2ry1::cre; Pet1::Flpe* neurons belong to
1948 type D.

1949 Figure 6- figure supplement 1: Key membrane properties distinguish serotonergic
1950 neuron firing types. Groups are same as in Figure 6; all *P2ry1::IRES-cre;*
1951 *Pet1::Flpe;RC::Ai65* neurons belong to group D. (A) Scatterplot of rheobase (in pA)
1952 exhibited by each cell of the corresponding firing type. (B) Scatterplot of the latency of
1953 each cell to fire the first action potential after the onset of the depolarizing current pulse
1954 by the corresponding firing type. (C) Same as B except firing type D was split into
1955 subgroups Da and Db, based on bi-modality visible in B. (D) Scatterplot of the maximum
1956 firing frequency (in Hz) exhibited by each cell of the corresponding firing type. (E)
1957 Scatterplot of the membrane resistance (in MΩ), exhibited by each cell of the
1958 corresponding firing type. (F) Scatterplot of the average half-width of the action potential
1959 of each firing type at maximum firing rate (in ms). Dashed lines indicate the median.
1960 Asterisks indicate statistical significance, Kruskal-Wallis test *$p < 0.05$, **$p < 0.01$, ***$p <$
1961 0.001, ****$p < 0.0001$.

1962 Figure 7: Correspondence of serotonin subtypes identified in previous studies (Y-axis) to
1963 the fourteen 10x clusters identified in this study (X-axis). The size of the dot indicates the
1964 percentage of single cells from the original cluster that are attributed to a given reference
1965 cluster.

1966 Figure 8: Fourteen *Pet1* subtypes in the DR can be defined by the combinatorial
1967 expression of transcription factors and other markers and have distinct anatomical
1968 organization. (A) Molecular markers (neurotransmitters (NTs), transcription factors (TFs),
1969 and other markers) on the left half of the table, with increasing specificity from left to
1970 right, that combinatorically define each identified *Pet1* subtype (colored column).
1971 Anatomical biases of each cluster are described on the right, with increasing specificity
1972 from right to left. Note, cluster numbers have been re-ordered to highlight anatomical
1973 groupings.

1974 Supplemental Excel Spreadsheet: The “all_subgroup_markers” worksheet displays the
1975 output of the Seurat FindAllMarkers function. Column one is the gene symbol, column
1976 two is the p-value given by the Wilcoxon Rank Sum test, column three is the average
1977 “log fold change” (i.e. log-fold difference in transcript abundance between the in-group
1978 and out-group), where a positive value indicates that a gene is expressed at a higher
1979 level in a given cluster relative to all other clusters, and a negative value indicates that a
1980 gene is expressed at a lower level. Column four is the percent of cells within a particular
1981 cluster in which the gene was detected, column five is the percent of cells within all other
1982 clusters in which a gene was detected, column six gives the Bonferroni-corrected p-
1983 value, and column seven indicates the cluster in which the given gene is a positive or
1984 negative marker. Note, not all enriched genes are unique to only one cluster, as more
1985 similar clusters will share subsets of enriched genes. The “sig_var_genes” worksheet
1986 lists the top two thousand highest “standardized variance” genes, i.e. genes that vary
1987 significantly more than expected based on mean expression.

Figure 1

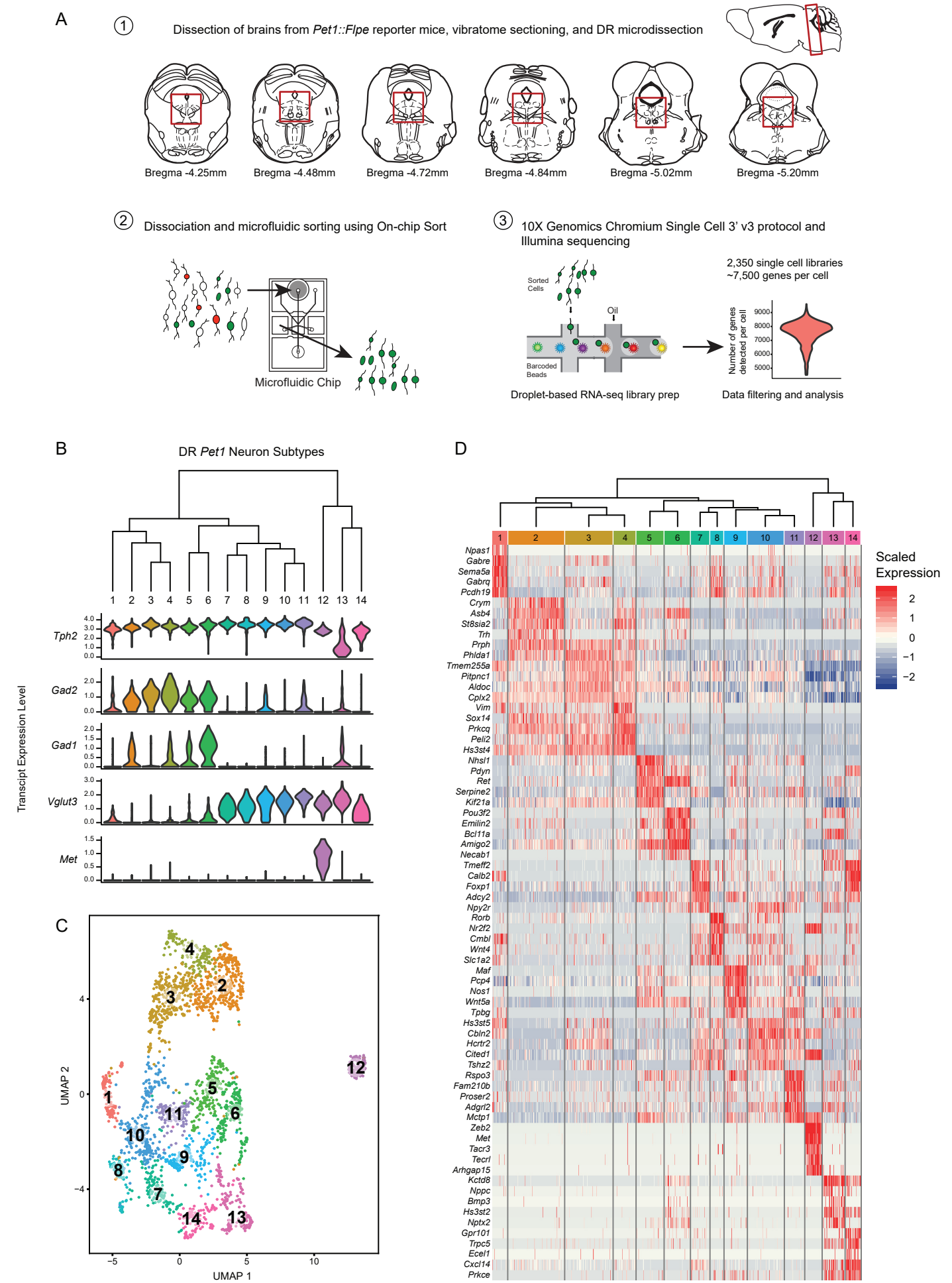
A
1
Dissection of brains from Pet1::Flpe reporter mice, vibratome sectioning, and DR microdissection
Bregma -4.25mm
Bregma -4.48mm
Bregma -4.72mm
Bregma -4.84mm
Bregma -5.02mm
Bregma -5.20mm
2
Dissociation and microfluidic sorting using On-chip Sort
Microfluidic Chip
3
10X Genomics Chromium Single Cell 3' v3 protocol and Illumina sequencing
Sorted Cells
Oil
Barcoded Beads
Droplet-based RNA-seq library prep
2,350 single cell libraries
~7,500 genes per cell
Number of genes detected per cell
Data filtering and analysis
B
DR Pet1 Neuron Subtypes
Tph2
Gad2
Gad1
Vglut3
Met
Transcipt Expression Level
C
UMAP 1
UMAP 2
D
Scaled Expression
Npas1
Gabre
Sema5a
Gabrq
Pcdh19
Crym
Asb4
St8sia2
Trh
Prph
Phlda1
Tmem255a
Pitpnc1
Aldoc
Cplx2
Vim
Sox14
Prkcq
Peli2
Hs3st4
Nhsl1
Pdyn
Ret
Serpine2
Kif21a
Pou3f2
Emilin2
Bcl11a
Amigo2
Necab1
Tmeff2
Calb2
Foxp1
Adcy2
Npy2r
Rorb
Nr2f2
Cmbl
Wnt4
Slc1a2
Maf
Pcp4
Nos1
Wnt5a
Tpbg
Hs3st5
Cbln2
Hcrtr2
Cited1
Tshz2
Rspo3
Fam210b
Proser2
Adgrl2
Mctp1
Zeb2
Met
Tacr3
Tecrl
Arhgap15
Kctd8
Nppc
Bmp3
Hs3st2
Nptx2
Gpr101
Trpc5
Ecel1
Cxcl14
Prkce

Figure 1- figure supplement 1

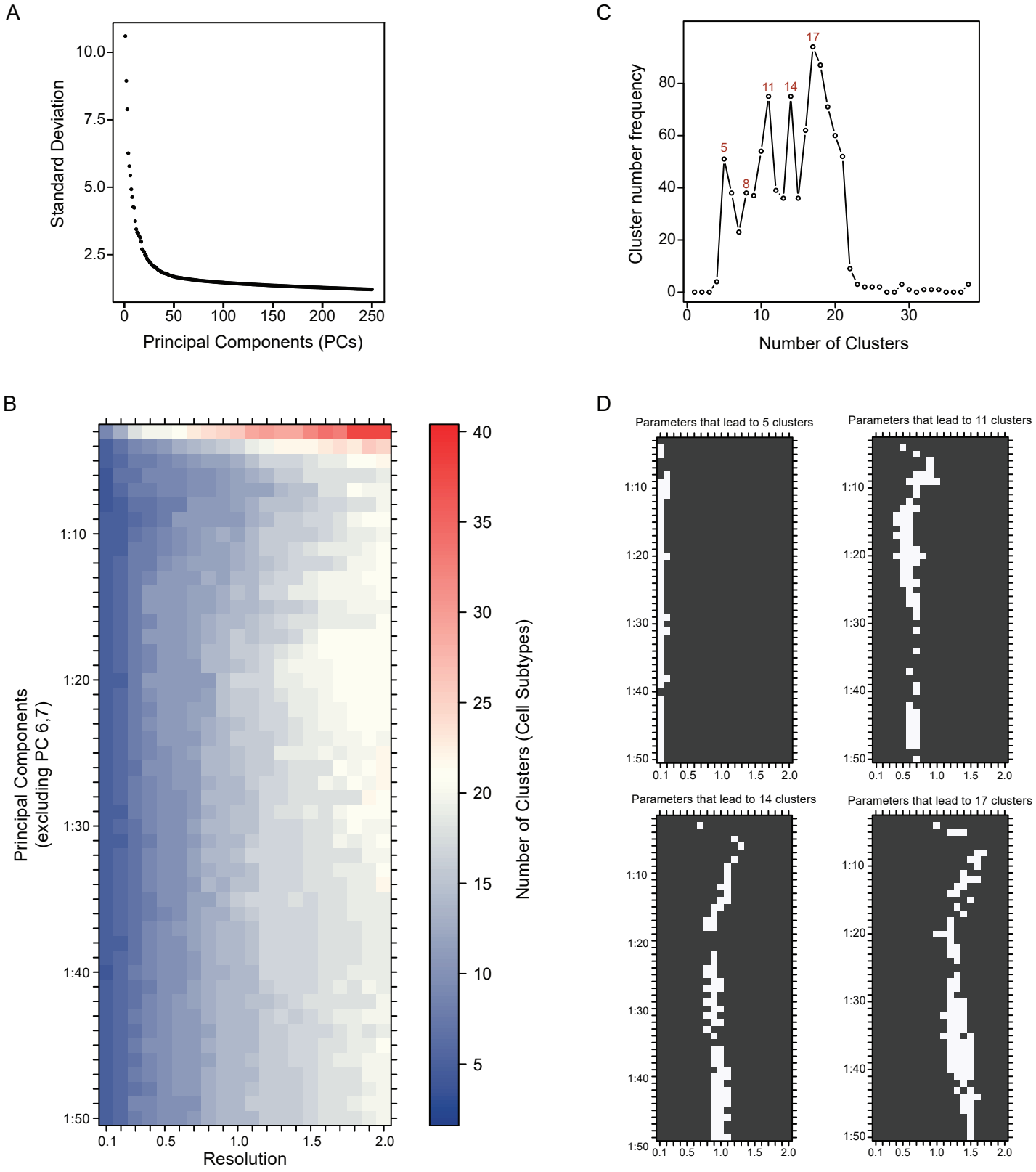

Figure 1- figure supplement 2

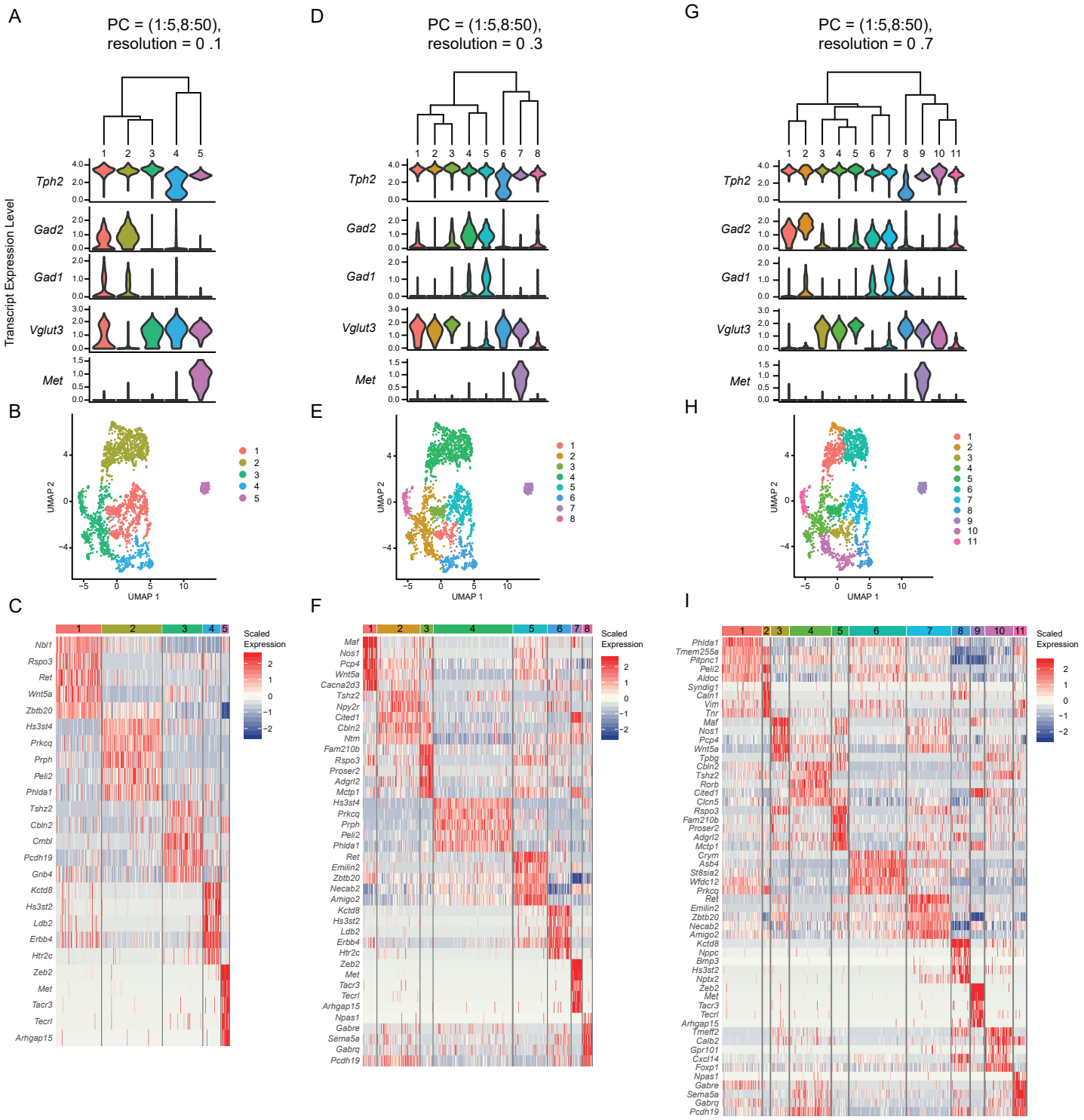

Figure 1- figure supplement 3

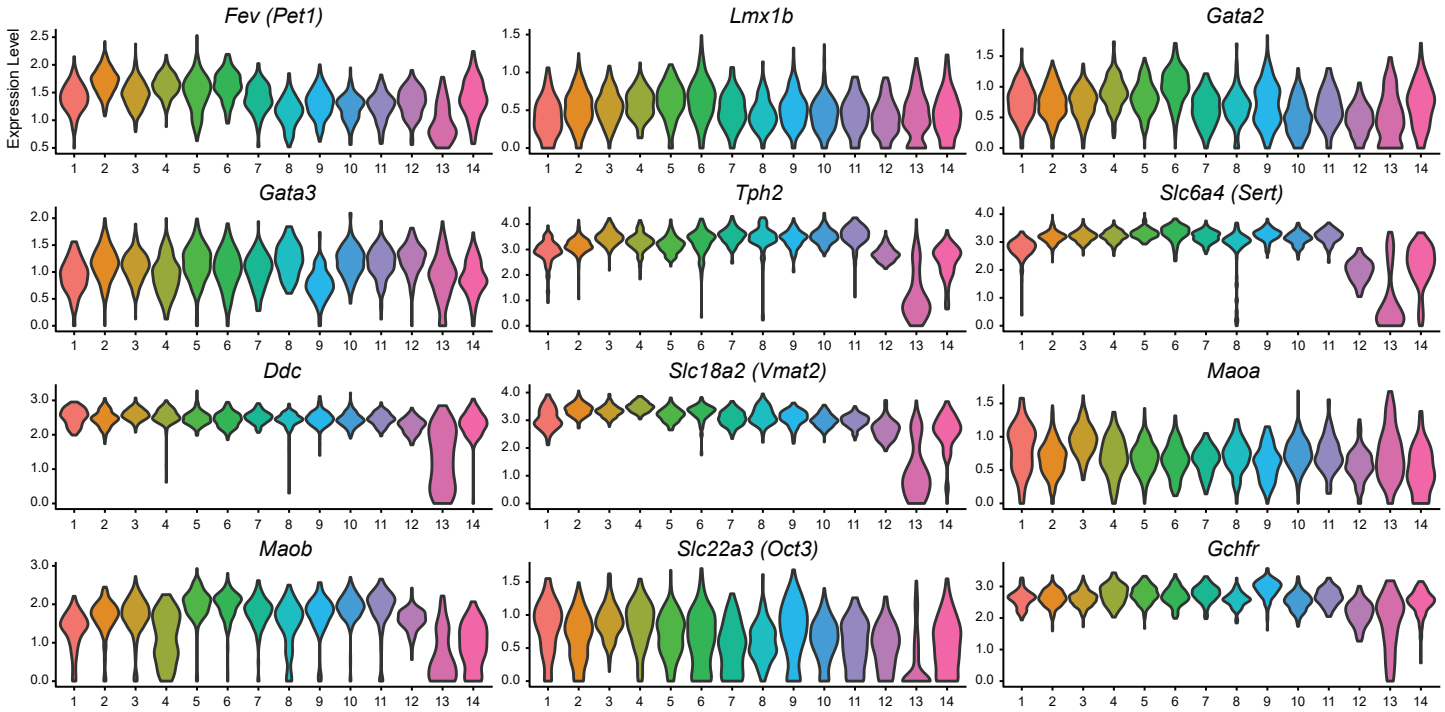

Figure 2

Transcription Factors
Fev
En1
En2
Nr3c1
Npas3
Pou3f1
Npas1
Pax5
Pou6f2
Klf5
Pou3f3
Sox14
Satb2
Barx2
Kit
Bcl11b
Esr2
Zbtb20
Pou3f2
Bcl11a
Id2
Scx
Zfp536
Foxp1
Lmo2
Sox5
Rorb
Mn1
Maf
Esr1
Mef2c
Foxa1
Mafb
Cited1
Nr2f2
Zeb2
Tox3
Lmo1
Uncx
Nr2f1
Lmo4
Tcf4
Egr1
Nfix
Nfib
Satb1
Ldb2
Sox4
Neurotransmitters and Neuropeptides
Tph2
Slc18a2
Chgb
Chga
Gad2
Gad1
Trh
Pdyn
Gal
Slc17a8
Ghrh
Adcyap1
Nos1
Crh
Nmb
Npb
Penk
Sst
Ionotropic Receptors
Gabrq
Gabre
Gria1
Grin3a
Gabrg3
Grin2a
Chrna4
Gabra2
Gabrg2
Gabra1
Gria3
Gabra5
Grik3
Cellular Calcium Ion Homeostasis
S100a10
S100a11
S100a16
Calb1
Necab2
Necab1
Calb2
Ryr2
S100b
Ryr3
G Protein-Coupled Receptors
Gabbr1
Adra1b
Adra2c
Htr1a
Htr1b
Htr1d
Hcrtr1
Hrh1
Grm1
Adra2a
Hrh3
Gpr149
Prokr2
Npy2r
Grm7
Htr5b
Ptger3
Cckar
Gpr35
Gpr88
Grm8
Hcrtr2
Crhr2
Oxtr
Calcr
Chrm2
Grm5
Lpar1
S1pr3
P2ry1
Rxfp1
Tacr3
Oprm1
Ptger4
Chrm1
Gabbr2
Cnr1
Htr2c
Gpr22
Htr7
Sstr2
Sstr1
Tacr1
Oprk1
Galr1
Gpr101
Plasma Membrane Ion Channels
Scn9a
Cacng3
Kcnh7
Kcnq3
Kcnc4
Cacng4
Kcnip1
Clic1
Scn7a
Kcng4
Kcnn3
Cacna1e
Cacna1i
Kcnab1
Kcnj4
Kcnc1
Hcn1
Kcnb2
Cachd1
Kcnc2
Cacna2d3
Kcnf1
Cacng5
Kcna1
Kcnj12
Kcnd2
Kcna4
Trpc3
Kctd8
Kcnk2
Kcnip4
Kctd4
Kcnh5
Kcnh8
Trpc5
Regulators of Heparan Sulfate Proteoglycans
Hs3st4
Hs3st5
Ndst3
Hs3st1
Ext1
Ndst4
Hs3st6
Sulf2
Hs3st2
Hs3st3a1
Sulf1
Regulators of Neuron Projections and Synaptic Connectivity
Fgf13
Pcdh19
Sema5a
Cdh11
Cdh18
Pcdh18
Prph
Robo2
Cdh13
Sema6a
Cdh22
Flrt2
Cdh4
Plxna2
Plxnd1
Cntn4
Amigo2
Robo1
Nptx1
Fgf18
Cbln1
Pcdh17
Wnt4
Wnt5a
Sema6d
Plxna4
Pcdh15
Fgf9
Ntn1
Cdh7
Pcdh7
Ntng1
Cbln2
Sema3c
Epha7
Fgf1
Epha6
Pcdh20
Fgf11
Epha3
Cbln4
Cdh8
Pcdh8
Ephb1
Sema3e
Reln
Epha4
Fgf10
Pcdh11x
Efna5
Efnb3
Slit2
Nrp2
Sema3d
Nrp1
Efnb2
Kinases and Kinase Inhibitors
Prkcb
Pkib
Prkca
Prkcq
Ret
Igf1r
Cdkn1a
Prkcd
Lats2
Ror2
Met
Camk2d
Erbb4
Prkg1
Prkg2
Average Expression
Percent Expressed
UMAP 1
UMAP 2

Figure 3

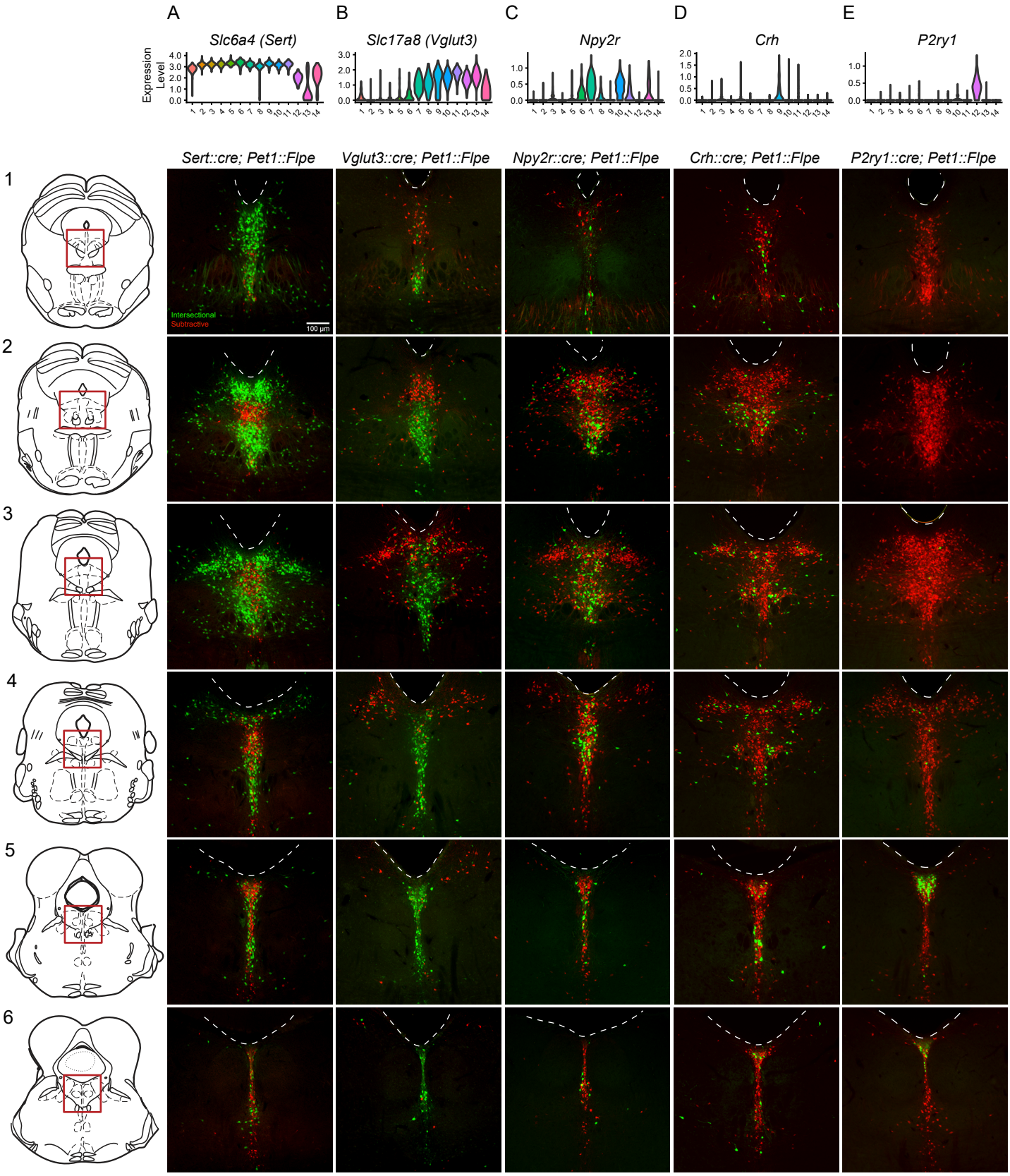
A
B
C
D
E
Slc6a4 (Sert)
Slc17a8 (Vglut3)
Npy2r
Crh
P2ry1
Expression Level
Sert::cre; Pet1::Flpe
Vglut3::cre; Pet1::Flpe
Npy2r::cre; Pet1::Flpe
Crh::cre; Pet1::Flpe
P2ry1::cre; Pet1::Flpe
1
2
3
4
5
6
Intersectional
Subtractive
100 µm

Figure 3 - figure supplement 1

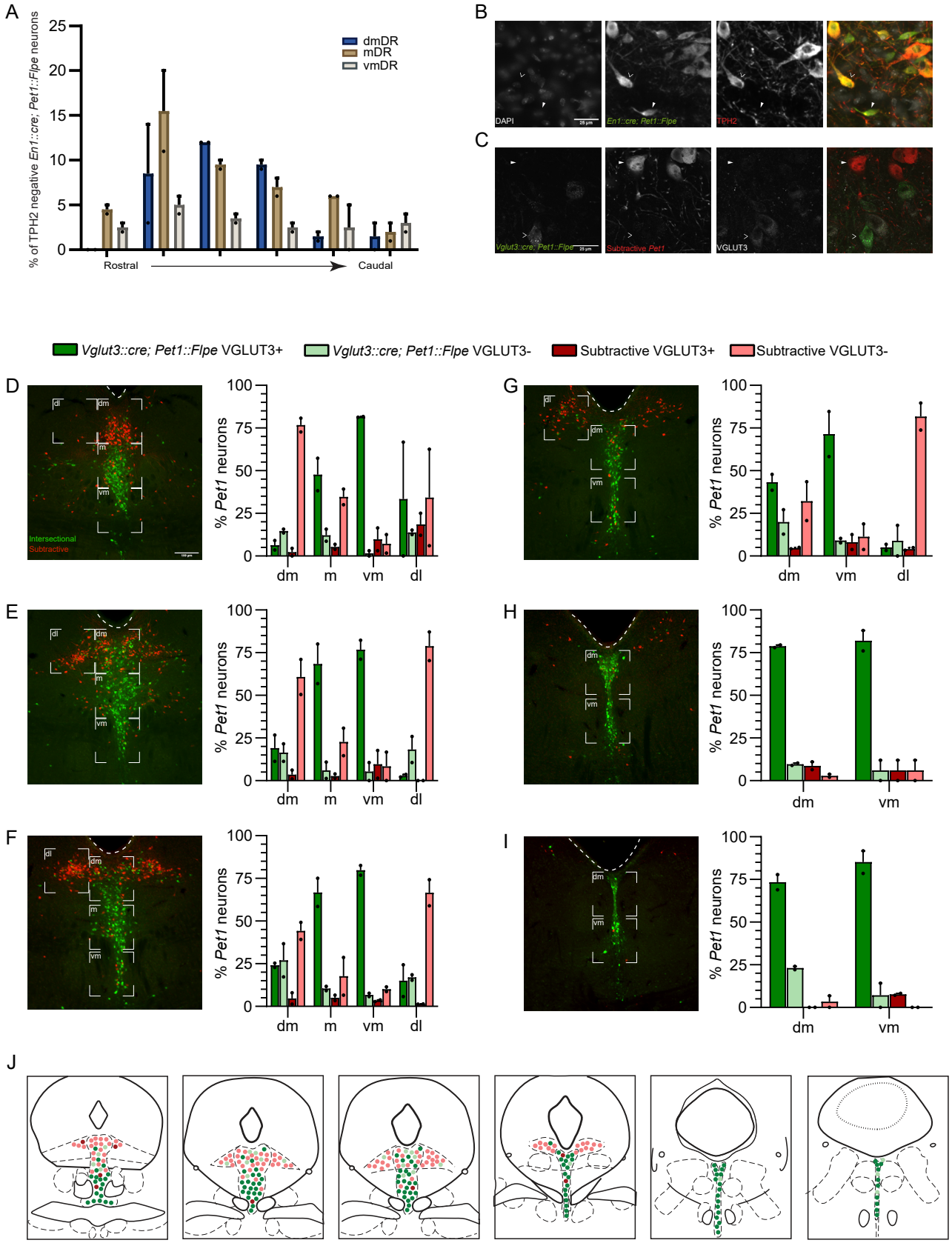

Figure 4

A

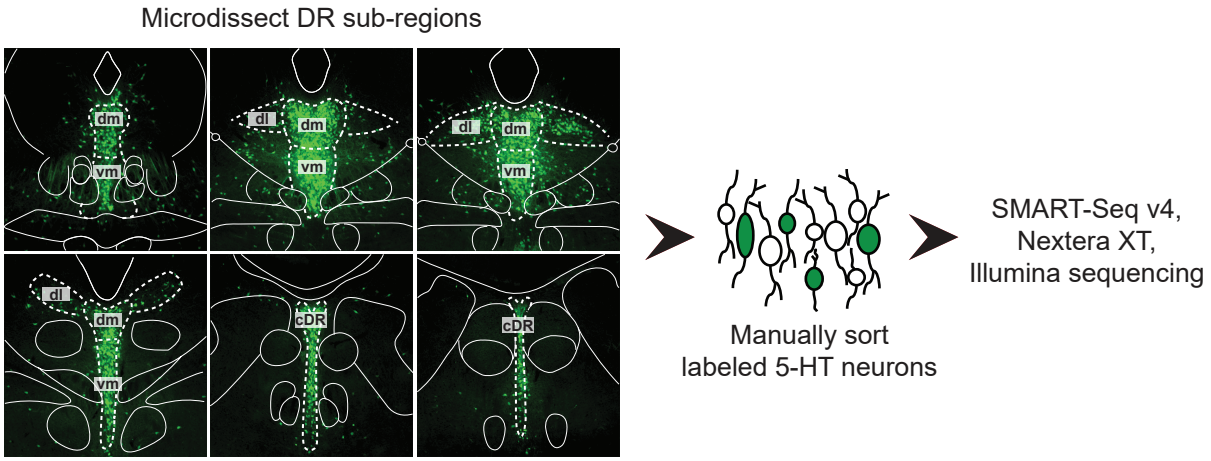
Microdissect DR sub-regions
dm
vm
dl
cDR
Manually sort
labeled 5-HT neurons
SMART-Seq v4,
Nextera XT,
Illumina sequencing

B

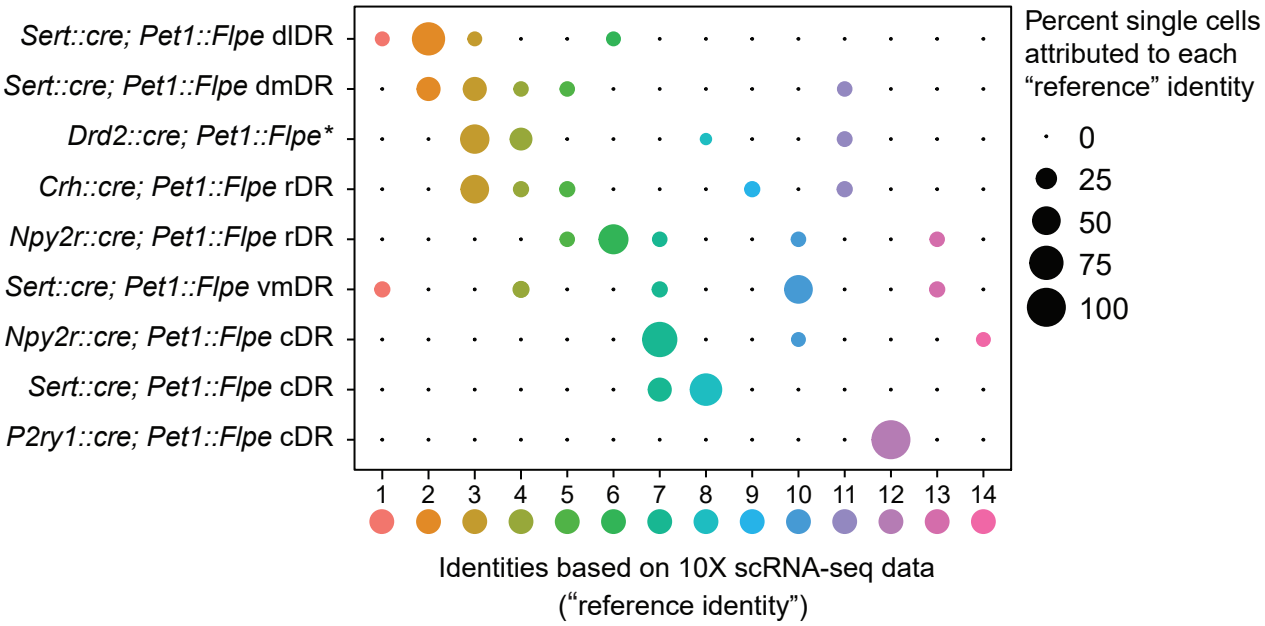
Sert::cre; Pet1::Flpe dlDR
Sert::cre; Pet1::Flpe dmDR
Drd2::cre; Pet1::Flpe*
Crh::cre; Pet1::Flpe rDR
Npy2r::cre; Pet1::Flpe rDR
Sert::cre; Pet1::Flpe vmDR
Npy2r::cre; Pet1::Flpe cDR
Sert::cre; Pet1::Flpe cDR
P2ry1::cre; Pet1::Flpe cDR
1 2 3 4 5 6 7 8 9 10 11 12 13 14
Identities based on 10X scRNA-seq data
("reference identity")
Percent single cells
attributed to each
"reference" identity
0
25
50
75
100

Figure 4 - figure supplement 1

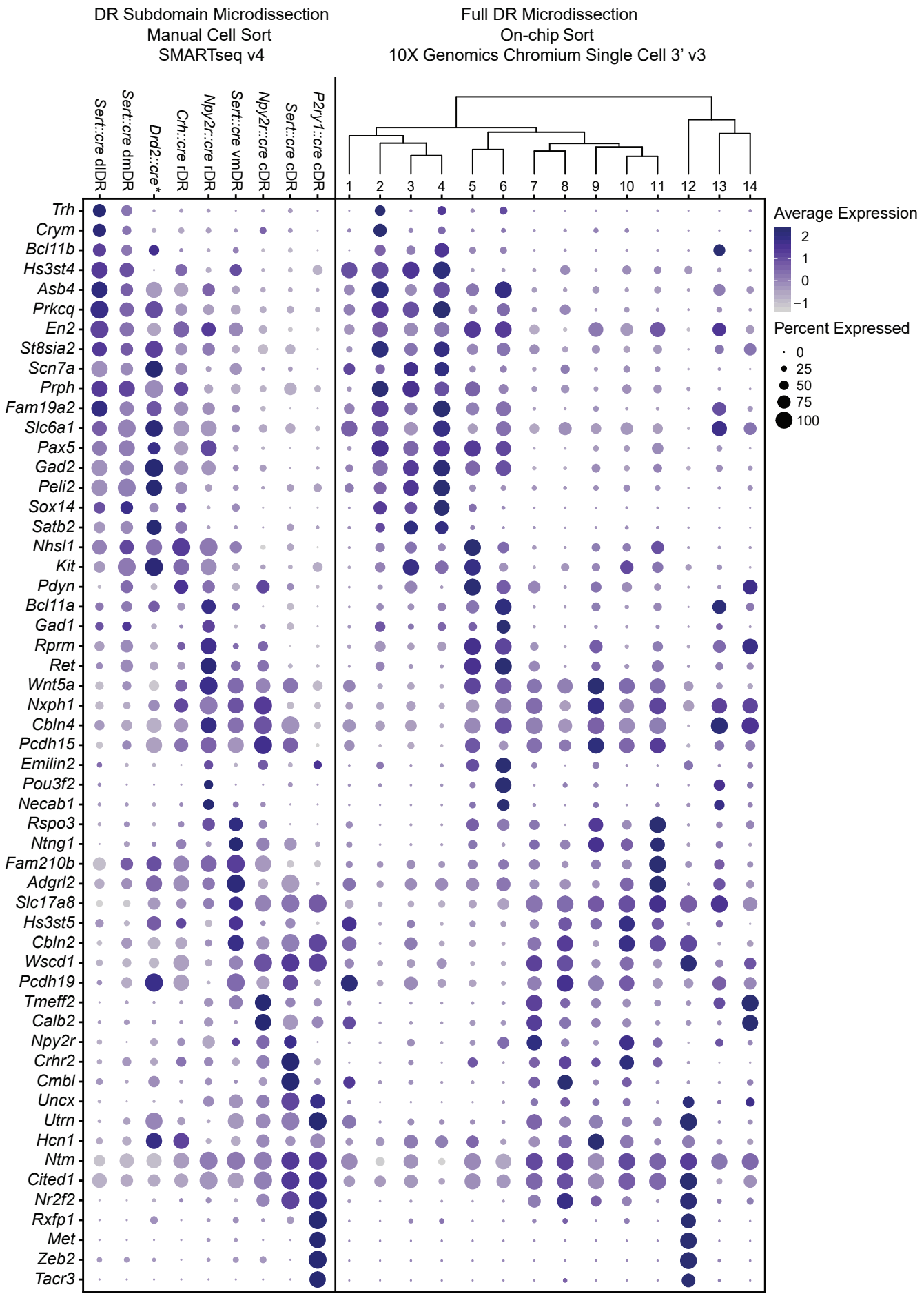

Figure 4 - figure supplement 2

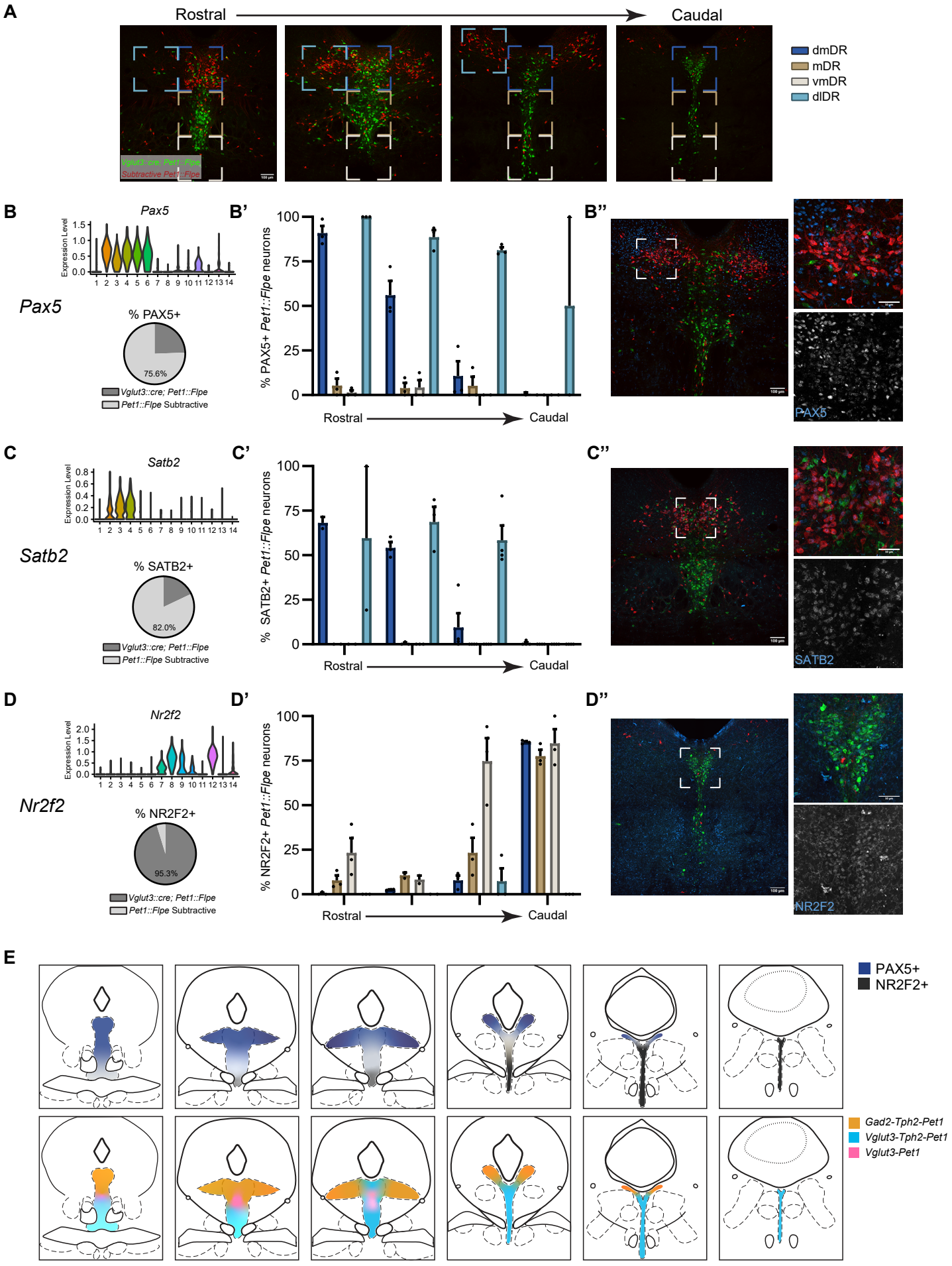

Figure 5

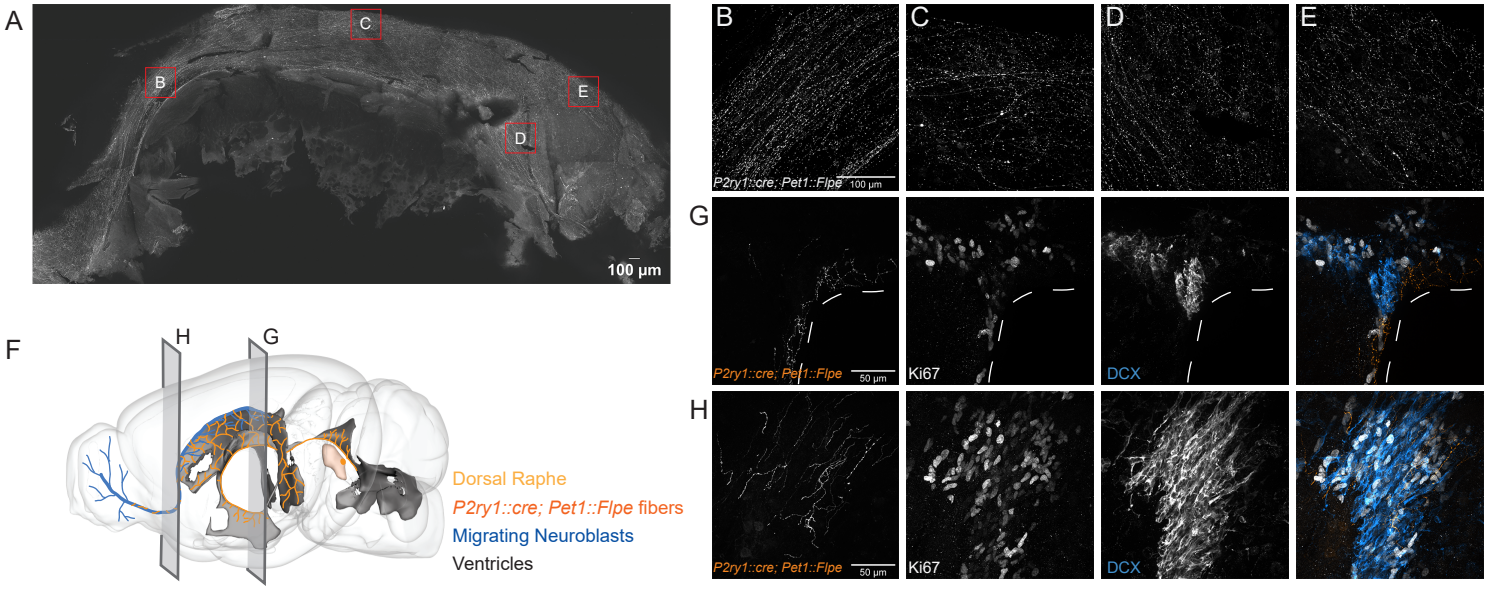
A
B
C
D
E
100 µm
F
H
G
Dorsal Raphe
P2ry1::cre; Pet1::Flpe fibers
Migrating Neuroblasts
Ventricles
B
C
D
E
P2ry1::cre; Pet1::Flpe
100 µm
G
P2ry1::cre; Pet1::Flpe
50 µm
Ki67
DCX
H
P2ry1::cre; Pet1::Flpe
50 µm
Ki67
DCX

Figure 6

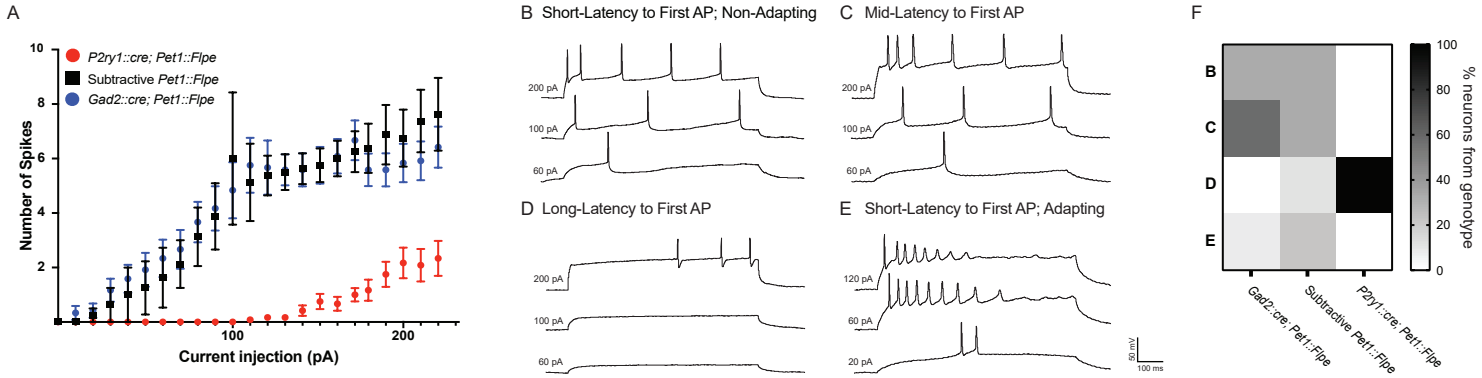
A
P2ry1::cre; Pet1::Flpe
Subtractive Pet1::Flpe
Gad2::cre; Pet1::Flpe
Number of Spikes
Current injection (pA)
B Short-Latency to First AP; Non-Adapting
C Mid-Latency to First AP
D Long-Latency to First AP
E Short-Latency to First AP; Adapting
200 pA
100 pA
60 pA
120 pA
20 pA
50 mV
100 ms
F
% neurons from genotype
Gad2::cre; Pet1::Flpe
Subtractive Pet1::Flpe
P2ry1::cre; Pet1::Flpe

Figure 6- figure supplement 1

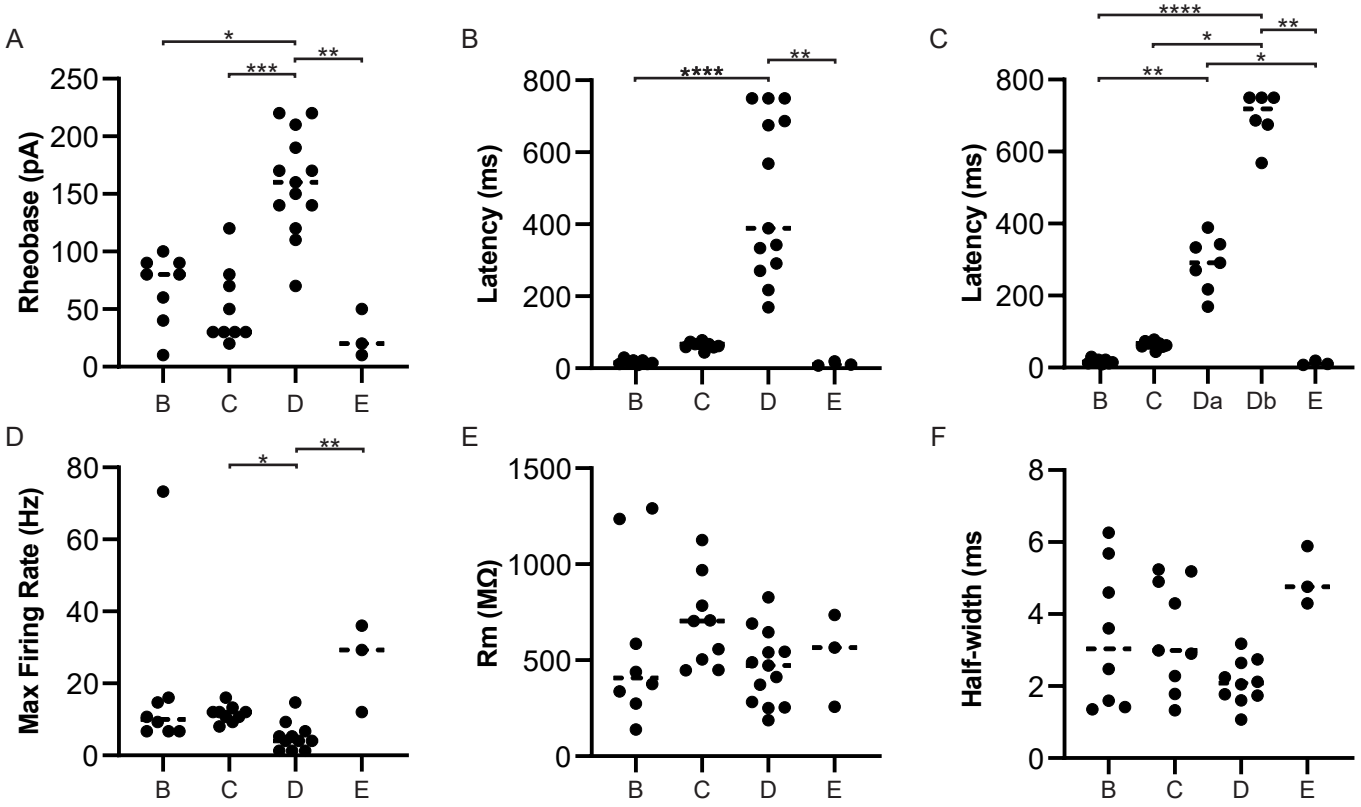

Figure 7

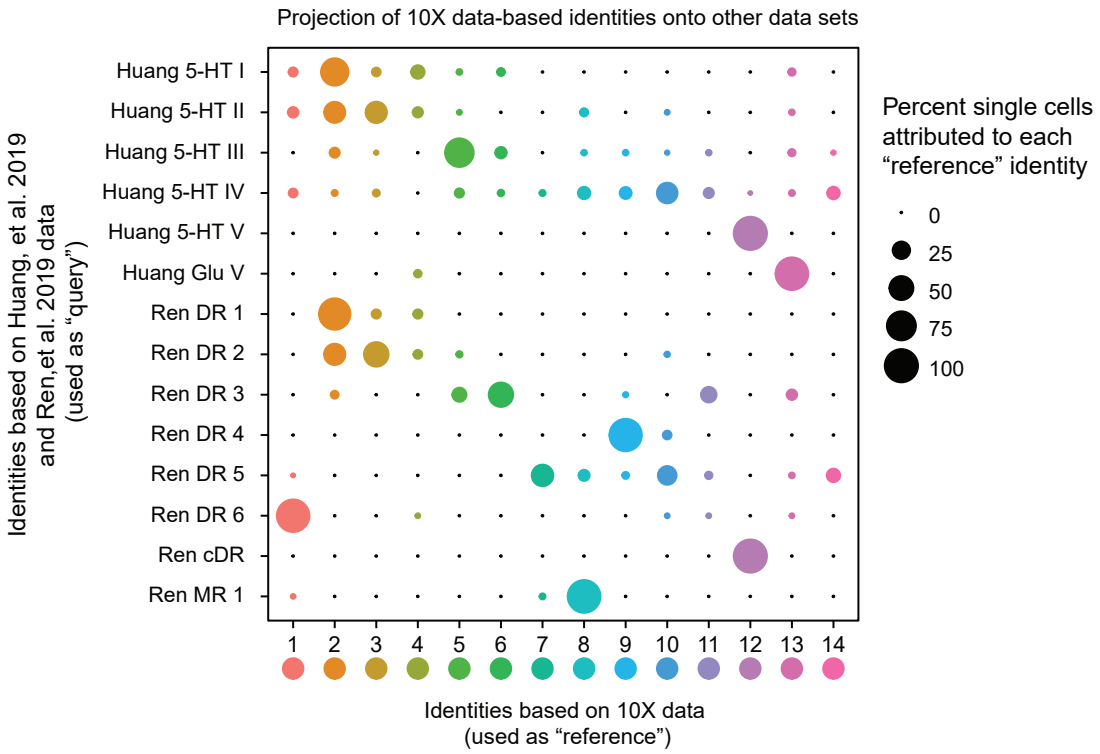
Projection of 10X data-based identities onto other data sets
Identities based on Huang, et al. 2019 and Ren,et al. 2019 data (used as "query")
Huang 5-HT I
Huang 5-HT II
Huang 5-HT III
Huang 5-HT IV
Huang 5-HT V
Huang Glu V
Ren DR 1
Ren DR 2
Ren DR 3
Ren DR 4
Ren DR 5
Ren DR 6
Ren cDR
Ren MR 1
1 2 3 4 5 6 7 8 9 10 11 12 13 14
Identities based on 10X data (used as "reference")
Percent single cells attributed to each "reference" identity
0
25
50
75
100

Figure 8

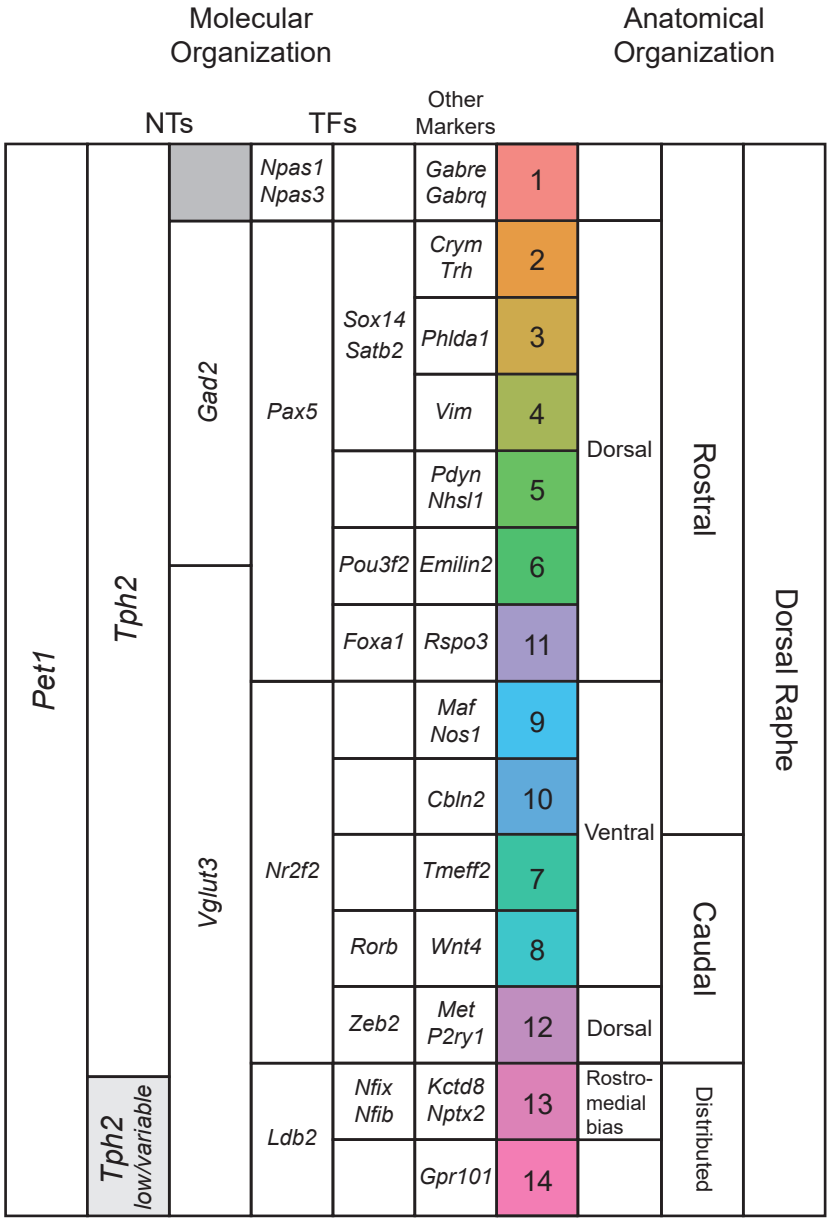
Molecular Organization
Anatomical Organization
NTs
TFs
Other Markers
Pet1
Tph2
Tph2 low/variable
Gad2
Vglut3
Npas1 Npas3
Pax5
Nr2f2
Ldb2
Sox14 Satb2
Pou3f2
Foxa1
Nfix Nfib
Gabre Gabrq
Crym Trh
Phlda1
Vim
Pdyn Nhsl1
Emilin2
Rspo3
Maf Nos1
Cbln2
Tmeff2
Rorb
Wnt4
Zeb2
Met P2ry1
Kctd8 Nptx2
Gpr101
1
2
3
4
5
6
11
9
10
7
8
12
13
14
Dorsal
Ventral
Dorsal
Rostro-medial bias
Rostral
Caudal
Distributed
Dorsal Raphe